Politecnico di Milano

Scuola di Ingegneria Industriale e dell'Informazione
Corso di Laurea Magistrale in Ingegneria Nucleare

Tesi di Laurea Magistrale

Design and development of a dosimetry instrumentation for Quality Assurance in motion adaptive lung radiotherapy

Relatore interno:
Prof. Andrea Pola

Relatore esterno:
Prof. Marco Petasecca, University of Wollongong

Autore:
Diego Cammarano
Matr. 801218

Anno Accademico 2013-2014

Acknowledgements

First things first. Non posso non mettere al primo posto i miei genitori, che 1000 volte ho odiato e 1000^{1000} ho amato. Se sono l'uomo (e non solo a causa della barba che in più occasioni ho sfoggiato) che sono adesso, se qui sotto c'è ancora qualcosa da scrivere e qualcuno da ringraziare, il merito è prima di tutto loro. I loro sacrifici, i loro rimproveri e le loro esortazioni, i momenti di lontananza cercati e non hanno reso la nostra relazione irrinunciabile.
In secondo luogo, ho il piacere di poter ringraziare il prof. Marco Petasecca per la passione e la disponibilità che ha sempre dimostrato, il dott. Anatoly Rosenfeld per avermi accolto nel gruppo di ricerca praticamente senza avere la minima idea di chi fossi, e con loro tutto il gruppo del CMRP. Ringrazio poi il prof. Pola per la disponibilità e la competenza dimostratemi.
Le persone che hanno accompagnato i miei primi passi si meritano ovviamente una posizione privilegiata: i nonni tutti, gli zii, i cugini più grandi (che sono tanti) e anche quelli più piccini (che sono sempre di più). Mi sento, all'interno di questo nutrito gruppo, di fare 3 dediche speciali: il nonno Franco, testa più dura dell'ebano, ma anche curiosità e ambizione tanto sconfinate da farlo salire su un aereo all'alba delle 81 primavere per venirmi a trovare a Parigi; il "Compa", che per tanti anni è stato (e spero continui ad esserlo) una guida preziosa e una insostituibile fonte di ispirazione; la zia Palmina, semplicemente la persona più generosa che abbia mai conosciuto, di gran lunga più buona di tutte le leccornie che sia mai stata in grado di preparare.
Impossibile dimenticare tutti gli insegnanti, o meglio, maestri di vita che mi hanno formato nel corpo e nella mente,: la prof. Magugliani, che è stata la prima a farmi appassionare alla matematica e alle scienze naturali; la prof. Girotti, perchè grazie a lei ho imparato davvero cos'è la disciplina; la prof. Beghetti, che è riuscita a farmi apprezzare davvero il valore delle parole (e, con mio grande piacere, è diventata una splendida amica di famiglia); il prof. Raccagni, perchè non è un caso se quel lontano - ma non troppo... - mercoledì 22 marzo ho scelto di ripartire dall' "Apologia di Socrate" e non dalle leggi di Newton; il prof. Gigante, che, da esperto allenatore e caloroso educatore, ha fatto maturare in me il piacere dello sport e mi ha trasmesso il significato della motivazione in quello che si fa (non mi scorderò mai quel 5 al primo anno diventato 9 al quinto); la prof. Ania, che mi ha fatto conoscere un nuovo modo di guardare alla vita e che è riuscita, in 6 parole, a descrivermi meglio di chiunque altro (me compreso); il prof.

D'Errico, che si è fidato ciecamente di me, più di altri miei veri professori, e mi ha permesso di vivere l'esperienza parigina. Definirvi semplicemente dei professori sarebbe riduttivo, preferisco ricordarvi come dei maestri di vita: grazie infinite perchè mi avete guidato nel diventare una Persona, aiutandomi, stimolandomi e proponendomi sempre il meglio.
Per arrivare a tempi più recenti (quelli dell'università), con tanto affetto ringrazio i bianconigli Gigi (ancora lui...), Teo, Cuca, Costa, Pavel e Richi per aver reso più ignoranti i primi anni al Poli, ed aver vissuto con me tante (dis)avventure tra il celeberrimo S6 (menzione particolare per la Mapi) e la fantascientifica Passat a gas. Ringrazio tutte le fantastiche persone che ho conosciuto nei 2 anni trascorsi a Parigi, tra l'École Centrale ed AirLiquide: il 2B, con dedica speciale ai "bitaliani" Teo (ancora lui...), Profeta, Pier, Botte e Tic; il Club italiano nelle varie generazioni che ho potuto conoscere (una nota di merito alle impareggiabili guide Dami, Mario, Teo e Ricky), il Club Time e il CFC; Tanguy e tutti gli stagiaires che con me hanno condiviso la "calda" estate parigina. Sono salito sull'aereo da ragazzo, e sono sceso due anni dopo da uomo. Non potrei mai smettere di ringraziare i "Nuotto boys" che, tra la biblioteca di architettura, Valva e il leggendario Cesnef, mi hanno accompagnato notte e giorno tra sezioni d'urto, spalle Compton ed equazioni di Maxwell nel sistema di Gauss: il capitano Buccio, Santos, Barca "il ginecologo", Vez, Bencio, il Grana, Giuse, Sasa' e (last but not least) il gran visir Carlo. Probabilmente senza di voi le ore di studio sarebbero state molto più produttive, ma avrei rischiato di cadere nel buco nero della prima fila: grazie per avermi salvato. Eccomi quindi all'avventura australiana: ringrazio i coinquilini di 22 Bode avenue; Kia, Tilman, Túlio, Pedro e la folta comunità brasiliana, che hanno condiviso con me i primi passi a Wollongong; il North Beach Volleyball Collective e i Motherfunckin' Ninjas, per aver riempito i miei pomeriggi tra una schiacciata e un catch (caviglie permettendo); Sebastian, Dany, Vivi, Wence e Laura per aver risvegliato la mia indole latina; Charles, Corentin, Yvonne e Sang, che sono stati dei magnifici compagni di avventura per (quasi) tutta la mia permanenza. Una nota speciale va alla mia semiquasicugina Laura, conosciuta per delle strane coincidenze a 20000 km da casa, e ad Alana, purtroppo conosciuta quando la mia testa era già ai bagagli.
Passo quindi a tutti coloro che, in tempi, modi e luoghi diversi, hanno condiviso con me (e piacevolmente persistono nella loro opera) tanti attimi della mia vita: Dea, una gran testa matta, ma un cuore ancor più grande; Bongio, capace come pochi di trasmettere passione in quello che fa; Ciccio che, non contento di tutte le vaccate fatte insieme, mi ha chiesto di stargli vicino anche in quella che si appresta a fare tra qualche mese; la Roby Palla, valida spalla, confidente e compagna in ogni giorno di scuola dal primo delle elementari fino all'ultimo alla maturità (e anche oltre); Ivan, Bacco, Chri, Gambo, EmmeGi', compagni di mille vacanze estive, oratori feriali, messe di mezzanotte; Emiliano, prima da educatore (e non solo per tutti i km che si è sparato ogni benedetto lunedì) e da amico poi; Paola Squash, la mia non-mia-dottoressa preferita; il gruppo Perù, compagno di viaggio della prima follia oltreoceano; la Mary, la Fede, Tia, Tom e Menca,

perchè quando c'era qualcosa o qualcuno da festeggiare loro c'erano sempre; la Chiara Franca, che non mi ha mai fatto sentire solo tra gli sfigati; i miei compagni (tra POSM e Olmese) di numerose battaglie sui "terreni di gioco" più pericolosi del milanese e tutti i mentori che ci hanno "guidato", con una dedica speciale a Gigi e Davide, che non mi hanno mai fatto sentire solo nella lista degli infortunati; la Com.A. (nomina speciale per il Cele, o più semplicemente il Suca) e tutti i sacerdoti incontrati lungo il mio cammino. Vi chiedo di continuare così, perchè so che avrò ancora bisogno di voi.
Ora è tempo di chiudere questo sterile e poco poetico elenco della spesa (chiedo scusa in anticipo se dovessi aver dimenticato qualcuno), e provare a rimediare con qualche parola di Gesualdo Bufalino che descrive quello che la mia vita è stata finora (e fornisce la chiave di lettura per questi miei ringraziamenti). "L'universo: un acrostico dove cerco di leggere Dio".

Abstract

The stereotactic radiosurgery (SRS) and stereotactic body radiation therapy (SBRT) are radiation therapy modalities currently implemented on all types of linacs and allow conformal treatment even for small volume tumors. Organs motion during treatment is patient specific and can be taken into account in SBRT and SRS by increasing margins in planning target volume (PTV) and using image guidance or organ motion tracking to adapt the radiation beam shape and intensity to the movable target. Organ tracking approach has been recently introduced clinically using the Calypso-guided multi-leaf collimators (MLC) tracking system. In both organ imaging or tracking, a high spatial and temporal resolution dose delivery quality assurance (QA) system is required to provide real-time feedback to clinicians. Presently film only can provide direct dosimetry with adequate spatial resolution but still show large limitations in terms of accuracy and real-time measurement.

Centre for Medical Radiation Physics (CMRP) has developed the Magic Plate 512 (MP512), a high spatial and temporal resolution dosimetry system which, mimicking the moving tumor, measures 2D dose distributions and the effect of movement, simultaneously. MP512 consists of a 2D pixilated (512 pixels) monolithic thin silicon detector with a pixel size of 0.5x0.5 mm^2 and pitch of 2 mm. The sensor is readout by fast front-end electronics which allow for pulse by pulse dosimetry and, in combination with a movable platform, reproduce patient specific tumor motion.

Use of MP512 in combination with the motion platform HexaMotion has been investigated by the use of a patient specific 3D (X, Y and time) lung motion pattern and by the electromagnetic motion tracking system Calypso. Verification of the motion compensation algorithm in controlling the DMLC effectively for accurate beam delivery to the movable target has been achieved, comparing the dose distribution measured by MP512 for static, movable and tracked beam delivery to the phantom.

The radiofrequency electromagnetic field emitted by Calypso induces fluctuations of the baseline current in electronic based dosimetry systems. Such issue has been overcome by the application of an aluminum shielding which encloses the detector maximizing the signal to noise ratio of the instrument. This required a careful dosimetric characterisation of the effect of the aluminium shielding on the detector response.

A timing resolution study has been performed in order to describe the time resolution of the MP512 and its data acquisition system (DAQ). This has allowed to foresee a substantial improvent in the tracking system as, through a Fourier analysis, it is possible to determine a quantitative criterium to make the tracked dose as close as possible to the theoretical one.

Relying on sampling theory, is has been shown that MP512 does not feature a satisfactory resolution for optimal profile reconstruction. For this reason, CMRP has designed DUO, a silicon detector consisting in 2 arrays

which constitute a cross. Its basic characterisation has shown satisfactory results but also new issues linked to the smallness of the active volume of the single pixel.

As this device features the same timing performances of the MP512 and higher resolution than EBT3 films, it has been chosen to be integrated in a Movable Phantom system. The aim of the Movable Phantom is to reproduce a lung motion pattern along one axis in order to verify that the tracking system gets effectively closer to the theoretical profile.

Key words: stereotactic radiotherapy; quality assurance; small field dosimetry; silicon detectors; organs motion management

Sommario

La radiochirurgia stereotassica (SRS) e la radioterapia stereotassica corporea (SBRT) sono tipi di radioterapia attualmente integrati su tutti i tipi di acceleratori lineari e permettono cure appropriate anche per tumori di piccole dimensioni. Il movimento degli organi durante il trattamento è specifico per ogni paziente e se ne può tenere conto nella SRS e nella SBRT aumentando i margini del planning target volume (PTV) e guidandosi usando tecniche di imaging oppure tracciando il moto degli organi per adattare al bersaglio in movimento la forma e l'intensità del fascio di radiazioni . L'approccio del tracciamento degli organi è stato introdotto di recente a livello clinico utilizzando il sistema di multi leaf collimators (MLCs) Calypso. Sia nell'imaging che nel tracciamento degli organi, un sistema di quality assurance (QA) ad alta risoluzione spaziale e temporale della dose ceduta è necessario per fornire feedback in tempo reale ai medici. Al momento, i film possono fornire una dosimetria diretta in maniera adeguata soltanto in termini di risoluzione spaziale, ma mostrano ancora grosse limitazioni in termini di precisione e misure in tempo reale.

Il Centre for Medical Radiation Physics (CMRP) ha sviluppato il Magic Plate 512 (MP512), un sistema dosimetrico ad alta risoluzione spaziale e temporale che, mimando il movimento del tumore, misura distribuzioni 2D di dose e allo stesso tempo l'effetto del movimento. MP512 consiste in un sottile rivelatore al silicio monolitico e pixellato (512 pixels) in 2 dimensioni, con pixel di 0.5x0.5 mm^2 e una spaziatura di 2 mm. Il sensore è letto da una veloce elettronica che permette di effettuare dosimetria impulso per impulso e, in combinazione con una piattaforma mobile, riproduce il movimento del tumore specifico per ogni paziente.

L'uso di MP512 in combinazione con la piattaforma mobile HexaMotion è stato investigato con l'uso di un modello di moto in 3D (X, Y e tempo) di uno specifico paziente e del sistema di tracciamento elettromagnetico Calypso. E' stata realizzata la verifica dell'algoritmo di compensazione del moto nel controllo efficace dei DMLCs per una precisa emissione del fascio, paragonando la distribuzione di dose misurata con MP512 per emissione statica, mobile e tracciata del fascio al fantoccio.

Il campo elettromagnetico di radiofrequenze emesso da Calypso induce delle fluttuazioni della corrente di riferimento nei sistemi di dosimetria elettronici. Tale problema è stato superato applicando una schermatura di alluminio che racchiude il rivelatore massimizzando il rapporto tra segnale e rumore dello strumento. Questo ha richiesto una precisa caratterizzazione dosimetrica dell'effetto della schermature sulla risposta del rivelatore.

Uno studio di risoluzione temporale è stato realizzato per descrivere la risoluzione nel tempo del MP512 e del suo sistema di acquisizione di dati (DAQ). Questo ha permesso di vedere un sostanziale miglioramento nel sistema di tracciamento in quanto, per mezzo di un'analisi di Fourier, è

possibile determinare un criterio quantitativo per rendere la dose tracciata il più possibile vicina a quella teorica.

Basandosi sulla teoria del campionamento, si è mostrato che MP512 non presenta una risoluzione sufficiente per una ricostruzione ottima del profilo del fascio. Perciò, CMRP ha disegnato DUO, un rivelatore a semiconduttori che consiste in due array che formano una croce. Una sua caratterizzazione elementare ha mostrato risultati soddisfacenti e, allo stesso tempo, nuovi problemi legati alla piccolezza del volume attivo dei singoli pixel.

Dal momento che questo strumento presenta le stesse performance temporali del MP512 e una risoluzione spaziale superiore dei film, è stato scelto per essere integrato nel sistema Movable Phantom. Lo scopo del Movable Phantom è di riprodurre un modello di movimento del polmone lungo un singolo asse per verificare che il sistema di tracciamento sia effettivamente più vicino al profilo teorico.

Parole chiave: radioterapia stereotassica; quality assurance; dosimetria dei campi piccoli; rivelatori a semiconduttori; gestione di organi in movimento

Contents

List of Figures

List of Tables

Chapter 1

Radiation therapy and quality assurance

The aim of this chapter is to introduce the main physical and technological points that are involved in small field radiation therapy, as well as all available solution strategies, focusing on lung cancer, in order to define a general context for this thesis.

After a brief introduction about radiotherapy (aim and classifications, paragraph 1.1) and lung cancer (paragraph 1.2), paragraph 1.3 brings SRS and SBRT into focus, pointing out moving targets issues. Paragraph 1.4 deals with lung motion management strategies, concentrating on some possible tracking techniques.

The rest of the chapter is centred on dosimetry for small field applications: difficulties of making quality assurance for small fields (paragraph 1.5), a general introduction about radiation detectors (paragraph 1.6), the ideal solution device for quality assurance of small fields (paragraph 1.7) and a brief overview about the best available devices (paragraph 1.8).

Finally (paragraph 1.9), the general aim of this thesis is presented, as well as its operational objectives.

1.1 Background: radiotherapy

The word *radiotherapy* (also known as radiation therapy or radiation oncology) involves all cancer treatment procedures exploiting ionizing radiation: hence, the aim of this practice is to control or kill malignant cells. This is obtained by damaging the DNA strands of cancerous cells following ionization phenomena.

Thanks to its properties, radiotherapy is often the only treatment a patient needs (e.g. prostate and larynx cancer). Nevertheless, other cancer treatment techniques exist: the main ones are surgery and chemotherapy. All these techniques can be used separately, but sometimes the synergy of two different solutions can lead to better results. In fact, about 30% of all cured patients are treated with radiotherapy, and more than half of all patients receive radiotherapy as part of their cancer management plan [1].

Different types of radiation sources (all with different energies) can be used, either outside (*external beam radiation therapy*, *EBRT* or *teletherapy*) or inside the body (*brachytherapy*). Also, different radiation particles are used: charged particles, neutrons and photons. Depending on the incident radiation as well as on its energy, the interaction with biological tissues (normal tissues and tumour cells) changes. What is crucial is that these interactions are random and not deterministic but depend on several properties of the incident beam and of the target material. This means that it is impossible to irradiate in a single fraction until all tumoral cells are destroyed without cause inevitably damages to normal tissues. Dose-effect curves (Figure 1.1) let us describe this concept: the aim of radiotherapy is the increase of the gap between the "local control of tumour" curve and the "complications" one, then minimizing as much as possible side effects. This concept is expressed by the *therapeutical ratio*: it is the ratio given by the lethal or toxic dose divided by the therapeutic dose. For this reason, one of the biggest remaining issues concerning radiotherapy is achieve a better understanding of the biological response of individual tumours versus normal tissue tolerance.

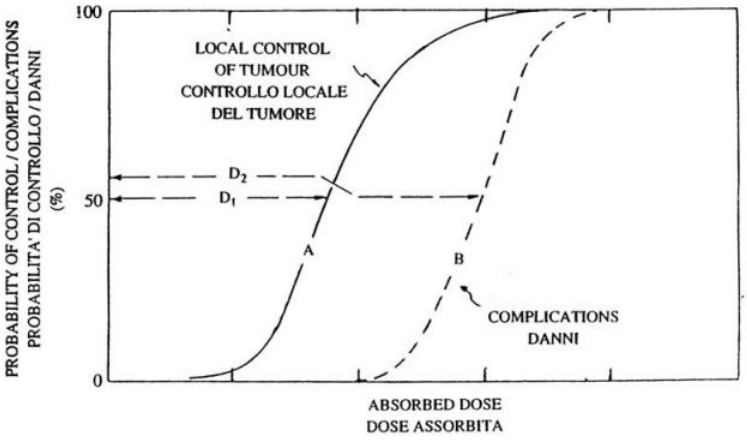

Figure 1.1: Dose-effect curve for tumor (A) and normal (B) tissues. [2]

Considering the fractionation regime adopted, we can differentiate many types of external beam radiotherapy: *stereotactic radiosurgery*, *SRS* (1 fraction); *stereotactic body radiation therapy*, *SBRT* (up to 5 fractions); *volumetric-modulated arc therapy*, *VMAT* (15-16 fractions) and *intensity modulated radiation therapy*, *IMRT* (20 fractions). What differentiates stereotactic from conventional radiotherapy is the precision with which it is delivered.

In particular, this thesis is centred on lung stereotactic radiation therapy lead with photons originating from medical linear accelerators.

1.2 Burden of disease from lung cancer

Lung cancer is the first cause of cancer death for both men and women in North America: in fact, it causes more deaths than breast, prostate and colorectal cancer combined together [3], and is responsible for 1.5 million deaths annually, as of 2012 [4].

It is mostly (almost 90%) due to cigarette smoking (toxic and carcinogenic substances present in cigarettes can deposit in the alveoli): for this reason, it is largely preventable. On the other hand, it is aggressive and metastasizes rapidly and widely in the human body: this makes it hard to diagnose, leading to a reduced cure rate (the five-year survival is about 17%).

Generally speaking, there are three common types of lung cancer:

1. *squamous cell carcinoma* (incidence rate of 25÷30%): it originates at the epithelium of the bronchi and tends to form masses that may cavitate and bleed;

2. *adenocarcinoma* (incidence rate of 40%): it consists of solitary nodules that develop from bronchial glands and alveolar cells;

3. *small cell carcinoma* (incidence rate of 20%): round lymphocyte-sized cells originate from the main bronchi and grow like clusters within the mediastinum, from which a few metastasis can spread rapidly.

In all these cases, because of the nature of lung tissue (it is less dense than water as lungs are filled with air), the tumour shows a higher mass density, making it recognizable via different exams such histology and CT.

Nowadays, there are different possible cure techniques: unfortunately, traditional strategies like surgery and chemotherapy show a low succes rate. For this reason, new therapies are actually undergoing research: the most promising are cancer vaccines, gene therapies and antibodies that target specific growth factors. In this context, stereotactic body radiation therapy represents a different approach to this problem.

1.3 Stereotactic radiosurgery and stereotactic body radiation therapy

Stereotactic (from the Greek words $\sigma\tau\varepsilon\rho\varepsilon o$=solid and $\tau\alpha\sigma\sigma\varepsilon\iota\eta$=orderly arrangement) radiosurgery is a minimally invasive form of surgical intervention which leads to ablation of small targets (up to 4 cm in diameter) inside the body, defined via three-dimensional imaging (CT, PET/CT, MR/CT). In order to achieve such effects, a much higher dose than in conventional fractionated radiation therapy is delivered, which results in a higher biologically effective dose. Therefore, it is necessary to achieve precise target definition and target localization to assure the safety and accuracy of the radiosurgery procedure. This technique was born at the start of the 20th

century and had a stunning development in the years following the Second World War thanks to the contribution of a Swedish neurosurgeon, Lars Leksell, who developed a stereotactic frame exclusively for human patients.

Stereotactic body radiation therapy is a treatment procedure similar to stereotactic radiosurgery, except that it deals with tumours outside of the central nervous system. A stereotactic radiation treatment for the body means that a specially designed coordinate-system is used for the exact localization of the tumours in the body in order to treat it with limited but highly precise fields. SBRT involves the delivery of controlled high doses (8-24 Gy/fraction) of ionizing radiation to a small volume in lung, prostate, liver, or spinal lesions (view [1]) in a single session or a few fractionated treatments (up to 5 sessions) [5].

The aim of SRS and SBRT is to minimize toxicity and provide highly effective treatment of lesions using a strong ablative effect of the tissue in the planning target volume (PTV) region and the use of very small margins ensures that minimal dose is delivered to normal tissues.

The high dose per fraction used in these techniques combined with small radiation fields adopted to treat lesion of less than 4 cm in diameter require particular care in planning and delivery of the dose which have to be verified before each patient dose prescription is delivered. Quality assurance (QA) of such treatments, then, requires specific tools and instrumentation to account for the complex physics behind small field dosimetry. This is even more important considering the fact that the high hyperfractionation of these techniques leaves a lower margin of error (miss a session implies missing the entire treatment).

If this was not enough, dealing with thorax organs gives rise to a new problem: these organs are moving, which means that the small target is, too. This intrafraction organ motion, predominantly caused by patient breathing, is even intensified by external irradiation (as heart rate is increased) and leads to volume and position tumour distortion. As a result, this can compromise the treatment outcome of radiation therapy for tumours in the thorax and abdomen, either by reducing the dose delivered to tumoral cells or by increasing the dose delivered to normal tissues.

In order to cope with this issue, various techniques have been conceived and used through the years, and are presented in the following paragraph.

1.4 Lung motion management

The hysteresis of lung motion is such that the tumour motion path is changed from inhalation to exhalation and back to inhalation by as much as 5 mm in the superior/inferior direction, which means possible serious or even irreparable errors in delivery, such as exposing more healthy tissue to high doses while under-dosing the tumour. In order to increase target doses to very high levels utilizing stereotactic body radiation therapy (SBRT) while keeping the normal tissue dose at a minimum with moving targets, a reliable motion management strategy is necessary. Nowadays, different techniques

are available in clinics for motion management during simulation, planning, and treatment:

1. abdominal compression,

2. breath hold and respiratory synchronized techniques, such as respiratory gating,

3. real-time tumour tracking with multi-leaf collimator (MLC) tracking, couch tracking [6],

where the first two aim to minimize the motion (*step and shoot* techniques) while the last one tries to follow the target in its motion (*moving slit* or *coach moving* techniques).

For all these motion-management techniques to be successful, one needs a reliable form of image-guided radiation therapy (IGRT). The motion can be monitored using IGRT by multiple surrogates: the tumour itself, an artificial marker implanted in or near the tumour, or a surrogate such as the diaphragm.

1.4.1 Abdominal compression

This method uses a pneumatic mechanism for applying abdominal compression to limit the motion of abdominal and thoracic tumours following respiration.

To achieve this, two different approaches exist:

- positioning of a small plate on the patient's abdomen (usually just below the ribs), attached to an arch system that allows to adjust the force applied on the abdomen;

- placement of a tight belt fitted to the patient with an air bladder integral to the belt whose air pressure is controlled with a pump and gauge.

The greatest advantages of these techniques are the easiness of implementation, the needlessness of a 4D planning scan, the compatibility with a conventional C-arm gantry linac and the reproducibility at each treatment of the pressure applied. At the same time, it can be intolerable for patients, specially for spine and lung tumour treatment.

1.4.2 Breath-hold

Breathe-hold methods involve patient holding breath at certain phases of the breathing cycle to reduce and/or control tumour movements. The main goal of these strategies is to exploit anatomical immobilization (and force it in specific positions) to minimize the effects of breathing motion.

Various ways are viable:

- voluntary deep inspiration: reproducible maximum inhalation breath-hold during simulation and treatment. The objective is to immobilize the tumour and to expand healthy lung tissue out of the high-dose region: the beam will be turned on only when the target breath-hold has been attained and turn the beam off if the breath-hold level falls outside a preset tolerance;

- active breathing control: a spirometry system enforces patient breath-holds at preselected volumes of respiration during which dose delivery occurs;

- self-held breath-hold: the patient voluntarily holds his breath at some point in the breathing cycle while the prescribed dose is administered;

- respiratory monitored self-breath-hold: uses an external device to monitor the breathing waveform and to control dose delivery while the patient is required to perform a voluntary breath-hold.

What is more, this technique has an additional benefit for lung and breast patients: dose-limiting organs at risk (OAR) are moved away from the target by utilizing deep to moderate breath holding. This minimizes the dose to vital organs, such as heart.

On the other hand, in all these breath-hold techniques, it is not easy to achieve reproducible breath holds. Moreover, a second key issue is the accuracy of externally placed breath-hold monitors in predicting internal positions of the tumour and nearby organs. Last but not least, these procedures require much more time as the duty cycle depends on how long the target is inside preset tolerances during an entire respiration cycle.

1.4.3 Real-time tumour tracking

This procedure shifts dose in space to track a tumour's changing position: this can be achieved moving the couch, moving the beam, and, above all lately, moving the dynamic multileaf collimators (DMLCs) in the linear accelerator. The main advantage is the reduction of the effect of target motion, without increasing significantly treatment time or linac maintenance costs.

This method includes four steps:

1. 4D-CT: this allows to create separate CT images at discrete phases of the respiratory cycle;

2. selected respiratory phases are reconstructed, and deformable image registration is then performed to map each CT image data set;

3. IMRT treatment planning is simultaneously performed on each CT set reconstructed, and a leaf sequence based on optimized fluence maps is generated;

4. the radiation beam tracks the respiration-induced target motion conformly to the treatment planning.

This way, the duty cycle for treatment is 100% and the dose to OAR is minimized. Although this, the image quality is adversely affected by variations in the breathing pattern, and artefacts are still present even when breathing-training techniques are employed.

Hereafter, three specific techniques are described.

Real time positioning (RPM) optic solution

One possible strategy [7] is based on infrared cameras: they can detect reflective markers applied on the patient's skin. This organ tracking technique, called "real-time positioning monitoring" (RPM) and developed in collaboration with Varian (USA), is combined with the RapidAcr IMRT system.

In order to test this solution, a moving target is utilised so that the difference in dosimetric accuracy could be evaluated with and without the MLCs tracking during the treatment. The treatment plans are calculated using the RapidArc inverse planning method in order to deliver 2 Gy using a Varian 2300ix linac to a lung tumour target of about 12.42 cm^3. The same plan is exported into the Delta4 ScandiDos (Sweden) analysis software: in this way, the Delta4 2D diode array phantom could be used for measurements. Lung tumour movement is simulated by a sinusoidal pattern of a motion platform manufactured by Standard Imaging Inc. (USA). In order to make the MLC follow the exact path specified by the treatment plan, during the experiments the MLC tracking controller was totally disconnected; in any case, both configurations with and without motion of the target volume were tested.

The RPM system is found to have an average error of only 1.1 mm in resolving the location of the target. Dose smearing that occurs due to target motion is significantly reduced when the tracking system is incorporated, and a pass rate of 98% for 3mm-3% gamma analysis and 93% for 2mm-2% is measured when MLCs are activated. In case of motion without the tracking, the pass rates change to 75% for the 3mm-3% and 45% for the 2mm-2% criterion with a 24 mm displacement of the target. The tracking performance was consistent with respect to the magnitude of the target motion, investigated within a displacement range of 5 to 25 mm. However, the limitation of such an approach is mainly related to the difference between the displacement of the exterior surface of the body and the internal tumour motion path in 3D, especially inter-fractions. Unfortunately, simulations of such a scenario by a rigid body as a water equivalent phantom fails to help evaluate the effect of such relative displacements.

Calypso radiofrequency solution

An alternative solution proposed by Keall et al. [8] is represented by Calypso 4D Localisation System (Varian Medical Systems - USA): it is a technology

based on radiofrequency (RF) signals that allows continuous monitoring of the organ motion.

Figure 1.2: Calypso localisation system setup above a patient. [9]

An RF signal is emitted by Calypso (figure 1.2) at a frequency of about 500 kHz: this excites some radiofrequency transponder circuits (called *beacons*, Figure 1.3) which act as dipoles [10] and generate an electromagnetic field. This new field is detected by an array of coils positioned above the patient: the relative distance of each beacon from the array is then recorded. Installing a minimum of three beacons in the organ, it is possible to follow their centre of mass and 3D-reconstruct the exact position of the organ.

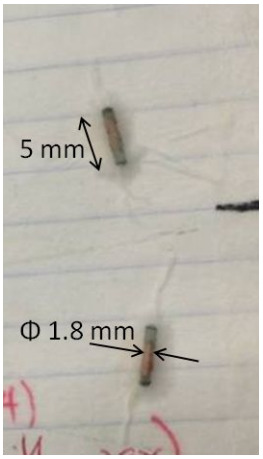

Figure 1.3: Detail of transponder beacons.

Subsequently, the position data is sent to the tracking system that drives the DMLCs. At the same time, the position of the array relatively to the linac head is determined by Infra Red (IR) cameras (Figure 1.4) installed in the treatment room: this gives the relative position of the organ with respect to the DMLC. Finally, a feedback algorithm for calculation of the DMLCs tracking movement based on Calypso data has been developed by Keall et al. at [8]. This technique has been implemented successfully in clinical practice [11].

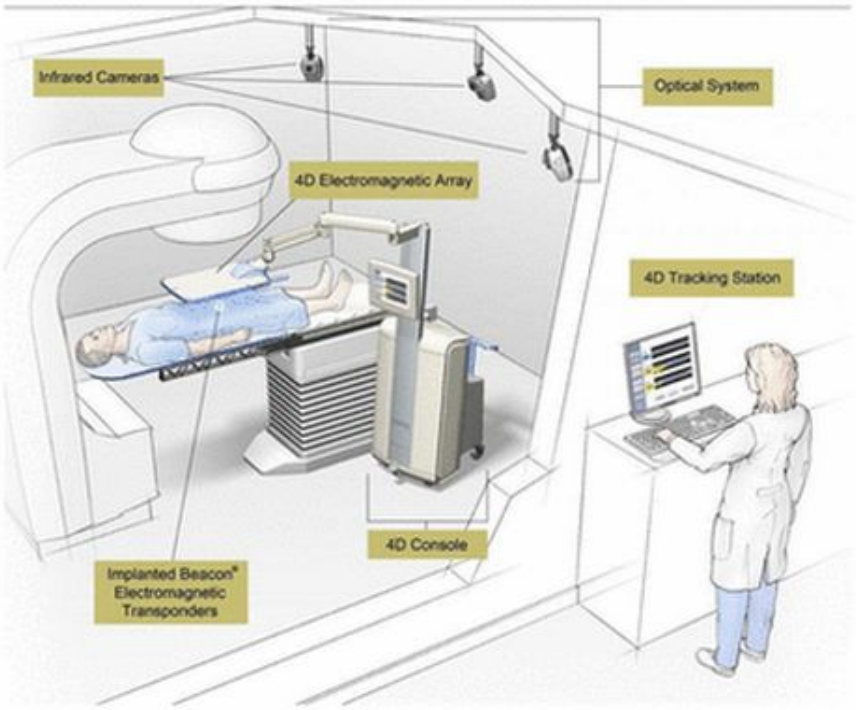

Figure 1.4: Calypso technology with IR cameras localisation system. [12]

Smith et al. [13] have investigated the effectiveness of the implantation of RF transponders by using intensity modulated arc radiotherapy (IMAT) plans generated by Eclipse treatment planning system (TPS) (Varian), which included lung and prostate motion based on patient data. In order to cover the full spectrum of clinical situations, plans with high modulation (optimising PTV and dose to OAR) as well as low modulation (optimising only the dose to PTV) have been tested. For all the plans, 2 Gy were delivered to 95% of the PTV with a 6 MV linac at 600 MU/min. A Seven29 (PTW Germany) 2 ion chamber array was used to take dosimetric measurements: this device consists 729 plane parallel 5x5x5 mm^3 ion chambers arranged in a 27x27 grid with a pitch of 10 mm. A layer of 2 cm of solid water is placed on top of the array for the dose build-up region. The array was irradiated in three modalities:

1. with no motion;

2. with motion;

3. with motion and DMLC tracking.

Plans with motion and no tracking (case 2) resulted in misshaped and shifted dose distributions when compared to the static measurements (case 1). For the lung treatment plans, 34% of points of the plan failed a 3mm-3% gamma criterion for case 2 while only 1.6% of the points failed for case 3. Globally, a 95% improvement was seen in the gamma test results when DMLC motion tracking is used. Smith et al. [13] found the dosimetric measurements with 4D DMLC tracking to be equivalent to gating measurements but with a 2-4 fold increase in treatment delivery efficiency when compared to gating.

In high dose-gradient regions, the distance to agreement (DTA) parameter of 3 mm and the dose difference of 3% adopted in these studies may not be stringent enough for stereotactic radiotherapy modalities (such as SRS and SBRT), where the degree of accuracy is usually higher and, thus, tolerances for dose discrepancies in high dose-gradient regions are smaller than observed in conventional IMRT treatments. Sawant et al. [14] show, with a similar tracking setup, that system geometric accuracy is of the order of 2 mm for lung and 1 mm for prostate motion by using electronic portal imaging devices (EPID). The latter approach has been used to evaluate the temporal and spatial resolution of the tracking system and its latency due to the delay between the movement and the effective reaction of the DMLC, but it does not provide any accurate information of the dose distribution for comparison with the TPS.

VERO mechanical solution

Another possible technique goes by the name of VERO (BrainLab - Germany) [15]: it consists of an integrated imaging and radiotherapy treatment machine for cranial and extra-cranial applications, conceived in particular for moving targets (mainly lung, liver, prostate and spine).

In fact, concerning the imaging side, it features two diagnostic kV X-ray tubes for fluoroscopy and orthogonal X-ray imaging, a volumetric cone-beam CT and a megavoltage EPID for beam verification: all these device provide simultaneous stereo imaging, 6D patient positioning, continuous verification at any gantry angle and at any time during the treatment [16]. The two X-ray tubes can be used separately in order to have a faster image construction process. What is more, there is also an integrated ExacTrac infrared marker-based positioning system that enables real-time patient monitoring.

The irradiation system consists in a gimbaled head with tilt functions for both coplanar and non-coplanar treatment angles. In fact, this allows the patient to remain stationary once positioned: the system moves around the couch delivering the planned dose from more angles with uninterrupted beam delivery.

The main structure (Figure 1.5) is composed by a closed ring: a gimbal holds an accelerator (mated with the inner surface of the ring and designed

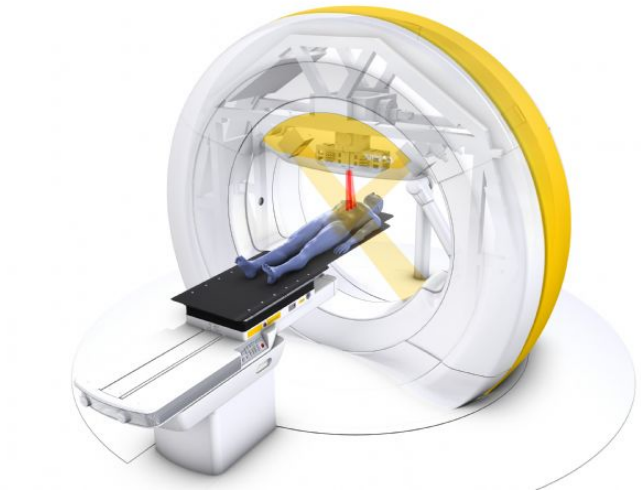

Figure 1.5: VERO imaging and treatment integrated system. [17]

by Mitsubishi Heavy Industries Ltd. - Japan) which can move around the couch placed at the centre of the ring. All the components can move simultaneously: the couch has 6 degrees of freedom (three translations and three rotations, even if its absolute displacement are reduced), the gimbal can rotate for 360° around the couch, the accelerator features a 5 mm leaf MLC system and the ring can pivot ± 60°. This great freedom allows to correct in real time any possible misalignments that are recognised thanks to the image fusion algorithm iPlan. This software also features fully integrated Monte Carlo forward and inverse planning capabilities, which turn out to be useful for extracranial treatments due to the great tissue heterogeneity.

Burghelea et al. [18] benchmarked the VERO system in a planning study against the Novalis SRS system for quality of delivered dose distributions to intracranial lesions in order to assess VERO capacity for SRS. These two systems show many differences such as:

- Novalis has a C-arm gantry while VERO features an O-ring gantry;
- MLC leaf thickness is 3 and 5 mm for Novalis and VERO, respectively;
- Novalis couch can rotate up to 90° while VERO couch has some mechanical limitations to rotations because of the ring gantry.

Globally, 27 patients with one brain lesion treated with the Novalis system were replanned with VERO. Considering tumour volumes larger than 5 cm^3, no significant difference was observed between VERO and Novalis.

On the other hand, for smaller lesions, Novalis showed a better conformity ratio between the volume encompassed by the prescription isodose and the target volume (called *conformity index*, CI), leading to a difference of approximately $\Delta CI = 13.74\%$: in fact, the smaller MLC thickness allows to obtain steeper dose falloff outside the lesion. At the same time, when VERO is used in IMRT mode, the CI difference gets unimportant.

1.5 Small field dosimetry

Ultimately, stereotactic techniques have a few peculiar properties [19]:

1. high dose per fraction (8÷30 Gy/fraction), small number (1÷5) of fractions;
2. total amount of delivered dose of 30÷80 Gy;
3. small radiation fields adopted to treat lesions of less than 4 cm in diameter [20];
4. several angles (7÷9 angles) or full rotation;
5. beam modulation via MLCs or cone collimators;
6. organ movement.

These extreme conditions require particular care in planning and delivery of the dose: precise verification and spatial registration are needed before each patient dose prescription is delivered. Quality assurance (QA) of such treatments requires specific tools and instrumentation to account for the complex physics behind small field dosimetry.

The complexity of this subject is stated by the difficulty in stating a universal definition of the field size. In fact, the usual definition based on the full width at half maximum (FWHM) of the beam profile is not appropriate because of the reduction in output on the central axis and the overlapping penumbrae. This means that the classification of a beam as *small* depends on the properties of the absorbing medium, on how dose varies with field size and also on photon beam energy. In order to reach high dose (order of magnitude of 1÷10 Gy) deliveries in small volumes and in a reasonable time, megavoltage (MV) photon beams are used: referring to these conditions, a field size is defined as *small* if characterized by a square field with dimensions between 0.3 and 4 cm^2.

More specifically, there are three "equilibrium conditions" that determine the scale of a radiation field to be considered as small:

1. the size of viewable parts of the beam focal spot as projected from the detector location through the beam aperture. Occlusion of the focal spot results in lower output than the output for field sizes at which the entire source can be viewed from the detector's field of view as well as overlapping of penumbrae;
2. the secondary electron range in the irradiated medium;
3. the size of the detector needed for accurate measurements.

All these factors place small field dosimetry at the crux of the physics of the stereotactic radiosurgery and radiation therapy paradigm in guaranteeing that doses in the planning system are in agreement with those that are actually delivered.

1.5.1 Partial occlusion of the direct-beam source

The bremsstrahlung photon fluence generated by medical linear accelerators has two different components:

1. *direct-beam radiation* (also referred as *effective X-ray source* or *focal spot*): it originates directly from a radiation source at the level of the target. This distribution is the result of the blurring of the extended-size electron pencil beam hitting the target (so the size and the shape of the spot depend on the shape of the profile of the electron beam), typically has a 3D Gaussian distribution and is described by the the FWHM of the photon fluence profile exiting the target (3÷5 mm);

2. *indirect* (also called *extrafocal*) *radiation*: it originates from photons scattered at structures below the target (primary collimator, flattening filter, transmission ion chambers), and accounts for about 8% of the beam output for a 6 MV beam [19].

Because of the divergency of the photon source (due to an unideal collimation and to the fact that the distance between the bremsstrahlung target and the primary collimators is about 50 cm), the full output read at the position of measurement is not a spot but has finite-size distribution. Nevertheless, the beam source is still entirely visible.

Considering small field applications, the primary collimator setting must be decreased in order to get sufficiently reduced photon spots. This procedure reduces the exposition and visibility of the flattening filter from the position of measurement. This fact makes that extra-focal scatter becomes less important in the determination of the dose. In fact, at very small collimation settings, the direct beam source as seen from the position of measurement is shielded by the collimation device, as shown in Figure 1.6. The larger the focal spot size, the larger the collimator setting at which occlusion of the direct beam source begins. Because of this, the full output read at the position of measurement is smaller than the photon source size and is due to the overlapping of penumbrae profiles. At the same time, as the direct beam source is partially blocked, the number of direct-beam (primary) photons reaching the isocentre is reduced and will be proportionally less for the beam with the largest focal spot size, implying a drop of the output intensity.

The problem of source occlusion becomes important in radiation fields with sizes of the order of the size of the direct beam source (typically not greater than 5 mm), and is sharpened by mobile elements such as jaws and MLCs.

1.5.2 Loss of lateral charged-particle equilibrium

Radiation dose from a photon beam is delivered by secondary electrons that are put in motion by photon interactions with tissue (photoelectric,

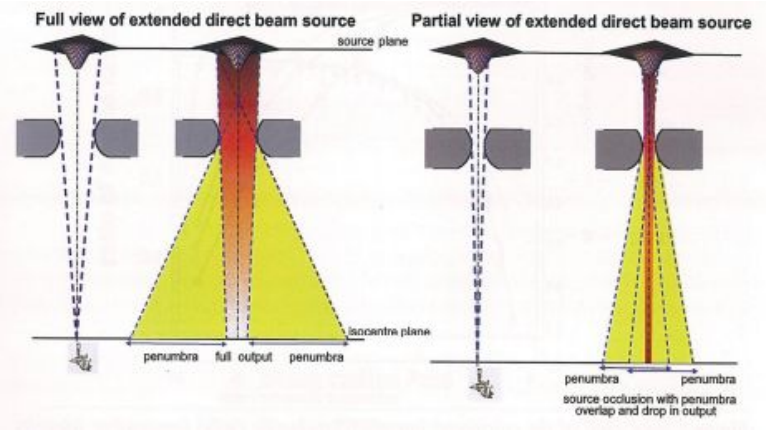

Figure 1.6: Illustration of direct beam source occlusion. [19]

Compton, and pair-production interactions, view Appendix A). These electrons have a finite range in which they deposit energy as they travel through the medium.

For large fields, the lateral equilibrium (view Appendix B) in the central portion of the field is maintained, giving a uniform dose; however, close to the beam edge, there is no equilibrium, and the dose is reduced.

For small fields (especially with high energy beams and tissue heterogeneities) the maximum range of secondary electrons becomes greater than the beam radius, leading to a loss of charged-particle equilibrium (CPE). This means that the lateral range of the electrons is, in general, more significant than the forward range of the electrons for the establishment of CPE for a given field dimension.

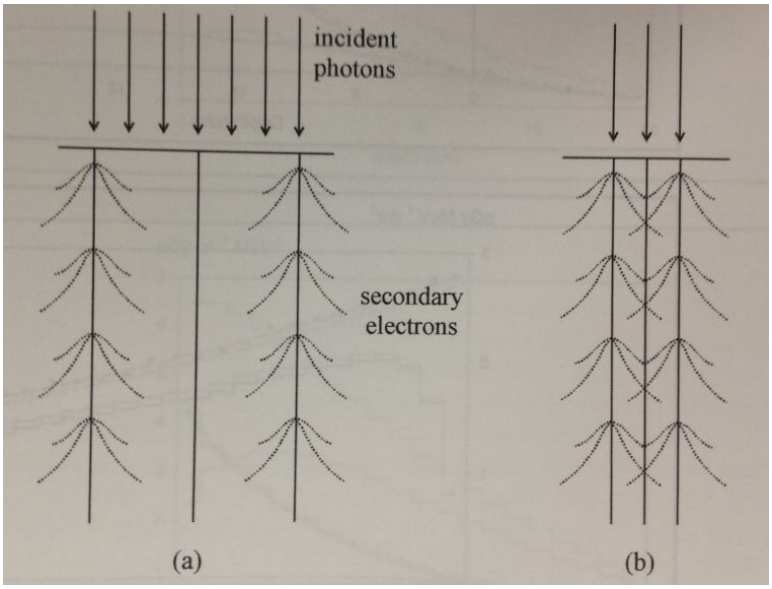

Figure 1.7: Schematic representation of lateral disequilibrium. (a) Electrons displaced laterally from the central axis are replaced by equal numbers from elsewhere; (b) lateral electron range exceeds half the field width leading to lateral electronic disequilibrium. [21]

1.5.3 Equivalent spatial resolution of the detector (based on its volume size and pitch)

Accurate measurements of standard dosimetric quantities with small fields depend on the size of the detector with respect to the field dimensions.

Radiation detectors can be classified according to their size as:

1. standard detectors: volume size of $\sim 10^{-1}$ cm^3
2. mini-detectors: volume size of $\sim 10^{-2}$ cm^3
3. micro-detectors: volume size of $\sim 10^{-3}$ cm^3

The finite size of the device gives an averaged signal over its volume. With normal beam sizes, this is noticeable only in the penumbra region. Nevertheless, with small fields, as the output is given by an overlapping of penumbrae, this results in a reduction in the measured signal in the central part of the beam and a drop in the measured beam output.

1.6 General properties of a radiation detector

A radiation detector is a device designed to detect, track, count, identify particles and eventually determine other properties such as energy, momentum, spin, charge of the detected particles. All available detectors are based on two physical radiation-matter types of interaction: ionization and excitation.

A wide range of different detectors is available nowadays: depending on the specific aim and application, one can give better results than another. Generally speaking, every detector for medical applications should be provided with the following properties.

1.6.1 Stability

Any measurement has an uncertainty which is partly inherent in the measurement device and partly linked to the method of measurement and the variation of the parameter being measured. An indication of the global stability of the whole measurement system is given by the standard deviation of a certain amount of different measurements in which all controllable irradiation parameters remain unchanged.

Instabilities can be related to variations in detector response caused by its irradiation history. A proper calibration can be used to correct short or long term degradation of the detector response.

1.6.2 Dose linearity

The ideal response given by a dosimeter should be linearly proportional to dose over the wider range possible. Its limits are determined by the background noise and by a possible over-response of the detector leading to saturation at high doses.

1.6.3 Energy response

Detectors for small field dosimetry applications should have a uniform response all through the useful energy range up to 25 MV photons or electrons beams.

1.6.4 Spatial resolution

The spatial resolution consists in the ability in determination of the variation of dose as a function of its spatial distribution. Therefore, its requirements depend on the gradients of the quantities to be measured.

Usually, it is a matter of trading-off between signal-to-noise ratio and dosimeter size.

1.6.5 Background signal

The zero dose reading of a detector inevitably affects the low dose limit as well as the signal-to-noise ratio. Any leakage leading to increasing background reading should be at least three orders of magnitude smaller than the detector response.

1.7 Ideal QA detector for SBRT applications

The goal of quality assurance is the design of a radiation detector that is used on the patient just before or during the treatment to verify the dose given to the patient. Therefore, when trying to characterize a small photon beam for stereotactic radiation therapy applications, the measurement of penumbræ is crucial to calculate the delivery parameters. Other important aspects are percentage depth dose (PDD), tissue phantom ratio (TPR) and field size factors.

In particular, if we concentrate on SRS and SBRT, in order to characterise their dosimetrically relevant peculiarities, the ideal detector should have the properties described hereinafter.

1.7.1 Spatial resolution

This feature depends on the sensitive volume as well as on the pitch between two pixels of the detector.

1.7.2 Isotropy and angular independence

In order to obtain the wanted dose distributions, the treatment planning (TP) might decree the use of the linac photon beam from different positions, one after each other. Because of this, an ideal detector should give the same response isotropically, regardless the relative direction of the beam. A possible alternative is the capacity of characterising the angular dependence and therefore correct the wrong acquired data.

1.7.3 Large dynamic range

The detector should be able to provide a high sensitivity for small as well as for large range doses.

1.7.4 Angular independence

In order to obtain the wanted dose distributions, the treatment planning (TP) might decree the use of the linac photon beam from different positions, one after each other. Because of this, an ideal detector should give the same response isotropically, regardless the relative direction of the beam. A possible alternative is the capacity of characterising the angular dependence and therefore correct the wrong acquired data.

1.7.5 Energy independence and tissue equivalence

The photons energy distribution is a continuous spectrum going from 10÷20 KeV [22] to E_{max} (Figure 1.8) which is the energy of the electron bunches before colliding on the bremsstrahlung target. Therefore, it is necessary that the response of the detector does not change (or changes in a known way) with the energy of the photons interacting with it, in order not to under- or over-estimate some contributions.

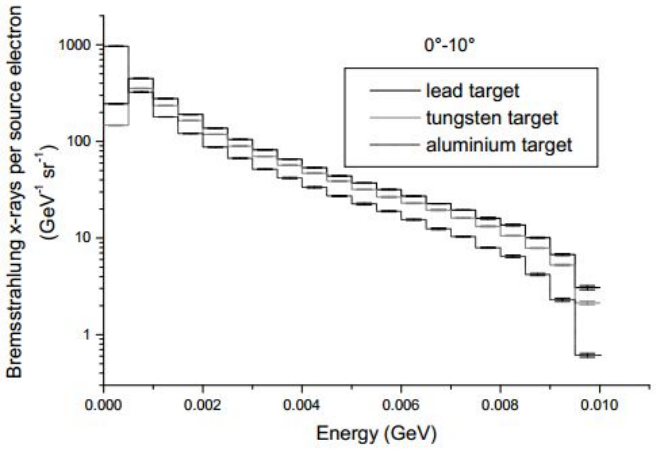

Figure 1.8: Energy spectra (calculated with FLUKA) for bremsstrahlung X-rays produced by 10 MeV electrons with different materials targets. [2]

1.7.6 Dose rate independence

Medical linear accelerators are pulsed devices: the deliverable dose rate is modulated by varying the number of pulses. Therefore, in order to reduce the delivered dose, it is sufficient to reduce the number of pulses per second. Because of this, it is not possible to verify the dose rate independence just varying the delivered dose: the instantaneous dose rate corresponding to one

pulse is not influenced by the delay between two pulses and is approximately 100 Gy/s for a 10x10 field size (FS) at 1.5 cm depth in water.

The correct way to study the dose rate dependence of a detector consists in deliver a fixed amount of dose (usually 600 MU/min, which correspond to $2.78\text{x}10^{-4}$ Gy/pulse) and take advantage of the geometric effect. In fact, distancing the detector, the $\frac{1}{r^2}$ decrease factor of the intensity of the beam makes the dose vary regardless of the pulse frequency.

1.7.7 Fast (real-time) response

In dynamic radiotherapy modalities, the ability to describe beam profiles in real time can allow to get additional information about the time evolution of dose deposition. This can be really important in order to identify real-time contingent errors and react in real time in order to correct them. In fact, when this is not possible, it is necessary to wait and undertake a long processing in order to realise there has been an error: obviously there is no possibility to correct errors as the treatment is over.

1.7.8 Radiation hardness

Depending on the structure of the detector as well as on the type of radiation, the material can be irreversibly damaged. Some detectors can recover their original properties after a certain latency time (depending on the specific detector), while pre-irradiation helps maintaining the detector response stable.

This factor can be relevant when the global dose is high.

1.7.9 Robustness

All along its use, a detector needs to be safely moved and handled. In order to avoid (either resolvable or definitive) damages and breakages, it must be as little fragile as possible.

1.7.10 Reproducibility

The possibility of obtaining the same response under similar conditions from the same detector makes the running of different experiment more uniform. This parameter is usually expressed in one or two standard deviations.

An alternative is still possible: in fact, as quality assurance detectors for stereotactic therapy treat relative (and not absolute) dosimetry, systematicity in errors can be overtaken via correcting factors.

1.7.11 Environmental factors independence

External parameters like pressure, humidity and, above all, temperature should not influence (or do it as little as possible) measurement results.

1.8 Available QA detectors

Nowadays, different dosimeters are commercially available. Ideally, the perfect detector would be fit for measuring large as well as small fields with the same performances.

A wide range of detectors has been used for small field dosimetry applications: the choice depends on the needs of the particular case (real-time readout needed, maximum spatial resolution needed, 1D or 2D measurement) as well as other practical factors, such as the simplicity and the cost of the detector. Since no device guarantees the ideal combination of characteristics, measurements should be cross-referenced between at least two different detector types when possible.

1.8.1 Ionization chambers

Ionization chambers are the reference type of dosimeter in radiation therapy. They provide reproducible measurements, generally have high sensitivity and are nearly energy independent and radiation-hard (dose, and dose-rate independent). However, typical ionization chambers are not suitable for small-field dosimetry because of their large active volume. Microionization chambers with active volumes ranging from 2 to 7 mm^3 have been reported as used for small field measurements. Using small volumes means that the signal leakage might be significant, particularly in low dose regions, and that the device is, from a mechanical point of view, fragile.

A possible example is represented by MatriXX (IBA - Germany, Figure 1.9) 2D detector array.

Figure 1.9: MatriXX detector.

Recently, liquid filled ionisation chambers with a sensitive volume of 2.3x2.3x0.5 mm^3 and pitch of approximately 2.5 mm (Octavius 1000 SRS, PTW – Germany, Figure 1.10) have been introduced and appear to be as a valid solution for high spatial resolution ionising chamber arrays [23].

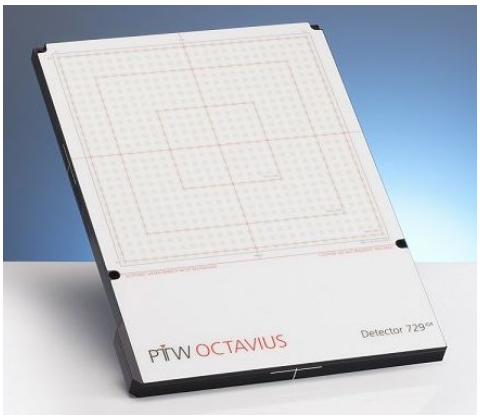

Figure 1.10: Octavius 729 detector. [24]

1.8.2 Solid-state detectors

Diverse devices and technologies go by the name of solid-state detectors:

- *Semiconductor silicon diode detectors* are an attractive option because of their high sensitivity and relatively small active volumes (diameters of 0.6-1.13 mm, 0.01-0.06 mm thickness) as well as their enhanced response per unit volume due to both their density (1000 times that of air) and their lower charged particles couple creation energy (also called W) values. At the same time, they exhibit some limiting characteristics: variations in measurement with accumulated dose, non water-equivalent composition for low energy photons (the high atomic number of silicon leads to a higher response to low energy photons), angular dependence. Depending on the different substrate, we can mention n-type diodes arrays MapCHECK, MapCHECK2 (Figure 1.11) and ArcCHECK (Figure 1.12) (Sun Nuclear - USA) and p-type diodes array Delta4 (Scandidos - Sweden, (Figure 1.13).

Figure 1.11: MapCHECK2 detector. [25]

- Although their high cost, *diamond detectors* are an interesting alternative to silicon diodes because of their water equivalence for photon

Figure 1.12: ArcCHECK detector. [26]

Figure 1.13: Delta4 detector. [27]

beams, their almost constant stopping power and mass energy absorption ratios with respect to water (leading to an excellent energy independence), their radiation hardness, low noise (due to the high band gap energy) and high spatial resolution. On the other hand, their significant dose rate dependence can be a really constraining handicap. This issue is stressed by a negative under-response at low energies and, at the moment, does not make diamond detectors price worth compared to its performances.

- *Metal Oxide Semiconductor Field-Effect Transistors* (*MOSFETs*) are used for in-vivo dosimetry thanks to their simplicity of readout and their high spatial resolution. Unfortunately, they show excessive energy dependence and anisotropy (compared to ionization chambers).

1.8.3 Films

Two families of films are used for small field dosimetry, especially for quality assurance. They are renown thanks to their superior spatial resolution as well as the 2D capability they intrinsically feature. In fact, they might be considered as the golden standard device for off-line QA.

- *Radiographic films* inherently have excellent spatial resolution and provide good profile measurements in small fields. The biggest disadvantage of radiographic film is that a long processing is required to develop the film. Other handicaps are their limited dose range united with their energy and orientation dependence.

- *Radiochromic films* are an attractive option for small-field dosimetry because they have high spatial resolution, are nearly water-equivalent, and do not require any processing but still require a latency time before scanning. Exposed films differentially absorb colour: the highest light absorption is in the red wavelength, the best contrast is achieved if this colour channel is extracted from the scanned image. In order to scan these films, a conventional red-green-blue (RGB) flat-bed document scanner or a HeNe laser scanner can be used.

  Considering EBT films (Figure 1.14), which have been used as a benchmark in this thesis work, they can provide a useful dose range between 0.01 Gy and 10 Gy, a nearly water-equivalent effective atomic number (film Z_{eff}=6.84 compared to water Z_{eff}=7.3) [28] and sub-mm spatial resolution. On the other hand, they might show some criticalities because of darkening, UV sensitivity, temperature, polarisation and orientation dependence.

In fact, it exists also a verification phantom called QUASAR (Modus Medical devices - Canada, Figure 1.15) which integrates a film cassette and several inserts for holding and positioning an ion chamber.

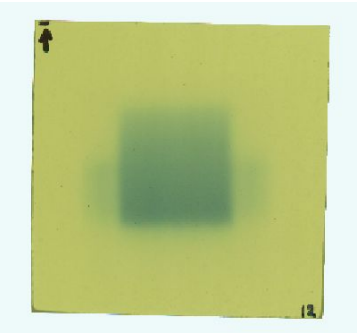

Figure 1.14: EBT3 film detector after irradiation.

Figure 1.15: Quasar verification phantom. [29]

1.8.4 Thermoluminescent dosimeters

Thermoluminescent dosimeters (*TLDs*) consist in non conducting crystals (at room temperature all the electrons are in the valence band), usually lithium fluoride doped with titanium and magnesium LiF(Mg), LiF(Ti): when these materials are irradiated, some electrons gain enough energy to get into the conductivity band. The presence of imperfections in the crystals can trap these moving electrons at an energy state that is in the energy gap: the number of electrons effectively trapped is a function of the incident radiation (typically less than 1% of the electrons in the conduction band). Rising the temperature, trapped electrons have enough energy to be raised to the conduction band and release energy (light) when they recombine with a positive hole in the valence band: this happens in special transition centres called colour centres.

This technique is well established for in-vivo use and for dose point measurements thanks to the wide dynamic range and the water equivalence of LiF crystals, but they have a large uncertainty (about 3%) and require a long read-out procedure. What is more, once the detector has been heated up and annealed, the reading gets lost and is not reproducible.

1.8.5 Optically stimulated luminescence dosimeters

Optically stimulated luminescence dosimeters (*OSLDs*), also known as radioluminescent detectors, consist of silver activate metaphosphate glass detectors: the irradiation produces stable colour centres that emit orange light when read by a N_2 laser system. If compared to TLDs, they have a higher energy response, but show excellent reproducibility, dose linearity, negligible fading, good spatial resolution, can be reused by annealing at 400°C and allow unlimited repeat readings.

1.8.6 Plastic scintillating detectors

Plastic scintillating detectors (*PSDs*) are made of a 5 mm long, 1 mm diameter polystyrene core that is pasted on a fibre optic cable. The latter is connected to a photomultiplier or a photodiode in order to get a readout. This detection system shows an excellent water equivalency over a wide energy range (0.2-25 MeV), high spatial resolution, highly sensitive detector material (which enables small sensitive volume construction), photon-beam quality independence, dose rate independence, dose linearity, and instantaneous reading. Their major drawback is the generation of a Cerenkov signal in the optical fiber that transports the scintillation photon to the photodetector. This blue emission is referenced with a second fibre cable and subtracted in order to reduce the noise [30].

A clinical prototype of a small sensitive volume (1.6 mm^3) scintillator was developed by Lacroix et al. [31]. The plastic scintillator is a BCF-12 (Saint-Gobain - France), it is 2 mm long and has a diameter of 1 mm, and is glued to a 1 mm diameter BCF-98 optic fibres 1.7 m in length which carry

the photons emitted from the scintillator to a charge-coupled device (CCD) readout system. Dosimetric performances agree in an excellent way with ionizing chambers and films [32], but there are still some limitations in the number of channels (due to the routing of the fibers), in the degradation of the light yield due to radiation damage effects and in the acquisition time (which can get up to several seconds for an accurate estimation of the dose distribution).

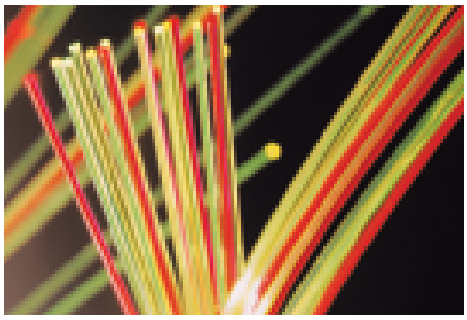

Figure 1.16: Scintillating fiber BCF-12. [33]

1.8.7 Gel dosimeters

This family of detectors is based on the stable chemical modifications (such as chengements in the oxidation number) due to radiation-matter interactions. In fact, it is possible to get a quantitative relationship between the dose and the entity of the chemical modification: thanks to a quantitative chemical analysis, it is possible to calculate the quantity new chemical product and obtain the value of the absorbed dose.

These devices are naturally three dimensional and tissue equivalent. At the same time, phantoms can be shaped in any shape and can incorporate other materials. On the other hand, technical difficulties in reproducibility of the gel make these detectors really expensive.

1.8.8 Conclusions about detectors

The specifications for a dosimeter to be used specifically in SBRT can be summarized as:

1. total sensitive area should include both the beam and the margins related to the target motion in a detector array plane (nominally 2 cm in the superior/inferior plane, 1.5 cm in the medial/lateral plane);

2. spatial resolution in the order of mm or less;

3. the active sensitive volume must be small to avoid any averaging effect in the steep dose gradients;

4. sampling temporal resolution in the order of hundreds of milliseconds. Although this may not be essential to verify the integral dose for daily

QA, this is desirable to resolve the 2D dose distribution variation in time if a failure occurs and the physicist needs to verify when the failure happens and in correspondence to which position.

For all these reasons, the use of multiple parallel 2D detectors remains one of the best ways to study the dose distribution for QA applications.

Among all the available devices listed in the previous paragraph and summed up at Table 1.1, only a few shows a 2D mapping capability. Radiographic and radiochromic films are inherently 2D systems: they provide the best spatial resolution achievable. On the other hand, they require a long and demanding readout process: this fact implies that the readout is not available in real time, and thus can not be used in dynamic radiotherapy modalities. The results they provide represent the integral dose, with lack of time-dose resolving capability. Semiconductor silicon diode detectors are widely used in QA as single point detectors or in 2D arrays and can be translated to monolithic 2D diodes arrays with submillimeter spatial resolution. These are fabricated on a thin substrate which minimizes the perturbation of the beam. In particular, high-resolution detector arrays (1D) and matrix (2D) have many advantages over single point detectors for dosimetry in small field modalities: online capability, dose integration of dynamic beams, dose-time analysis and use of an individual channel to characterise the scatter parameters.

The 1D high spatial resolution monolithic diode array (DMG) was developed earlier by the Centre for Medical Radiation Physics (CMRP) research team and was shown to be suitable for small beams QA in EBRT [34].

Subsequently, CMRP developed two other detectors that can meet the system requirements for QA in SBRT and SRS dosimetry: the 2D monolithic diode array Magic Plate-512 (MP512) and the 2D pixellated array DUO.

1.9 Aim of the project and operational objectives

Within this context, the aim of this project is the validation of use of 2D silicon detectors MP512 and DUO for adaptive motion radiation therapy modalities in SBRT and SRS and the development of a moving target phantom (called *Movable Phantom*) with MP512 or DUO embedded for dose distribution measurements in lung for SRS and SBRT applications in combination with MLC tracking techniques.

This system should integrate the MP512 and DUO advantages (high resolution and real-time readout) in a timber lung phantom capable of reproducing lung movements along a single axis. Its specific role is to perform the QA for SRS and SBRT treatments: this consists in the verification of the agreement of the linac as well as the motion management and tracking systems with the treatment planning.

Table 1.1: Summary on detectors characteristics.

	pixels	dimensions	absolute dosimeter	spatial resolution	timing resolution	angular independent	development
Ion chambers	1020	3D	✓	7.5 mm	real time	✓	commercialised
Semiconductors	1527	3D	×	submil	real time	×	commercialised
Diamonds	36	3D	×	submil	real time	×	research
TLDs	289	2D	×	11 mm	post-process	×	research
Films		2D	✓	submil	post-process	✓	commercialised
Plastic scintillators	100	3D	×	1.5 mm	real time	×	research
Gel dosimeters		3D	×	submil	post-process	✓	commercialised

The specific aims of this work can be divided in four sections:

- static characterisation of MP512 performances;
- clinical dynamic characterisation of MP512 in DMLC tracking beam scenarios;
- static characterisation of DUO performances;
- design and realisation of the Movable Phantom, detector integration, movement management and characterisation of the embedded system in DMLC tracking beam scenarios.

Chapter 2

Main materials: Magic Plate 512, DUO and Movable Phantom

The aim of this second chapter is to describe in detail the main radiation detectors that will be used in this thesis.

The first section is centred on silicon detectors MP512 (paragraph 2.1) and DUO (paragraph 2.2): both of them have been conceived and designed at CMRP. For each of them, there is a detailed description of the structure with some details about the technique of fabrication.

Subsequently, the second part of the chapter presents all the auxiliary instrumentation which is necessary for these detectors to work: the data acquisition system (paragraph 2.3), the detector packaging (paragraph 2.4) and the data acquisition software Romulus (paragraph 2.5).

Finally, the last section of this chapter includes a description of lung anatomy (paragraph 2.6) and of breath mechanics (paragraph 2.7) which introduce the specifications required for the Movable Phantom design (paragraph 2.8). In fact, this consists in two main parts: the structure of the phantom and the management of its motion.

2.1 Magic Plate 512

The first detector which has been used during this study is the Magic Plate 512 (MP512). An article published by CMRP group on Medical Physics [35] has been dedicated to its characterisation for dosimetry in small field radiation therapy.

It is a monolithic diode dosimeter containing 512 ion diodes arranged in a squared array, as shown in Figure 2.1.

Figure 2.2 displays a section on the detector in order to exhibit its structure. The bulk is composed by a 470 μm thick p type silicon substrate with resistivity ρ =10 Ω·cm. Underneath the bulk, a grounded 0.8 μm p+ type layer has been obtained by implanting donor ions of phosphorus (P) using an accelerator. On the other side, the 512 diodes are present: they are of

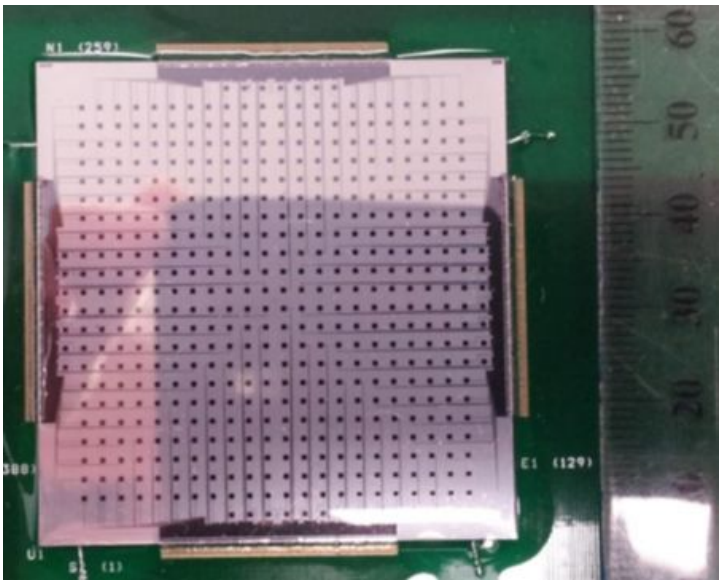

Figure 2.1: Magic Plate 512 mounted and wire bonded to the thin PCB.

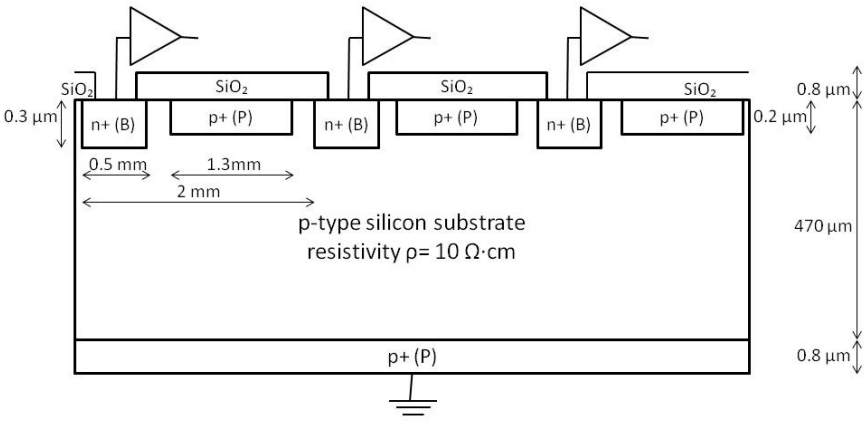

Figure 2.2: A section of the Magic Plate 512 (not in scale).

size 0.5x0.5 mm^2, have been obtained by implanting acceptor ions of boron (B) and are read out individually. The pitch between two diodes is 2 mm, making the overall dimension of the detector of 52x52 mm^2.

Figure 2.3 shows the schematics of MP512, wire bonded on a thin (0.5 mm thickness) printed circuit board (PCB) and covered by a layer of protective epoxy resin to preserve the silicon detector from moisture and chemical contamination as well as to protect the bonding wires. The PCB provides the fan out for connection of the sensor to the readout electronics. The MP512 silicon detector operates in passive mode, where no bias voltage is applied to the diodes.

MP512 was placed between two 5 mm-thick poly(methyl methacrylate) (PMMA) slabs. This procedure has two main purposes:

- protection from mechanical damages;
- shielding from ambient light;

depending on the experiment, these PMMA layers might be removed as they might alter the measurements.

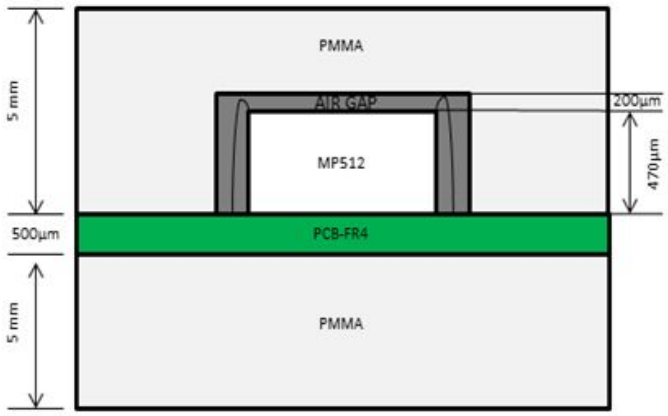

Figure 2.3: Schematics of the Magic Plate 512 packaging between two PMMA slabs (not in scale).

Moreover, in order to stabilise its response before its characterisation, MP512 has been pre-irradiated using a ^{60}Co gamma source up to 4 Mrad. Its radiation hardness performance has been extensively characterised by irradiation with photons from a Co-60 gamma source and on mixed photo-neutrons radiation field from 18 MV linac demonstrating very good radiation stability with variation of the response approximately 1%/10 kGy(H2O) of Co-60 and 0.9%/10 kGy(H2O) on 18 MV linac.

2.2 DUO

DUO (Figure 2.4) is a silicon microstrip detector: it consists in four narrow strip arrays disposed in order to form a cross. Every array has 125 pixels

of 20x800 μm^2, while the center features 5 squared pixels of 50x50 μm as shown in Figure 2.5, giving a total of 505 pixels.

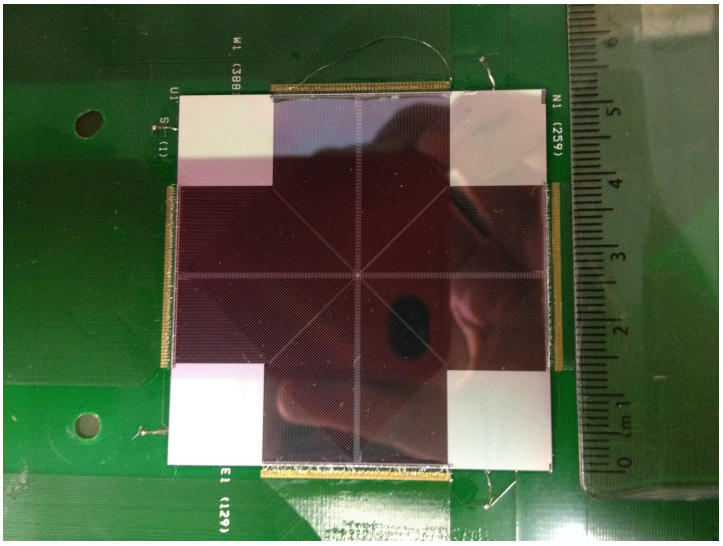

Figure 2.4: DUO mounted and wire bonded to the thin PCB.

As shown in picture Figure 2.6, the concept of its structure is very similar to the one of MP512: the main difference is the fact that the diode is 20 μm wide, allowing to have a pitch of 200 μm which is much more interesting in terms of spatial resolution.

DUO schematics exactly coincide with the one described above. Moreover, as well as MP512, DUO has been pre-irradiated before its characterisation using a ^{60}Co gamma source up to 14 Mrad in order to make its response stable and avoid changes due to radiation damage effects.

2.3 Data acquisition system

The data acquisition (DAQ) system is an important component of any multichannel detector device: its role consists in the conversion of electric signals originating from the detector into digital values for downstream processing.

In this study, the two detectors described above share the same DAQ, schematised at Figure 2.7 and shown at Figure 2.8 and Figure 2.10.

The prototype was custom-designed by CMRP and based on a multichannel electrometer chip: it is an AFE0064 chip (Texas Instruments). This device consists in a 64 channels device: each of these channels integrates the current generated in a pixel of the detector and accumulates the corresponding charge during a pre-settable time frame configurable for each channel [36].

The chip is set electronically through a serial protocol interface (SPI) on the lowest gain available to span the full scale up to 9.6 pC with a resolution of 16 bits and a non-linearity less than 0.1%. Each current integrator is equipped with a double sampler for subtraction of the baseline: this feature

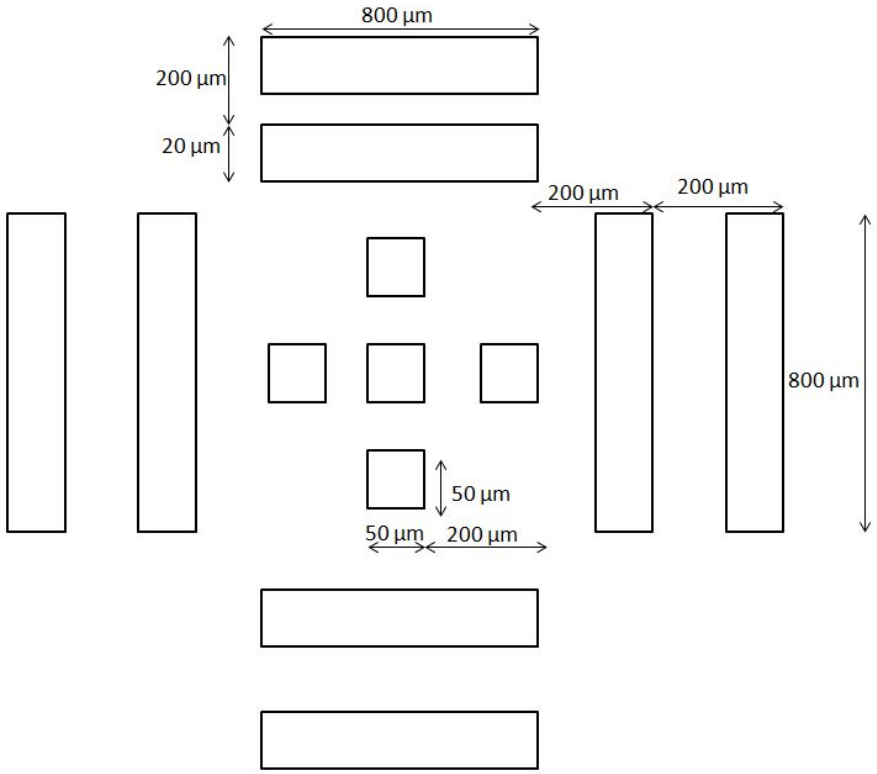

Figure 2.5: Representation of the central pixels of DUO (not in scale).

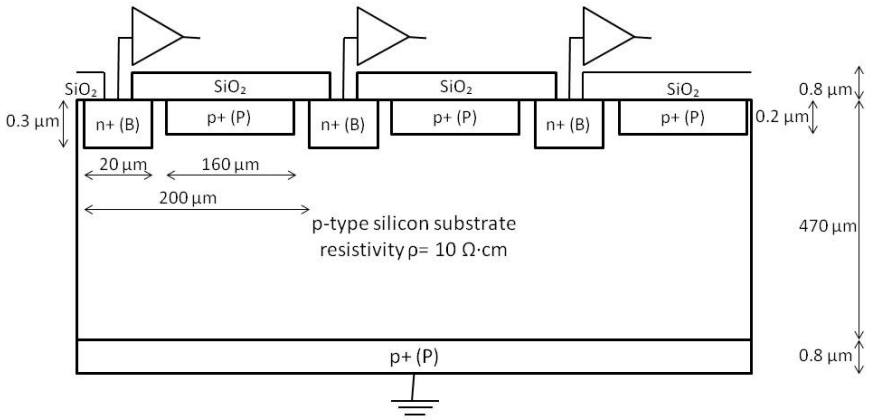

Figure 2.6: A section of the DUO (not in scale).

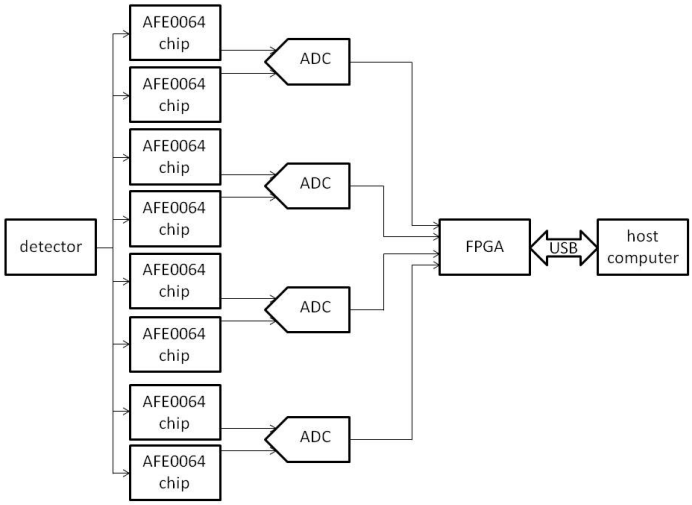

Figure 2.7: Block diagram of the DAQ system.

is important especially when a high signal-to noise ratio is required, as in the case of medical instrumentation.

A voltage (which still corresponds to the charge generated in the pixel) is then obtained and compared to a reference potential tension: this value is sent to an analogic buffer. Each of the 64 buffers is linked to a multiplexer which forwards all the input signals into a single line, making it available outside the chip.

In fact, as MP512 features 512 pixels, the DAQ system uses eight chips, for a total of 512 channels: they are readout in parallel by four analogue-to-digital converters (ADC).

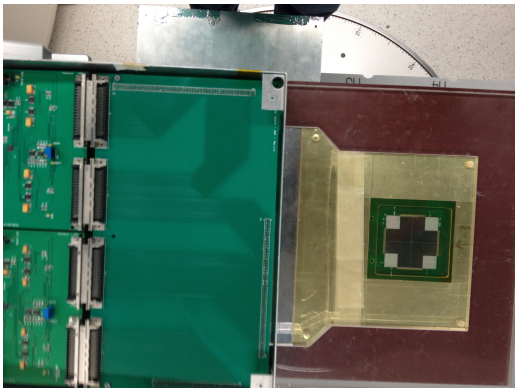

Figure 2.8: Connection between DUO and the DAQ system.

The AFE0064 chip and the ADCs are managed by a Field Programmable Gate Array (FPGA) which provides the clocks and the synchronisation circuitry to manage the trigger signal provided by the linac: this allows to synchronise the acquisition when the beam is on. For this reason, a physical connection between the FPGA and the linac is necessary: this is realised by the means of a coaxial cable.

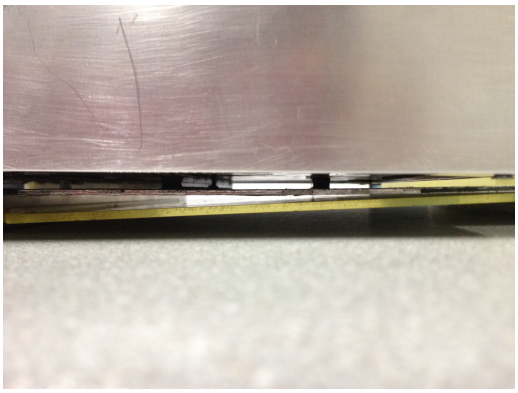

Figure 2.9: Detail of the plug of the PCB board in the DAQ system.

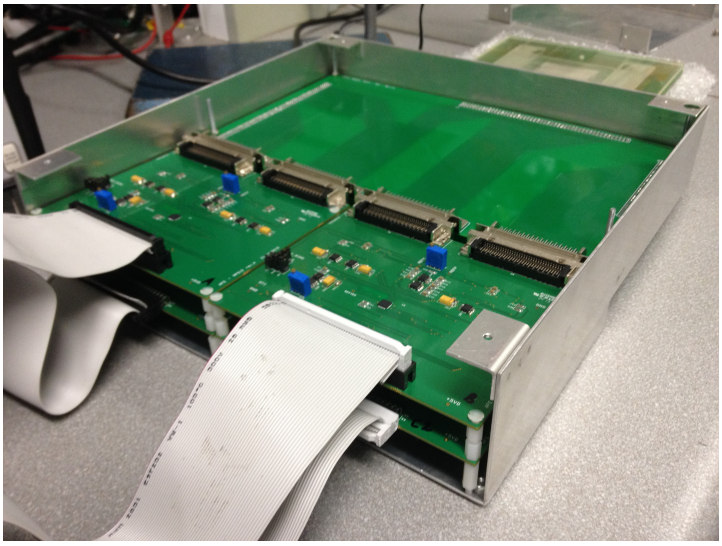

Figure 2.10: DAQ system.

The FPGA manages the USB2.0 link established with the host computer, where a graphical user interface (GUI) called *Romulus* (described in greater detail ahead at paragraph 2.5) and designed at CMRP for EBRT applications provides real-time visualisation and the commands necessary to control the instrumentation. For this reason, the USB link works in two ways: it sends the requirements set from the user via the graphical user interface (GUI) and forwards the signals obtained after the acquisition to the host computer for data storage.

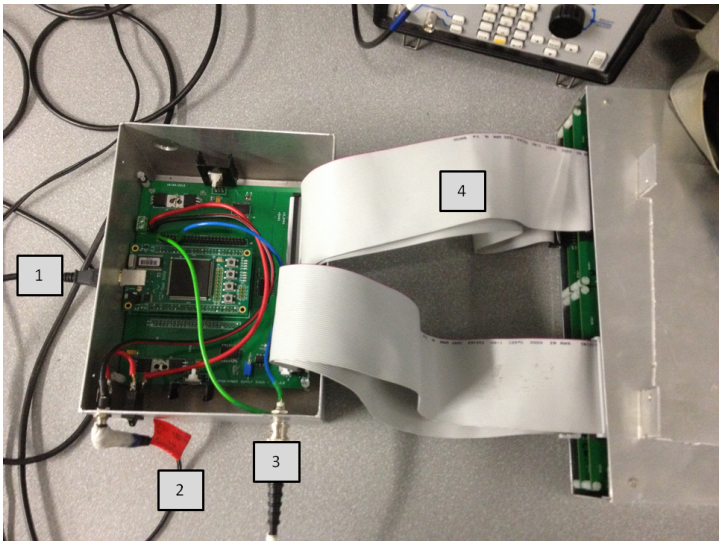

Figure 2.11: FPGA packaging. 1: USB connection; 2: power supply; 3: coaxial cable to the linac; 4 - connection with the ADCs.

Furthermore, the DAQ system allows asynchronous acquisition of the detector signals by the generation of an internal trigger with frequency up to 10 kHz [37]. In fact, it resolves and reports the amount of charge generated within each silicon pixel for each linac pulse: this unique feature is fundamental as it allows the visualisation and the quantitative analysis of the transient dose rate effect of the radiation generated by the linac. For further details about the data acquisition system refer to Fuduli et al. [38].

2.4 Detector packaging

As dosimetry is strongly affected by the scattering and the attenuation of a given radiation field by the materials surrounding the sensitive volume of the detector, particular care has been taken while designing the detector packaging. For this reason, the detector and PCB carrier are designed to avoid the use of high Z contact pads which could result in dose enhancement effect.

Evaluation of water equivalence of the PCB board was performed on the MP512 by placing it at a depth of 1.5 cm in a solid water phantom with 10 cm of backscattering material, at a source to surface distance (SSD) of 100

cm and irradiating the device by 6 MV photon beam of 10x10 cm^2in size, in both face-up and face-down orientations.

The relative difference in response of MP512 of face-up to face-down has been found to be +0.64%±0.1%: this shows that the flexible thin PCB is a valid option of packaging of monolithic 2D detector arrays.

2.5 Romulus graphical user interface

As mentioned at paragraph 2.3, Romulus is the interface software designed at CMRP in order to have an easy representation of the detector readings. As it is a general software used for several detectors at CMRP, it features specific choices and characteristics depending on the particular device (and its relative electronics): in this paragraph, the attention is focused on MP512 and DUO interfaces.

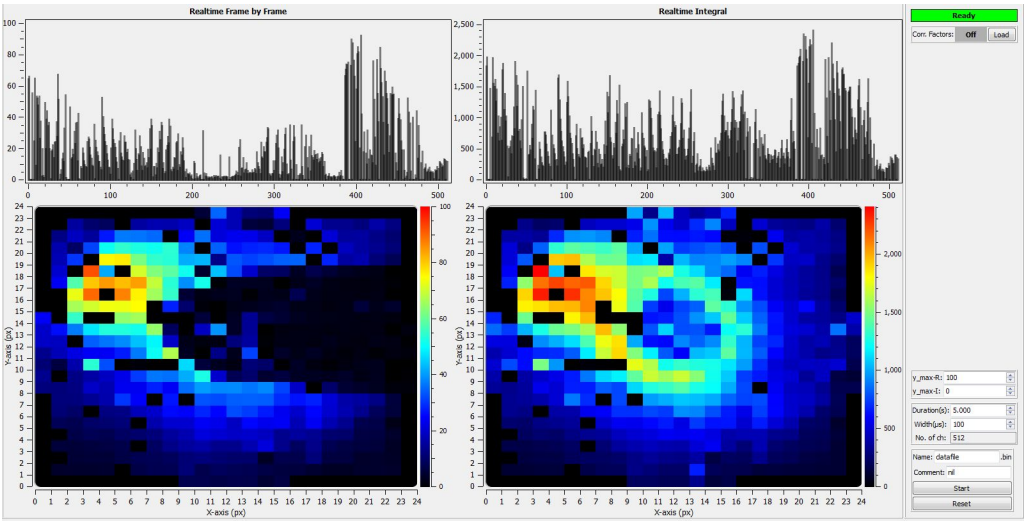

Figure 2.12: Romulus main interface.

The main interface (shown at Figure 2.12) is divided in two different sections: on the left, four windows display the readings of the detector normalised dose, while on the right there is an interactive list of specifications for the launch of the acquisition and process as well as some graphic parameters concerning visualisation of the left zone.

In particular, the four windows can be gathered in two ways:

1. per rows: the first row shows the response of every pixel (512 for MP512 and 505 for DUO) while the second is a graphic representation of the specific detector following a coloured scale from blue (low dose) to red (high dose);

2. per columns: the left column displays a frame every 500 of all the acquisitions, while the right one shows the integral on all single frames (therefore it is updated at each new frame); as the absolute value of the integral response can change (depending on the readings), the vertical axis and the colour scales are not fixed.

Once the acquisition is run, the software saves a .txt file in which readings are stored. In fact, every 512 data correspond to a frame, and frames are recorded one after the other: knowing the correspondence between the list of channels and the physical pixels position (in order to make the design of the PCB easier, they are not in order), it is possible to connect the read value to the proper channel.

In particular, in order to get this correspondence channel-pixel (and get the *mapping* of the detector), a focalised laser beam and an optic system have been used. In fact, using a collimated beam, mirrors and lenses (the setup is shown at Figure 2.13), it is possible to get a spot which is large enough to stimulate a few channels of the detector: thanks to a 2D stepper motor table (whose steps are smaller than the pitch between two channels) manually controlled, the spot can be moved from one channel to the other allowing to follow the movement of the spot on the Romulus display and to reconstruct the proper list of channels.

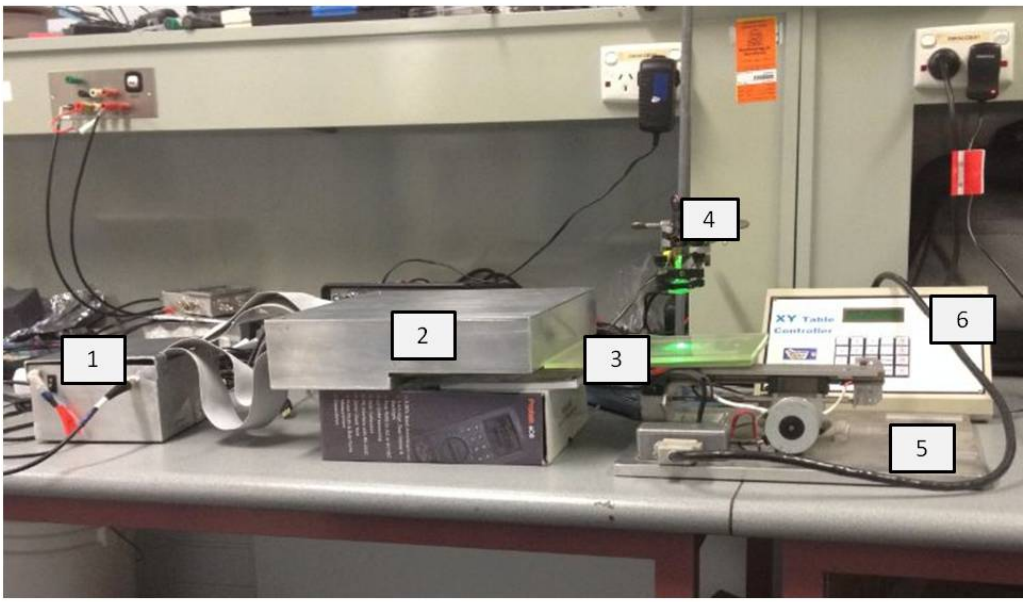

Figure 2.13: Setup for the optic mapping technique. 1: FPGA; 2: DAQ system; 3: MP512 detector; 4: laser, collimator and lenses; 5: sliding step board; 6: manual controller for the sliding step board.

At the same time, Romulus features some postprocessing data analysis tools such as single channel and single frame readings display, detector system equalisation (view paragraph 3.2), beam profile visualisation and basic statistical analysis which can be used during experimental sessions in order to double-check if the acquisition and save processes have run properly.

2.6 Lung anatomy

Lungs are the organs responsible for respiration: in fact, they represent the essential part of the respiratory system, where the gas exchange of carbon dioxide and oxygen occurs.

Figure 2.14 is a transverse section of a human's chest, showing all major organs. Lungs occupy all the thoracic cavity except the mediastinum (the central compartment of the thoracic cage, which includes heart, great blood vessels, bronchi and oesophagus) and are cone-shaped, which makes them fill up the rest of the thorax. In particular, anterior, lateral and posterior lung surfaces lie in close contact with the ribs (they form the costal surface); the apex and the base are in contact with the clavicle and the diaphragm, respectively.

Lungs are connected to the mediastinum by vascular and bronchial attachments through an indentation called *hilum*. As the apex of the heart is slightly pointing to the left of the median plane, lungs differ in size and shape: in fact, the left lung has a concavity called *cardiac notch* which accommodates the heart. For this reason, the left lung is subdivided into two lobes (superior and inferior), while the right one is subdivided into three lobes (superior, middle and inferior).

Globally, lungs largely consist of air spaces: in fact, their tissue is mostly formed by elastic connective tissue: this fact makes them spongy and elastic organs just weighting approximately 1 kg together.

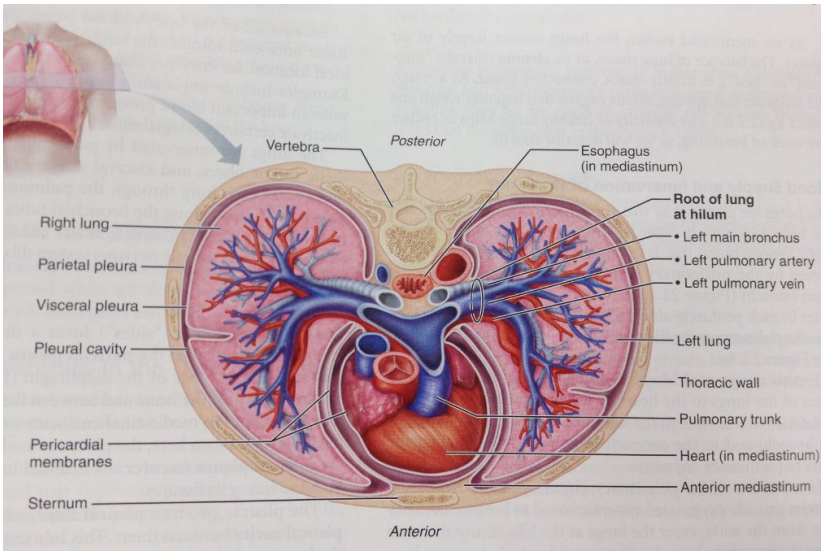

Figure 2.14: Anatomical relationships of organs in the thoracic cavity. The size of the pleural cavity is exaggerated for clarity. [39]

They are surrounded by pleuræ, two thin, double-layered serous membranes: one layer (called *parietal pleura*) covers the thoracic wall and superior face of the diaphragm, continues around the heart and between the two lungs forming the lateral walls of the mediastinal enclosure; the other one (*visceral pleura*) covers the external lung surface, dipping into and lining its

fissures. What is more, pleuræ help separate the thorax into three cavities: the mediastinum in the middle and the two pleural compartments (each containing a lung). This division prevents mobile organs from interfering with another and limits the diffusion of local infections.

However, the main role of pleuræ is the production of pleural fluid, which fills the pleural cavity between parietal and visceral pleura: this lubrificating secretion allows the lungs to slide over the thorax wall during the respiratory act. Although the pleuræ glide easily across each other, their separation is strongly resisted by the surface tension of the pleural fluid. Because of this, the lungs fasten tightly to the thorax wall and are forced to expand and recoil passively as the volume of the thoracic cavity changes during breathing.

2.7 Breathe mechanics

The mechanism of breathing consists of 2 different phases: inspiration (lungs volume increases and air flows into lungs) and expiration (lungs volume decreases and air flows out of lungs). All these mechanisms are then regulated by volume changes caused by natural and forced contraction and relaxation of muscles. If temperature does not change (we can approximate that air temperature changes lightly while travelling from the mouth to the alveoli), to every volume change corresponds a pressure change, as stated by Boyle's law:

$$p_1 V_1 = p_2 V_2 \tag{2.1}$$

where 1 and 2 identify respectively the beginning and the end of the process, and the changing is regulated by flowing gases.

In order to describe breathe mechanics, it is useful to analyse all different pressure levels reached in all chest cavities (Figure 2.15):

1. *intrapulmonary* (*intra-alveolar*) *pressure* pressure rises and falls with breathe phases around the atmospheric pressure;

2. *intrapleural pressure*: it fluctuates following the intrapulmonary cadence, but is always at lower level than the intrapulmonary one (it can be in depression if relation to the atmospheric pressure);

3. *transpulmonary pressure*: it is the difference between intrapulmonary and intrapleural pressures.

Effectuating a force analysis, two forces are found to be pulling the thorax away from the thorax wall: due to their elasticity, lungs tend to assume the smallest possible size; what is more, alveolar fluid molecules attract each other (surface tension effect) making the alveoli as small as possible. On the other hand, chest wall is naturally elastic and tends to pull the thorax outward, enlarging the lungs. For this reason, pleural fluid must be pumped out of the pleural cavity in order to create a depression zone that keeps secure pleuræ together (it works exactly like a drop of water

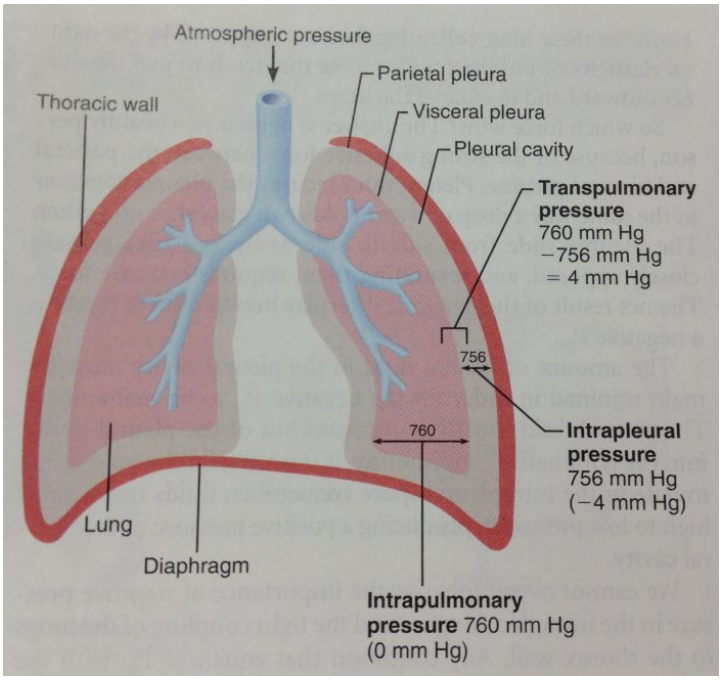

Figure 2.15: Intrapulmonary, intrapleural and transpulmonary pressures. [39]

holding two glass slides together): here is the cause of the existence of the transpulmonary pressure.

2.7.1 Inspiration and expiration

Analysing properly a respiration process, everything is governed by involuntary and voluntary muscles movement. In fact, as far as the diaphragm contracts, it moves downwards, making the superior-inferior dimension of the thorax increase. At the same time, intercostal muscles contract: the rib cage lifts and pulls the sternum upwards, giving an expansion of the thorax laterally and a modest change along the anteroposterior plane. The result of all these movements is an expansion of a few millimetres along each plane, leading to a decrease of the intrapulmonary pressure, which makes fresh air flow in: in particular, the most significative changes are given by the action of the diaphragm. Accessory voluntary muscles can further increase the thoracic volume: this process is called forced inspiration.

The expiration process principle is the same as inspiration: expiratory muscles contract, make the lungs recoil and the expired air flow out. An extra expiration can be realised if abdominal wall muscles are contracted: this forced expiration makes lungs assume a smaller volume than the one at rest.

2.7.2 Breathe movement profiles

Knowing the above-mentioned mechanics details, through a 4D CT scan of a real patient, it is possible to extract the temporary profiles that describe

lungs movement patterns. As specified in the previous paragraph, the movement along the sagittal plane is, on first approximation, negligible: for this reason, our study concentrates only on movements along the coronal and the coronal and the transverse plane.

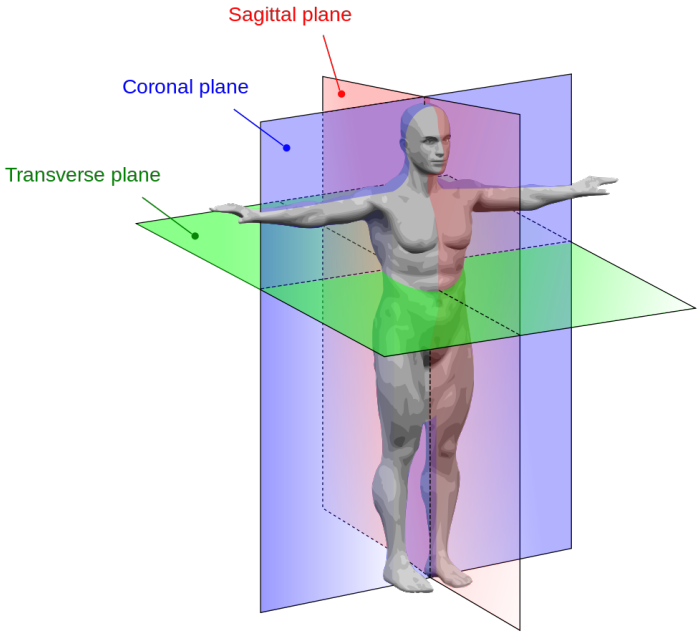

Figure 2.16: Cartesian coordinates. [40]

In order to have a simpler description of the movements, it can be useful to define a three-dimensional Cartesian coordinates system as displayed in Figure 2.16: negligible movement is then along the z axis. This is the reason why it is not necessary to use 3D detectors, but a 2D device is sufficient to play this role. At the same time, the x and y profiles (Figure 2.17) show synchronicity in time (peaks and valleys coincide in time) but the absolute displacement is greater for y axis. In fact, the maximum distance along y is about 10 mm.

2.8 Movable lung phantom

In order to mimic as much as possible the anatomical structure and movements of lung tumors, the *Movable Phantom* has been designed by CMRP taking care of materials, sizes and proportions. All the timber and PMMA pieces have been rendered using SolidWorks 2010 (Dassault Systèmes, France) and manufactured by the University of Wollongong mechanical workshop. The different components of the power supply and motion management have been designed and integrated by the CMRP team.

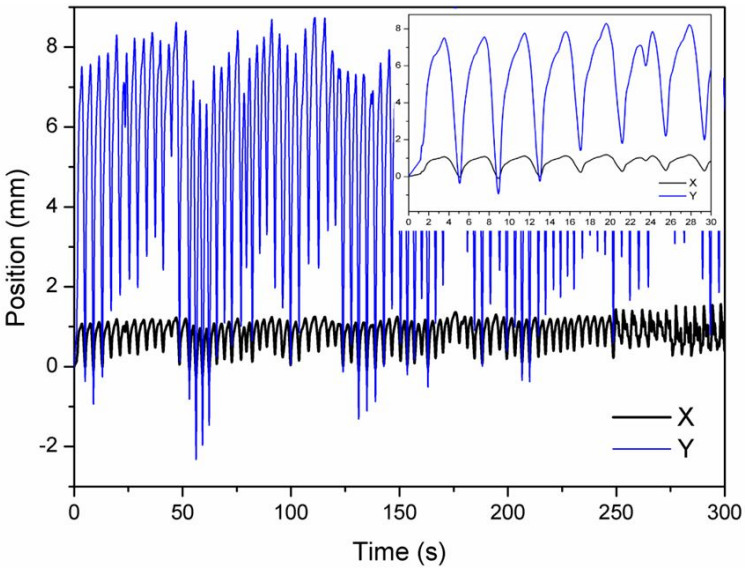

Figure 2.17: Lung temporal patter components extracted from a patient 4D CT scan. The inset window shows the details of the first 30 seconds of the motion.

2.8.1 Phantom structure

The phantom has a symmetric structure (it takes into account only one lung, and does not copy the entire thorax) and can be divided in a fixed and a moving part.

The base is constituted by a PMMA plate to which all the other fixed components are fixed: in particular, two vertical PMMA parallelepipeds and an horizontal cover simulate the presence of scheletal muscles of the thoracic cage (pectorals). In order to make the movement management easier, "ribs" do not move, but the relative movement of the inner timber lung phantom gives the same global effect.

The lung is made of pine timber: this is a light material that satisfactorily mimics lung tissue from the mechanical and radiative point of view.

In fact, two different pieces of wood hold the detector fixed on the plexiglass board between them: for this reason, in order to simplify the description, the upper and lower pieces are called respectively "top" and "bottom". Their structures are different, because the top piece (Figure 2.18) has to accommodate the detector: for this reason, it has a recess of 7x7 cm^2 (the size of DUO being 5.2x5.2 mm^2) whose deepness is 2 mm. In order to make the structure more compact and avoid vacuums, the top piece also presents a 0.5 mm step that helps arresting the PCB board. As the detector is then plugged in the reading system and they both have to move together, two extra plastic pins have been included in order to make the structure more firm and avoid relative movements between the detector and the timber pieces.

The two timber pieces and the detector are fixed to two PMMA pieces: their aim is to mimic all soft tissues in the mediastinum that surround the lung. The whole structure is held together with a few ISO M4 and M5

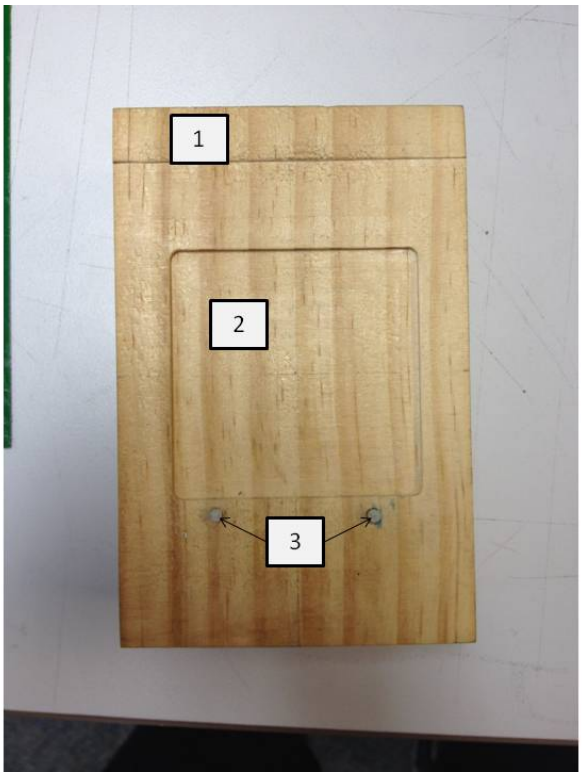

Figure 2.18: Top timber piece. 1: 0.5 mm step; 2: 7x7 mm^2 recess; 3: extra plastic pins.

nylon screws: the choice of this material is not random, as it allows to avoid metal inside the timber (it would have no physiological correspondence and would affect the results because of its properties with respect to radiation beams). Underneath these two components, two slices of Teflon are glued: this material helps the structure to glide (it reduces the friction between PMMA). What is more, the PMMA structure does not wear out: if the slices get too thin, they can be easily removed and replaced.

This whole moving block is then fixed by some plastic screws to a PMMA horizontal bar: this piece is linked to a Step-syn stepping motor (SANYO DENKI, Japan) via a shaft that transmits the movement from the engine to the moving phantom, the stepping motor being fixed to the PMMA base.

The stepping motor is a device which is able to split an entire rotation in 200 steps (1.8 deg per step): every step corresponds to a displacement of the phantom as the shaft transforms the circular motion in a linear motion along one direction (in this specific case, the Y axis of the detector). Obviously, because of the kynematics structure of the system, the conversion from angle

to displacement is not constant but is described by the following equations:

$$\begin{cases} x_b(t) = r \cdot cos\phi(t) \\ y_b(t) = r \cdot sin\phi(t) \\ x_B(t) = r + x_b(t) = r \cdot (1 + cos\phi(t)) \\ y_B(t) = r - d + y_b(t) = r \cdot (1 + sin\phi(t)) - d \\ \overline{AB} = D = constant \\ D_x(t) = D \cdot cos\theta(t) \\ D_y(t) = D \cdot sin\theta(t) \\ \theta(t) = sin^{-1}\left(\dfrac{D_y(t)}{D}\right) = sin^{-1}\left(\dfrac{r \cdot (1 + sin\phi(t)) - d}{D}\right) \\ x_A(t) = D_x(t) + x_B(t) = D \cdot cos\theta(t) + r \cdot (1 + cos\phi(t)) = \\ \quad = D \cdot cos\left\{sin^{-1}\left(\dfrac{r \cdot (1 + sin\phi(t)) - d}{D}\right)\right\} + r \cdot (1 + cos\phi(t)) \end{cases} \tag{2.2}$$

The dimensions are represented in Figure 2.19: $x_A(t)$ is the displacement as a function of time that describes the lung pattern motion, D is the length of the shaft, r is the radius of the rotating discus and angle ϕ is determined by the number of steps run my the stepping motor.

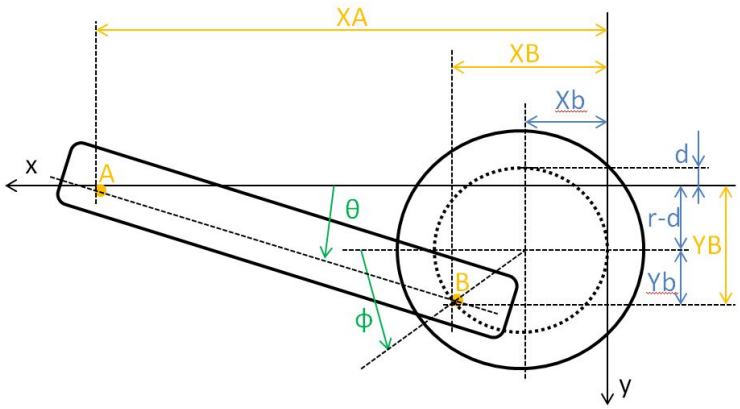

Figure 2.19: Description of the kinematics of the moving system.

Figure 2.20 shows the picture of the whole phantom structure with the detector between the two timber pieces.

2.8.2 Phantom movement

Figure 2.21 represents Phantom connected to the slow control system.

The main components are a G203V digital step drive (Geckodrive Inc., Tustin, CA, USA), a XEM6001 Opal Kelly FPGA board (Opal Kelly Inc., Portland, OR, USA) and a power supply system: all these elements are linked to a PCB via appropriate cabling (which supply power and allow data transfers) and are contained in a box shown in Figure 2.22.

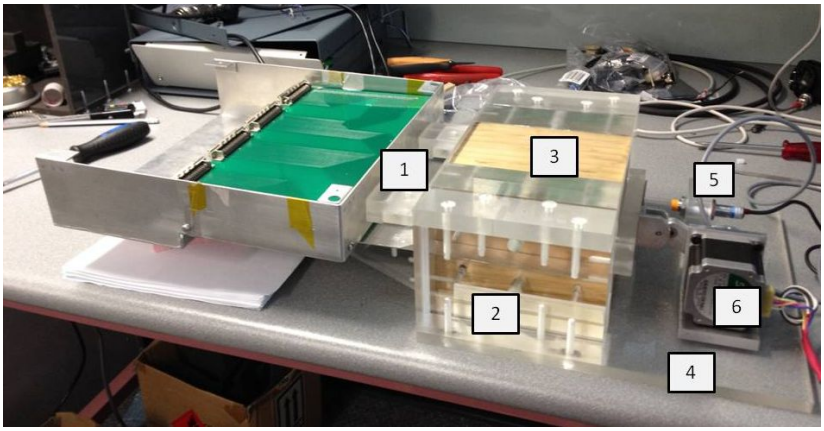

Figure 2.20: Phantom structure. 1: detector and DAQ system; 2 :PMMA thoracic cage; 3: top and bottom timber pieces; 4: PMMA base; 5: magnetic sensor (view section 2.8.2); 6: stepping motor.

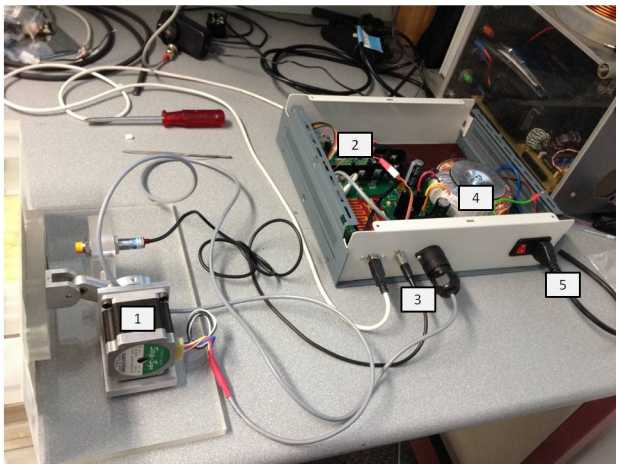

Figure 2.21: Connection between the phantom and the movement management elements. 1: digital step drive; 2: FPGA; 3: magnetic sensor wiring; 4: tension transformer; 5: power supply.

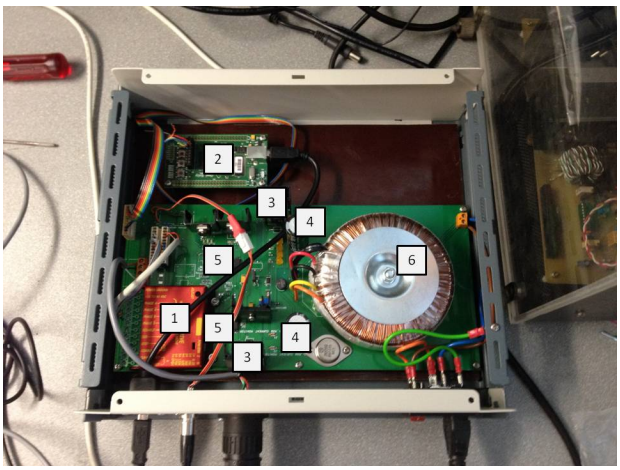

Figure 2.22: Detail of the motion management system. 1: motor stepper; 2: FPGA; 3: dissipators; 4: capacitors; 5: diodes; 6: tension transformer.

The whole system is supplied power via a standard power socket of the electric network: the voltage is converted from 250 to 18 V thanks to a thoroidal transformer (detail 6 at Figure 2.22). As this is still an alternate current, two diodes (detail 5) convert it in direct current by inverting the negative part. In order to make this tension more stable and smooth, two capacitors (detail 4) accumulate or supply electric charge as needed. The PCB applies the necessary voltage to every component of the motion management system. Figure 2.23 shows the direct current (black curve), the effect of the diodes (red curve) and of the capacitors (blue curve).

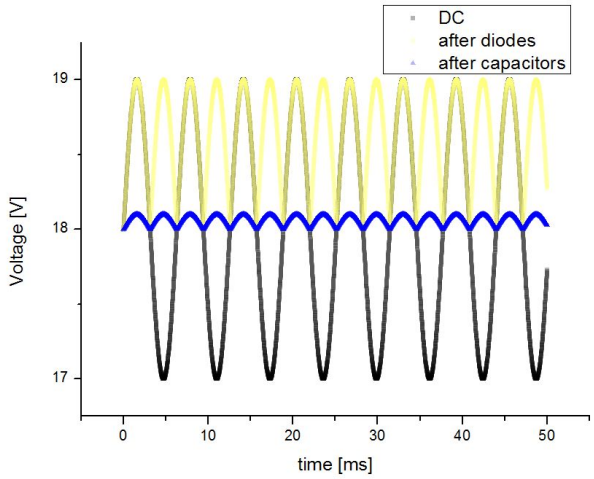

Figure 2.23: Changes in the electric current due to the diodes and the capacitors.

The FPGA is linked via a USB cable to a laptop: the latter, basing on the lung movement profile (Figure 2.17), generates a file consisting in a list of positions and the corrisponding times which are sent to the FPGA. As the clock time of the stepping motor is $20\text{x}10^{-3}$ s while the clock time of the FPGA is 10^{-7} s (10000 times faster), the FPGA is able to set the number of steps that the stepping motor has to run at every clock time. Changing the number of steps in a fixed time and the direction of the rotation, the motor is able to reproduce the lung profile movement along the Y axis.

In particular, the number of steps and the direction are sent from the FPGA to the motor stepper, which is able to split one motor step in 10 steps, leading to a minimum angle of 0.18 deg per step. At the same time, in order to avoid the overheating of the motor, this device enables or disables it.

Finally, the system features a magnetic sensor (detail 5 at Figure 2.18) which is placed on the PMMA base in front of the phantom. This device sends towards the phantom some radiowaves that are reflected by a metallic piece glued on the PMMA horizontal bar and read by the sensor. When the time needed for the waves to travel back to the sensor is less than a certain value (which means when the distance between the sensor and a metallic piece is smaller than a fixed value $\bar{d}$), a red light turns on and a signal is

sent to the FPGA. In fact, the sensor does not work as a meter, but is a physical representation of the logic *if-else* condition:

$$\begin{cases} if \text{ distance} < \bar{d}: & \text{light on} \\ else: & \text{light off} \end{cases} \tag{2.3}$$

In particular, this sensor has been implemented as it is necessary to run a specific "homing" procedure before the phantom starts its real movement: its aim is to make the movement start from the same place in order to have uniform movement profiles. To achieve this, the phantom moves forwards and then backwards up to a fixed position where the light turns on: at this point, the system starts counting how many steps it needs to get to the minimum distance from the sensor and then again to the point where the light turns off without changing the rotation sense, which makes the light turn on again. In order to get back to the home position, the stepping motor runs half of the number of steps counted but in the opposite direction. Figure 2.24 plots a profile of the distance between the metallic piece and the sensor as a function of time and shows the changements in light status as well as the final homing position.

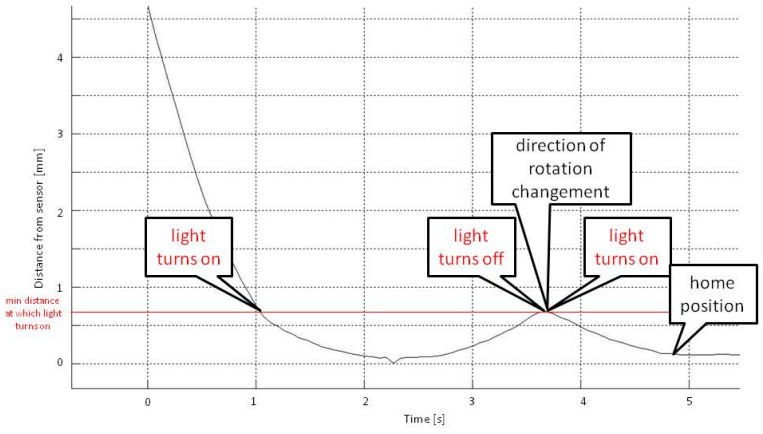

Figure 2.24: Phantom movement management elements and power supply. 1: stepper motor; 2: FPGA; 3: magnetic sensor wiring; 4: transformer; 5: power supply. This distance profile is obtained using the camera system described at 6.1.

Chapter 3

Static characterisation of MP512

The second chapter has shown a detailed description of all the instrumentations that are the object of this thesis. Chapter 3 presents the experimental work in terms of methods, specific materials and obtained results. In particular, in this chapter, the attention is focused on the static characterisation of MP512.

Nevertheless, the first part of the chapter is about radiochromic films and the procedure which must be adopted to properly use them. This device has not been developed at CMRP or modified during this project. However, it has been used in all the experiments to verify the goodness of the results obtained with MP512 as it features interesting properties in terms of spatial resolution. Therefore, it is presented before MP512 characterisation.

The second part describes a basic characterisation consisting in pixels response uniformity (paragraph 3.2) and dose linearity (paragraph 3.3).

As stated in [41], percent depth dose (PDD), output factors (OF) and beam profiles are generally the parameters required for a full characterisation of the beam. For this reason, the second part of this chapter presents the study of PDD measurements (3.5), OF measurements (3.6) and small field beam profiling (3.7) for beam sizes relevant to SBRT and SRS, benchmarked against conventional radiation detectors such as ionisation chambers and radiochromic films.

All these experiments have been run at the Illawarra Cancer Care Centre (ICCC) at the Wollongong Hospital, using a Varian 2100EX medical linear accelerator.

3.1 EBT radiochromic films

As pointed out in section 1.8.3, *Gafchromic EBT films* (ASHLAND, Wayne, NJ) represent the golden standard concerning the spatial resolution achievable nowadays. This is why the most currently used approach to small field quality assurance consists in delivering the planned dose to a phantom containing a piece of radiochromic film and then comparing the 2D dose

distribution calculated by the treatment planning system (TPS) with the value measured by films. What is more, these detectors are available in foils and can be handled in visible light and even immersed in water for short periods, allowing their use in water phantoms.

3 different generations of EBT film exist:

1. EBT film was the first type of radiochromic film suitable for the use with doses as low as the typical doses occurring in radiation therapy.

2. EBT2 film incorporates a yellow marker dye in the active layer and asynthetic polymer as the binder component.

3. EBT3 films are made by laminating an active layer between two identical polyester layers, which makes the product more robust and allows water immersion. While the active layer composition and response is unchanged, the real EBT3 improvement are: the symmetric structure that makes the detector angular independent (allowing to avoid the potential errors in optical density measurements due to scanning side in EBT and EBT2), the matte polyester substrate that prevents Newton's Rings formation, and the presence of fiducial marks that allow for the film automatic alignment.

The procedure required for this device is detailed hereafter and refers to the internal protocol of the New South Wales (NSW) as well as to [42]. Basicly, it consists in 2 steps: the first one is a scanning performed before irradiation (called "pre-scanning") while the second one is another scanning carried out after irradiation (hence said "post-scanning"), the first one being functional to the second one.

Particular care has to be taken while handling these devices, as their structure is quite sensible. Therefore, in order to cut the film foils into smaller pieces, no scissors have been used, because they might have detached the different layers of the film: in their place, a paper trimmer has been used. What is more, all films have been handled with medical latex gloves and stored in special tissues and antiscratch bags, in order to avoid any fingermarks or scratches on the film surfaces, as they might alter the film response to the scanner and the photon beam. At the same time, the virgin foils as well as all the cut pieces have been stored in dark rooms in order to avoid any accidental darkening reaction.

In the context of this thesis, EBT3 films were used as the benchmark for measurements and characterisation of the beam profiles. Therefore, the protocol described above has been run for the static characterisations of MP512 and DUO as well as the dynamic caracterisation of MP512. For each of them, the pre-scanning has been performed at least 3 days before the irradiation and the post-scanning at least 3 days after the irradiation, in order to guarantee that the whole darkening process has finished. An important point is that the irradiation of film and silicon detector have been performed in the same experimental session in order to mantain the same experimental conditions.

3.1.1 Pre-scanning

This first step aim is to describe how optical density changes in function of given dose and obtain a *calibration curve* in order to characterise the response of films in terms of dose. To achieve this objective, a set of 10 portions of EBT3 films is cut into sections of 3x3 cm^2, and every single portion is assigned a serial number from 1 to 10 and an oriented arrow in order to mantain the same orientation in all the following steps. To place the films at the same center region of the scanner, an acetate sheet was previously cut to be used as a template (Figure 3.1). All these procedures are necessary to reduce scanner induced nonuniformity.

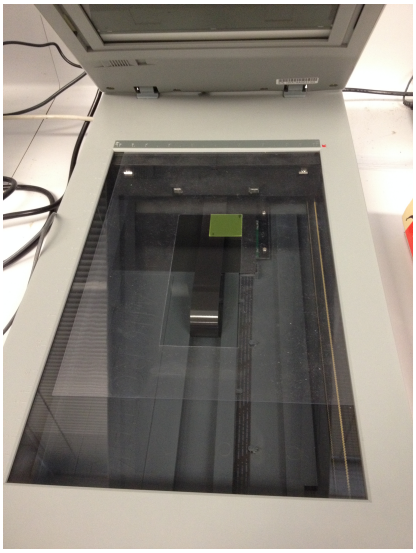

Figure 3.1: One 3x3cm^2 film sample is placed in the scanner inside the acetate template.

The scan is performed in 48-bit RGB color mode with the scanning resolution of 72 dpi (equivalent to a pixel size of 0.353 mm) with a Microtek ScanMaker i800: in order to ensure a proper warm up of the machine and hence a better film analysis consistency, each film is scanned six times and only the last three scans are kept to perform the following steps [43]. Particular care is taken to scan the film in the same orientation at the central region of the flatbed to reduce non-uniformities [44].

The analysis of the images is done using both the Image J version 1.43U (National Institute of Health, USA) and MATLAB (The Math Works Inc., Natick, MA) software tools. A 3x3 pixels two dimensional median filter is applied onto the image to reduce image noise [45]. By this mean, three background intensities I_0 are determined from image pixel values of the film scan: red, green and blue channels. Their values are measured from image pixel values of the film scan with associated statistical errors σ_I and σ_{I_0}, respectively; standard deviations are calculated across three image data sets (repeated scans of the same film). At the same time, a set of portions of 10x10 cm^2 (Figure 3.2) is prepared and prescanned following the same protocol.

Figure 3.2: One 10x10mm^2 film sample. The serial number 12 and the orientation arrow are visible.

3.1.2 Post-scanning

All the calibration samples are positioned at the centre of the solid water phantom at isocentre and submitted to beam profiles of 10x10 cm^2 with different dose values going from 300 to 2000 MU. Figure 3.3 displays the 10 calibration samples after irradiation.

Figure 3.3: A set of 10 calibration samples after irradiation.

At the same time, depending on the aim of the experiment, every 10x10 cm^2 sample has been irradiated with a proper beam profile.

After this, the same scanning procedure has been adopted. The final result is the obtaining of the values of the intensity I for red, green and blue channels.

3.1.3 Data analysis

The pursued information consists in the optical density (OD), which is defined as

$$OD = log_{10}(\frac{I_0}{I}) \tag{3.1}$$

where I_0 and I are the background intensity and intensity values, respectively obtained from pre-scanning and post-scanning procedures. Calculating these values for the 10 calibration film portions (each referring to a different given dose), the calibration curves D(OD) are obtained (Figure 3.4). This is possible because in the window of interest, this function is bijective.

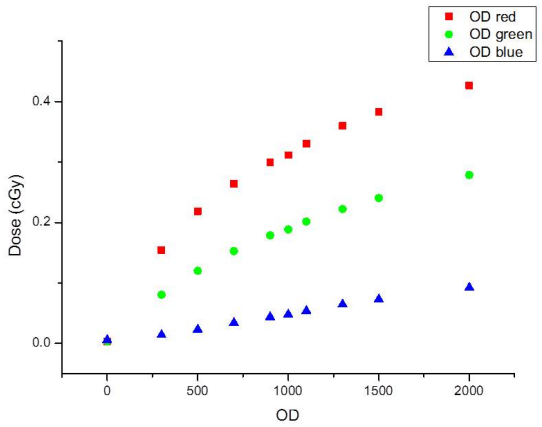

Figure 3.4: A set of blue, green and red calibration curves.

A second-order polynomial function is fitted to the measured data of the dose calibration curve,

$$D = A + Bx + Cx^2 \tag{3.2}$$

where the polynomial function depends upon associated fitting constants: A, B, and C with errors σ_A, σ_B, and σ_C, respectively. The standard deviations are determined statistically from the repetition of the fitting process across three film scan image sets. The final error (in cGy) in the calculated dose values from the EBT3 film measurements is thus dependent upon the values and errors associated with the measured quantities of I_0 and I, as well as the fitting constants of the second-order polynomial, as shown in equation 3.3.

$$\begin{aligned}\sigma^2_{Dose} = &[(\frac{B}{I_0 \times ln10} + \frac{2C \times ln(\frac{I_0}{I})}{I_0 \times ln^2 10}) \times \sigma_{I_0}]^2 + \\ &+ [(\frac{-B}{I \times ln10} + \frac{-2C \times ln(\frac{I_0}{I})}{I \times ln^2 10}) \times \sigma_I]^2 + [\sigma_A]^2 + \\ &+ [(log_{10}(\frac{I_0}{I}) \times \sigma_B)]^2 + [(log_{10}(\frac{I_0}{I}))^2 \times \sigma_C]^2\end{aligned} \tag{3.3}$$

In order to conduct the optical analysis, only the red channel has been used for pixel to dose conversion. This is due to the fact that, as shown in Figure 3.4, the red one shows a greater reliability as the dose gets bigger.

Using this curve, the direct conversion of pixel value to optical density and then to dose in cGy has been performed for every pixel of the 10x10 cm^2 portions, leading to an Excel sheet similar to the one shown in Figure 3.5.

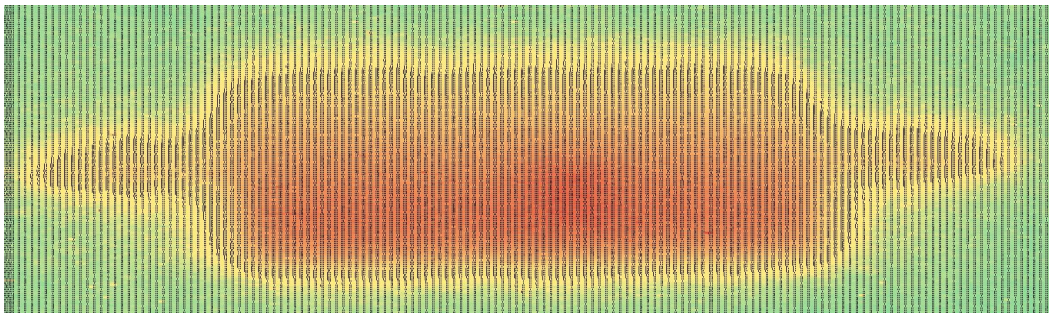

Figure 3.5: An Excel file showing a calibrated scan. Dose grows from green to red.

In fact, every cell represents a pixel in the film: the graduated scale goes from green (minimum dose) to red (maximum dose) and supplies a visive way to describe the spatial distribution of the integral dose provided to the film piece.

3.2 Pixels response uniformity

MP512 consists in 512 pixels implanted on bulk p-type silicon substrate and connected to a readout multichannel electronics. Therefore, the response corresponding to each channel is the combination of the sensitivity of each specific pixel and the gain of its corresponding pre-amplifier channel. This combination can generally lead to small variations of the response from pixel to pixel.

Typically, this issue can be addressed by an *equalisation* procedure: it consists in the calculation of a multiplication factor array which can be used to equalise the response of the entire system as reported earlier by Wong et al. [46].

The equalisation factor is obtained by irradiating the device at 100 cm SSD in a solid water phantom by a 20x20 cm^2 field of 6 MV energy photons at depth 10 cm. At this depth, the dose cross profile of a linac equipped with the flattening filter is considered flat (allowing the hypothesis of uniform stimulus for all channels) and the response from MP512 is recorded, generating the vector X_i. The average response from all the channels <X> is then calculated. The equalisation factor vector F_i and the equalised detector response X_{eq-i} are then

$$\begin{cases} F_i = \dfrac{X_i}{< X >}; \\ X_{eq-i} = \dfrac{X_i}{F_i}. \end{cases} \tag{3.4}$$

The uniformity of the array is calculated as percentual differential response from each pixel:

$$X_{\%} = \frac{X_{eq-i} - X_{eq-(11,12)}}{X_{eq-(11,12)}} \times 100 \tag{3.5}$$

where $X_{eq-(11,12)}$ is the response of the central pixel after the normalisation procedure described above. Results can be visualised by a statistical histogram as shown in Figure 3.6.

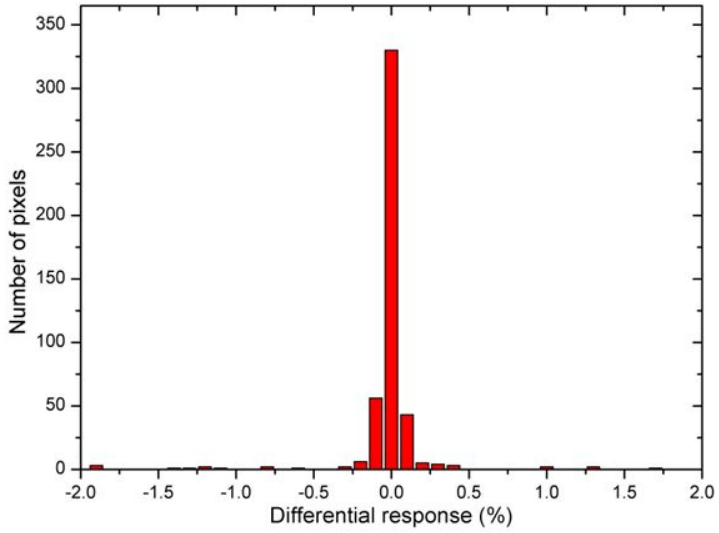

Figure 3.6: Differential response of MP512 after equalization.

In fact, it displays the uniformity statistics of MP512 response after the equalisation factors were applied. Uniformity is evaluated considering two standard deviations from the mean value as small as 0.25% after equalisation has been applied.

3.3 Dose linearity

Verification of the linearity response with dose is performed under conditions above by registering pixels response for each 50 MU increments for the total accumulated irradiation dose up to 500 MU.

Figure 3.7 shows the dose linearity of MP512 for accumulated dose in the range from 50 to 500 MU. The adjusted regression coefficient R^2 is 0.9988, which is a satisfactory result; vertical error bars are calculated by two standard deviations over 5 repetitions. From the slope of the linear fit, the conversion factor from counts to dose is 1825.19 counts/cGy which corresponds to 175.2 pC/cGy.

3.4 Dose per pulse measurements

The dose per pulse dependence (DPP) measurements (also called dose rate dependence) are made for the range going from $0.9{\cdot}10^{-5}$ to $3.4{\cdot}10^{-4}$ Gy/pulse.

This is achieved using a field size of 10x10 cm^2 at 6 MV with a fixed dose rate of 600 MU/min and changing the source to surface distance and depth of the detector in a water equivalent phantom in order to take advantage

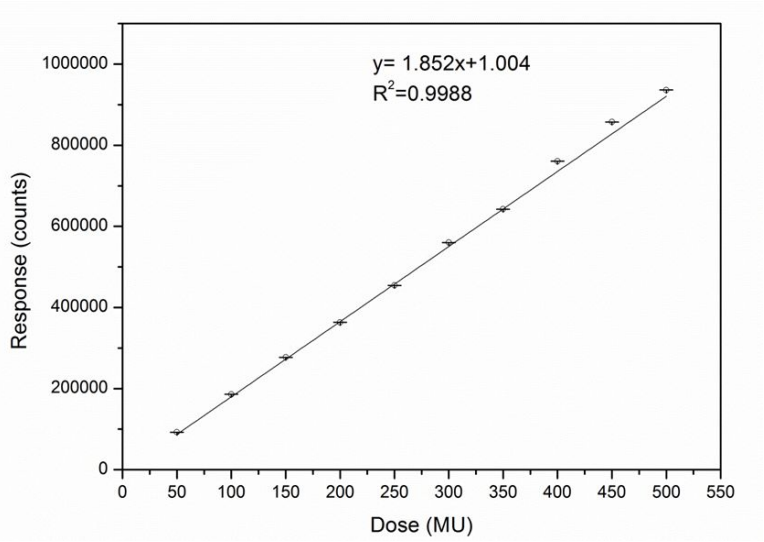

Figure 3.7: Accumulated dose response of the central pixel. The solid line represents the linear fit.

of the $\frac{1}{r^2}$ decrease factor of the intensity of the beam (as pointed out at paragraph 1.7.6).

The dose per pulse reference measurement is performed using an ionisation chamber CC13 at d_{max} and the response from MP512 was normalised to the chamber response ($2.78 \cdot 10^{-4}$ Gy/pulse).

This kind of characterization of DPP by changing the depth of the detector in a phantom can potentially be affected by the variation of the response of the detector with the spectrum of the radiation. Relying on the fact that MP512 is energy independent up to a depth of 25 cm (percentage depth dose analysis, paragraph 3.5), in order to determine the very low DPP, the depth has been kept constant to 25 cm and the source to surface distance (SSD) has been varied from 90 cm up to 350 cm as suggested by [47] and [48].

Figure 3.8 shows the dose per pulse response of MP512, normalised to $2.78 \cdot 10^{-4}$ Gy/pulse (which represents the response of the ionisation chamber at d_{max} for a 6 MV photon beam, field size of 10x10 cm^2). The error bars representing the uncertainties of the MP512 measurements are two standard deviations.

For each dose rate, the response of the MP512 is normalised to the dose measured by the ionisation chamber placed next to MP512. This is possible because it can be assumed that the ionisation chamber is dose rate independent.

The results obtained (maximum DPP dependence is approximately 5% in the whole range of dose rate evaluated) are in substantial agreement with the data measured by Zhu et al. [48] on commercially available single diodes for dosimetry in radiotherapy and manufactured on p-type silicon substrate.

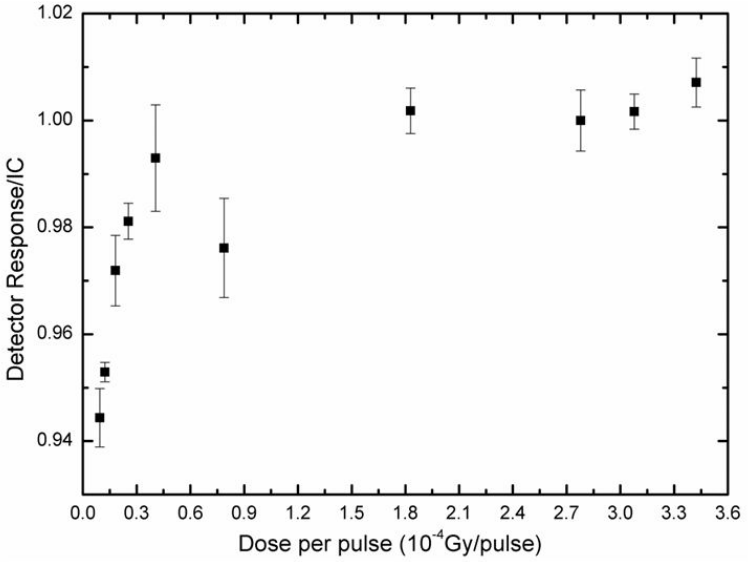

Figure 3.8: Dose per pulse response for the MP512 normalised to the dose per pulse of 2.78x10-4 Gy/pulse. The X axis represents the dose per pulse in order of 10^{-4} Gy/pulse.

3.5 Percentage depth-dose

To run this test, MP512 is inserted into a PMMA holder composed of a slab of 5 mm on top and on the bottom of the detector. In order to provide the proper scattering conditions, sections of 30x30 cm^2 of solid water were used: in particular, a slab of 10 cm was used as backscattering material, while several slabs were used to obtain the depth dose profile from 1.5 cm up to 30 cm depth. The minimum depth of measurements was 5 mm water equivalent depth (WED).

The entire setup is irradiated with 100 MU by a field of 10x10 cm^2 at 100 cm SSD by a 6 MV photon beam.

Under the same experimental conditions (in solid water), a Markus ionisation chamber (PTW Freiburg - Germany) is irradiated: its readings are compared with measurements taken by MP512 as a benchmark.

This comparison is displayed in Figure 3.9: the observed maximum difference between PDDs is approximately $\pm 1\%$. Error bars are calculated as two standard deviations over five repetitions.

3.6 Output factors

The *output factor* (OF) is defined as the ratio of dose measured in the centre of the field per MU at a specific field size to the reference field size [43].

Within this study, the reference field size is 10x10 cm^2, measured at isocentre (10 cm in depth at SSD of 90 cm) [43]. The output factor is calculated by acquiring the response of the detector in the central pixel (row 11, column 12) for field size ranging from 0.5x0.5 to 30x30 cm^2.

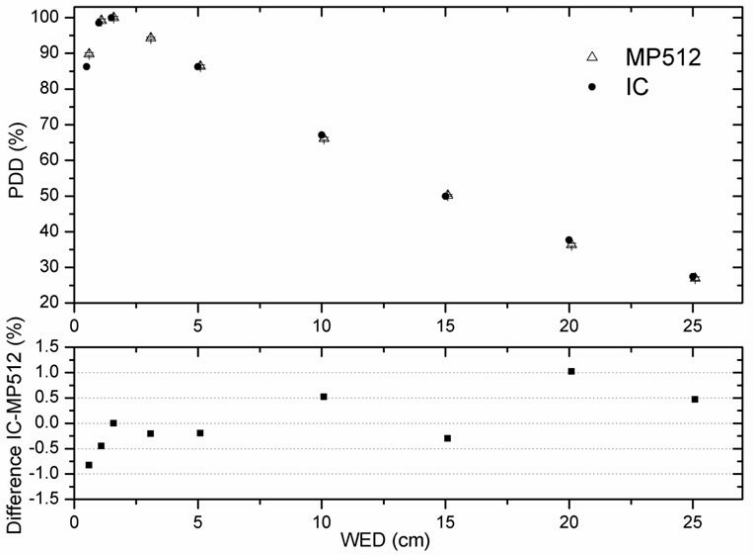

Figure 3.9: PDD of 6 MV photons, 10x10 cm^2 field measured with MP512 and comparison with Markus ion chamber.

The output factor measured by MP512 is directly compared with the MOSkin: this is a silicon MOSFET detector (paragraph 1.8.2) developed for skin dosimetry [49] [50]. Its main advantage is the smallness of its sensitive volume (approximately 3×10^{-6} mm^3), the minimal size of silicon die (approximately 0.5 mm^2) and its water equivalent depth (70 μm). It is mounted in a fully tissue equivalent packaging which avoids wire bonding and high Z materials in order to minimise the potential radiation field perturbation associated with OF measurements. The MOSkin measurements have been carried out at the British Columbia Cancer Agency (BCCA), Victoria, British Columbia, Canada following the AAPM TG-51 protocol: MOSkin has been placed at the isocentre in a solid water phantom (RMI Gammex) at depth of 10 cm. A 6 MV photon beam was delivered from a Varian 21EX medical linear accelerator for this testing and normalised to the 10x10 cm^2 field size.

At the same time, OF measurements were taken using EBT3 films.

These results are shown at Figure 3.10: it displays the response of the three detectors as a function of the field size

For field sizes smaller than 1x1 cm^2, it always shows an over-response (it is never exceeding 4% though). This effect has been observed for point silicon diodes as well, and is caused by the perturbation of the radiation field by the silicon and the package material of the diode. In fact, while decreasing the field size, the relative portion of the beam directly interacting with silicon and surrounding materials increases, leading the electrons scattered from silicon and packaging material to take a heavier role in the response of the detector. On the other hand, the large field response is dominated primarly by electrons scattered from solid water.

This problem can be minimised by reducing the size of the non-tissue equivalent detector and surrounding packaging. In fact, when a very small

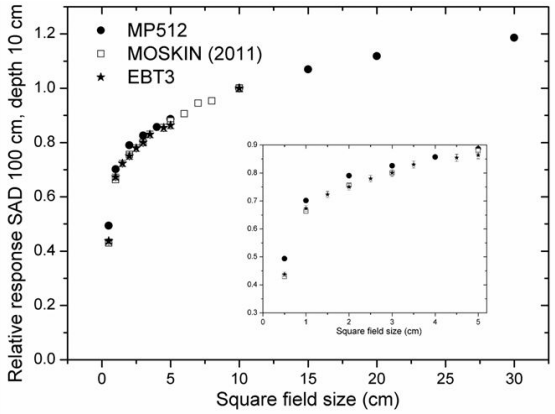

Figure 3.10: Field size dependence response of MP512, MOSkin and EBT3 film normalised to response at 10x10 cm^2 field size. The inset window shows a detail for field sizes smaller than 5x5 cm^2.

size point silicon detector, surrounded by no high Z materials (such as the MOSkin) is used to measure the output factor, the over-response almost disappears. Indeed, the MOSkin shows excellent agreement with EBT3 films: the response difference is always within 1.5%. This is mainly due to the fact that MOSkin's "drop-in" technology adopts only quasi-water equivalent materials, minimising the effect of dose enhancement of materials with high atomic number. Furthermore, it is possible to compensate for the over-response of the MP512 for these small field sizes using a small air gap above each pixel to ideally match to EBT3 film [51] [52].

OF measurements taken by MP512, MOSKin and EBT3 films were also compared with several detector studies taken by several research groups worldwide using commercial detectors in the same experimental conditions: Farmer ion chamber, Pinpoint ion chamber, Diamond PTW 60003, Scanditronic diode unshielded. Besides the fact that these measurements have been taken by different linacs, the comparison at Figure 3.11 shows that the results presented in this thesis fit nicely with the trend obtained by diverse detectors.

Both ionisation chambers exhibit a lower response when compared to other detectors: this is due to the averaging effect of the sensitive volume of 0.6 and 1.3 cm^3 respectively. Finally, for field sizes equal to 1x1 cm^2 and larger, the MP512 results agree generally within 1%.

3.7 Beam profile measurement

A beam profile of an X-ray photon beam can be divided in three parts [19]:

1. *penumbral region*: region included between 80 and 20% of the maximum dose intensity (blue areas in Figure 3.12);

2. *inter-umbral region*: region included between 100 and 80% of the maximum dose intensity (yellow area in Figure 3.12);

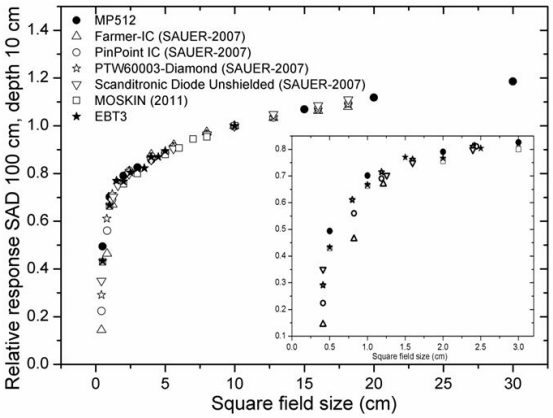

Figure 3.11: Comparison of output factors from different detector type and size, from Sauer et al. [53]. The inset window shows a detail for field sizes smaller than 3x3 cm^2.

3. *out-of-field region*: region included between 20 and 0% of the maximum dose intensity (pink areas in Figure 3.12).

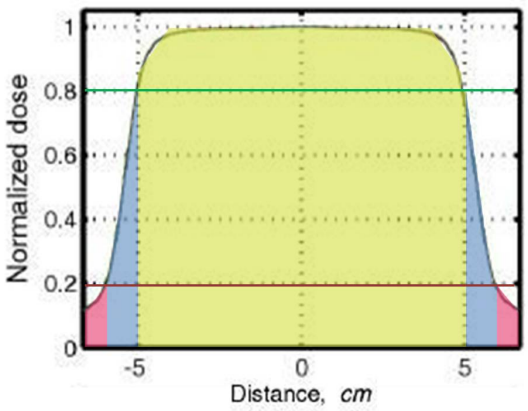

Figure 3.12: Division of the beam profile in penumbral regions (blue), interumbral region (yellow) and out-of-field region (pink). The horizontal lines indicate 80% (green) and 20% (red) doses. [19]

Among these three, the one that characterises a photon beam is the penumbral region: in fact, its slope and absolute width are fundamental parameters in order to quantify the effectiveness of the stereotactic treatment. Therefore, penumbræ measurements are performed with the MP512 placed at 10 cm depth in solid water phantom at isocentre (the same configuration used for the output factor measurements).

The square field size is collimated ranging from 0.5x0.5 cm^2 up to 10x10 cm^2 only using the linac jaws and keeping the multi-leaf collimator completely retracted. This choice allows to avoid the problems of inter-leaf and round leaf-end leakages typical for multi-leaf collimators.

The beam profile is evaluated using the central row of the MP512. In order to align the central pixel (row 11, column 12) with respect to the

beam, the detector is irradiated by a 0.5x0.5 cm^2 beam and moved laterally relatively to the beam by steps of 1 mm in both directions. The central position is identified when the corresponding detector pixel has the maximum response. All MP512 profiles are then normalised to the response of the central axis pixel.

The measured data points for the profiles are calculated as the mean value of five repetitions and the error bars of each data point are calculated as two standard deviations.

The measurements of the beam profile are shown in Figure 3.13. In particular, the plot compares the data measured by a set of EBT3 films with the ones performed by MP512.

For field sizes smaller than 5x5 cm^2 (Figure 3.13a to Figure 3.13d), the two sets of data are aligned to the value at 50% of the beam central axis. On the other hand, profiles for 5x5 and 10x10 cm^2 (Figure 3.13e and Figure 3.13f) are aligned to the response of the central axis as the 50% value is not available due to the overall MP512 size. At the same time, profiles measured with EBT3 films are normalised to the average value of a 2x2 mm^2 area around central axis of the beam profile.

In order to have a more accurate evaluation of the agreement between the two detectors, datasets were analysed by the means of MATLAB (Mathworks. Inc) generating a fit using the Curve Fitting Toolbox. The FWHM and the penumbræ (80%÷20%) are evaluated by interpolating the data points using the interpolation-shape-preserving fit (with a resolution step of 0.01 mm) and summarised in Table 3.1.

In the evaluation of the FWHM of the field size, MP512 and EBT3 films show a good agreement to within 1.36%. On the other hand, MP512 gives penumbral widths that are nominally about 0.4 mm wider than the ones derived from of the EBT3 film measurements. Additionally, the relative discrepancy increases with the decrease of the field size, suggesting an effect of averaging due to the size of the detector sensitive area (0.5x0.5 mm^2). An extra contribution is due to the detector pitch size (2 mm) which becomes too large when compared to the steep gradients of the penumbra width, especially for very small field size beams. A detailed analysis of this effect is presented in Wong et al. [46].

In any case, the absolute value of the discrepancy is less than 0.4 mm for the smallest field (0.5x0.5 cm^2): this overestimation is still acceptable for clinical use, considering that the general criterion for small field therapy applications is approximately 1 mm.

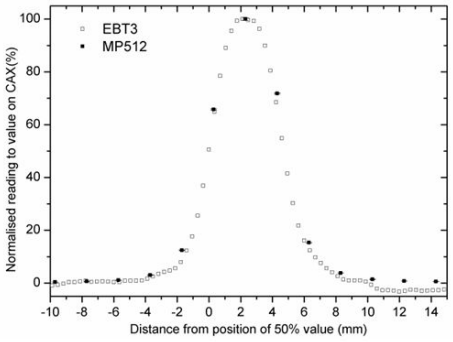

(a) field size 0.5x0.5 cm^2.

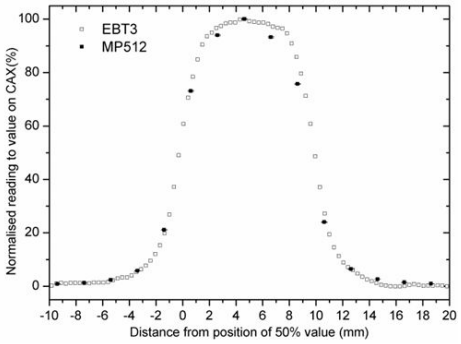

(b) field size 1x1 cm^2.

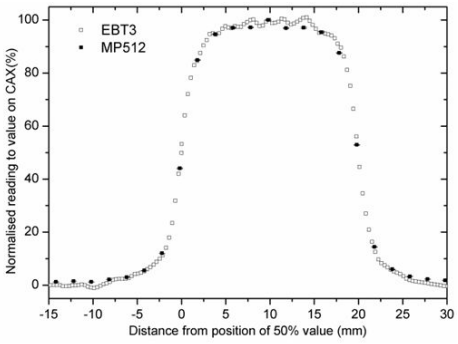

(c) field size 2x2 cm^2.

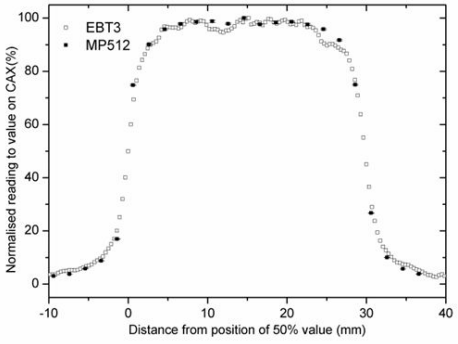

(d) field size 3x3 cm^2.

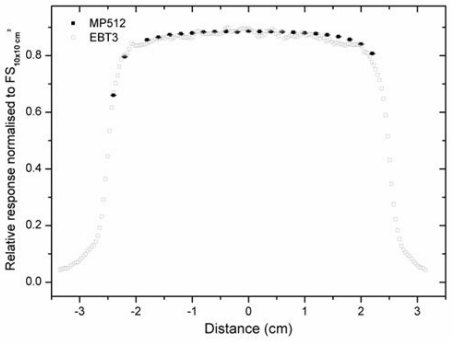

(e) field size 5x5 cm^2.

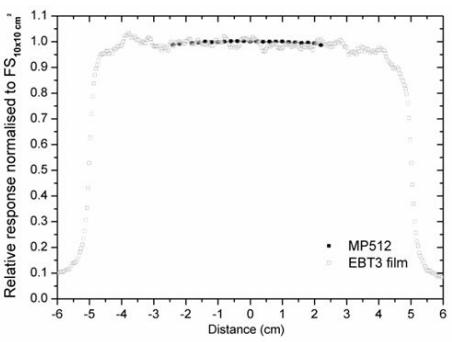

(f) field size 10x10 cm^2.

Figure 3.13: Beam profiles measured with MP512 and with EBT3 films for radiation fields ranging from 0.5x0.5 to 10x10 cm^2.

Table 3.1: EBT3 film and MP512 FWHM and penumbra width (80%-20%) study for different square field sizes at 10 cm depth and isocentre.

field size (mm)	EBT3		MP512		$\frac{MP512-EBT3}{EBT3} \times 100$	
	FWHM (mm)	Penumbra (mm)	FWHM (mm)	Penumbra (mm)	Δ FWHM (%)	Δ Penumbra (%)
100	100.46	3.60	-	-	-	-
50	49.98	3.31	-	-	-	-
40	39.96	3.16	40.16	3.61	+0.5	+14.2
30	29.88	3.02	29.89	3.49	+0.03	+15.5
20	19.91	2.74	20.08	3.17	+0.85	+15.6
10	9.96	2.46	10.08	2.89	+1.2	+17.4
5	5.15	1.97	5.22	2.36	+1.36	+19.7

Chapter 4

Dynamic characterisation of MP512

After having characterised MP512 in terms of static performances for small field dosimetry in chapter 3, the goal of chapter 4 is to characterise the temporal resolution performances of MP512 for Adaptive motion Radiation Therapy (ART) combined with a dynamic multi-leaf collimator tracking technique for motion compensation.

This motion tracking setup (described at paragraph 4.1) consists in a movable platform (HexaMotion technology, paragraph 4.1.1) and a radiofrequency tracking system (Calypso 4D localisation system, paragraph 4.1.2). As these radiofrequencies induce extra currents in the fast readout system of MP512 that lead to large fluctuations of the signal baseline, a radiofrequency interference shielding is necessary. Paragraph 4.1.3 describes a feasability study for the shielding system run by the means of Geant4.

After this description of all the extra devices necessary for the experimental setup, two different experiments are presented. The first one (paragraph 4.2) consists in the measurement of the beam profiles in the three different configurations and their benchmark with EBT3 films. The idea behind this experiment is exactly the same as the one in the previous chapter, but this time the lung movement pattern is used and tracked.

The last part of the chapter (paragraph 4.3) investigates the tracking performances of Calypso technology thanks to the real-time capability of MP512. The main idea is to superimpose a dynamic MLC wedge along the Y axis to the lung motion pattern and characterise the closeness of motion and tracking integral dose profiles with respect to the no-motion one. In fact, the first aim is the verification that the tracking profile is closer to the no-motion trace than the motion one (but not coincident): as this relys on integral dose, it can be benchmarked with the use of EBT3 films. Hence, a further timing analysis has been run in order to localise which conditions make the tracking system fail: consisting in a pulse-per-pulse dose study, EBT3 films can not be used to confirm the obtained results. Finally, an introductionary idea of possible solution in order to correct the tracking failures is presented.

All these experiments have been run at the Royal North Shore Hospital

(RNSH) in Sydney: in fact, this centre features the HexaMotion and Calypso systems. At the same time, the photon beams have been generated by a Varian 2100EX medical linear accelerator.

4.1 Movement and motion tracking

In order to mimic the movement described at paragraph 2.7, MP512 is used in combination with the tracking system Calypso and the movable platform HexaMotion. In particular, these devices are used in three different operation modalities:

1. static conditions ("*no-motion*" mode);
2. with the HexaMotion platform mimicking the temporal movement pattern of a lung tumor ("*motion*" mode);
3. with the HexaMotion platform mimicking the temporal movement pattern of a lung tumor and the Calypso system tracking the same moving target while the linac dynamic multi-leaf collimators (DMLCs) compensate for the instantaneous displacement ("*tracking*" mode).

The aim of these different modalities is to reconstruct the 2D dose distributions of small field square beams and to compare them to investigate the effectiveness of the Calypso tracking system.

4.1.1 HexaMotion moving platform

HexaMotion technology (Figure 4.1) consists in a moving platform manufactured by ScandiDos as accessory for Delta4 (HexaMotion, 2014), which is able to mimic the temporal movement pattern of a lung tumor.

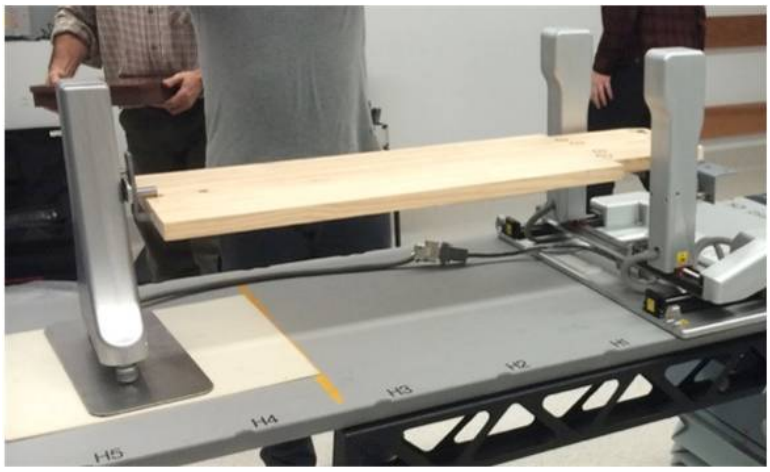

Figure 4.1: Hexamotion moving platform.

The system has been designed to allow the movement of the platform over six directions (three translations and three rotations), but in this work

it has been performed the motion along the X and Y axis as described in paragraph 2.7 and shown in Figure 4.2.

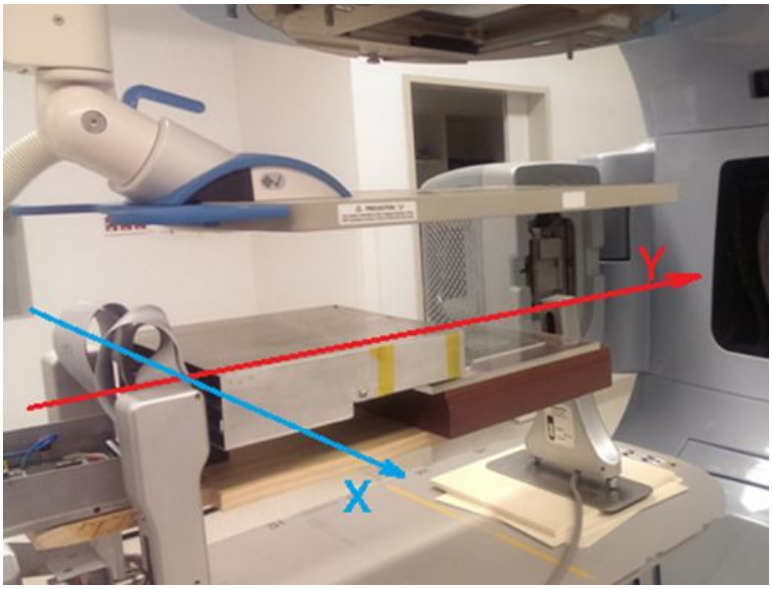

Figure 4.2: The detector, placed onto the platform HexaMotion, is shown along with the orientation of the coordinate frame.

Furthermore, in our specific case, the platform has been modified by using a flat wood slab where the detector and its DAQ have been placed: this allows to arrange a layer of solid water for backscattering underneath the detector, as shown in Figure 4.3.

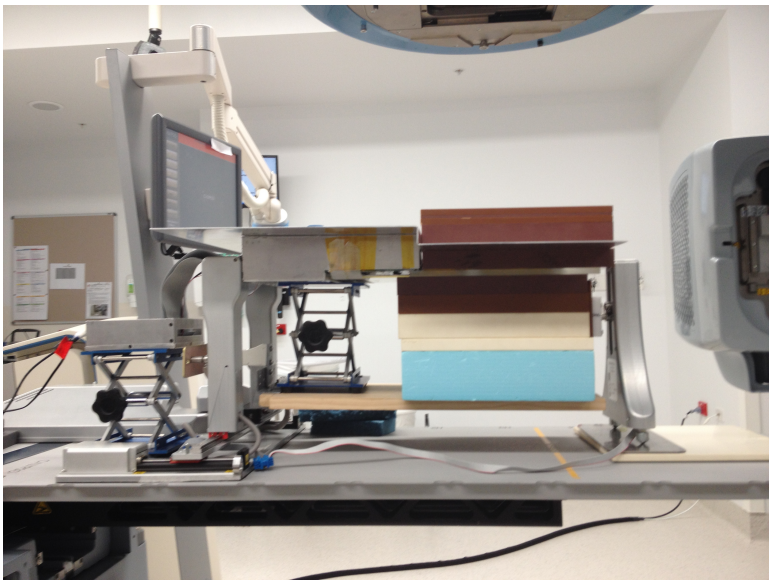

Figure 4.3: The detector is placed on a layer of solid water above a wood slab.

4.1.2 Calypso tracking system

In order to track the movement of the Hexamotion platform, the Calypso 4D Localisation System described at paragraph 1.4.3 has been used. The transponder beacons have been fastened directly to the detector with some adhesive tape as shown in Figure 4.4.

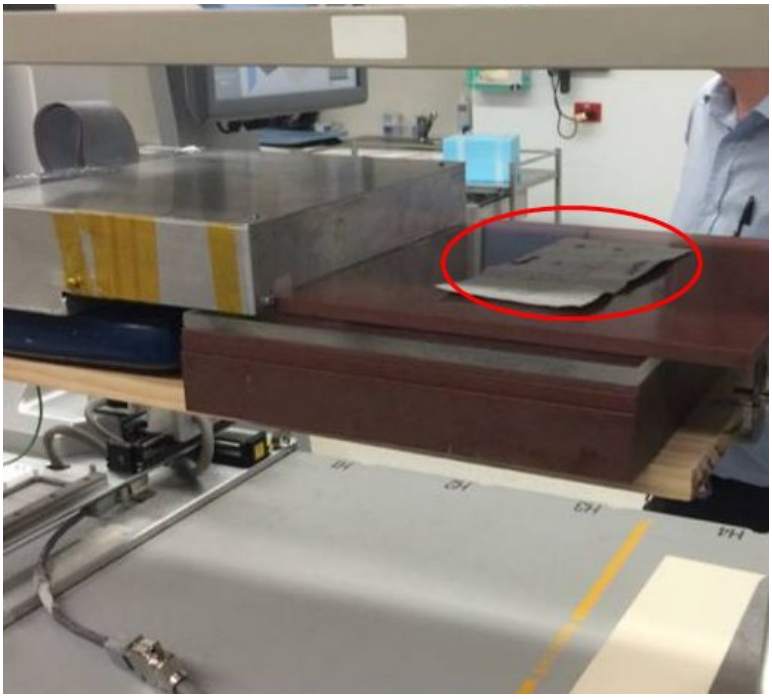

Figure 4.4: The beacons are placed on a white paper as shown in Figure 1.3 and placed over the detector.

4.1.3 Detector shielding

The use of Calypso joined with the fast readout system of MP512 requires some extra precautions: in fact, radiofrequencies and time-varying electromagnetic fields induce a current in the detector wiring and in the front end electronics, leading to large fluctuations of the signal baseline. In order to avoid this problem, an ad hoc radiofrequency interference shielding has been designed through the medium of Geant4. It consists of a packaging structure composed by a sequence of three different layers placed above the detector:

- 2 mm of aluminium, extending also above the electronics in order to shield the preamplifier boards;
- 5 mm of solid water;
- 5 mm of PMMA.

The thickness of the aluminium has been calculated in order to have no more than 5% of the original power of the RF field to be transmitted

through it: special care has been taken into account as conducting materials like aluminium produce the "skin effect".

Table 4.1: Main electromagnetic parameters for the aluminum RF shield.

parameter	description	typical value	units
ϵ_0	permittivity in free space	8.854×10^{-12}	F/m
μ_0	permeability in free space	$4\pi \times 10^{-7}$	H/m
μ_r	relative permeability	1	aluminum [54]
ω	oscillation	$2\pi \times 500 \times 10^3$	Hz
σ	conductivity	3.54×10^4	$(\Omega\cdot\text{cm})^{-1}$

In the approximation of a plane wave (ϕ), incident perpendicularly on the aluminum plane, Maxwell equations solutions have the form

$$\frac{\partial^2\phi}{\partial z^2} = i\mu_0\mu_r\epsilon_0\epsilon_r\omega\frac{\partial\phi}{\partial t} + \mu_0\mu_r\sigma\frac{\partial\phi}{\partial t} \tag{4.1}$$

where i is the imaginary number. Using the approximation of a conductive material ($\omega\epsilon_0\epsilon_r \ll \sigma$), the equation simplifies to

$$\frac{\partial^2\phi}{\partial z^2} = \mu_0\mu_r\sigma\frac{\partial\phi}{\partial t} \tag{4.2}$$

which is the equation of a second order partial mixed derivative equation whose solution has the form

$$\phi = \phi_0 \cdot e^{-\alpha z} \cdot e^{i(\omega t - \beta z)} \tag{4.3}$$

where z represents the thickness of the aluminium shield and

$$\alpha = \beta = \sqrt{\frac{\mu_0\mu_r\sigma\omega}{2}} \tag{4.4}$$

At a frequency $f = 500\ kHz$, the corresponding skin depth for the electromagnetic wave propagated by Calypso is

$$\delta = \frac{1}{\alpha} = \sqrt{\frac{2}{\mu_0\mu_r\sigma\omega}} \simeq 700\ \mu m \tag{4.5}$$

approximately.

In order to have a maximum 5% of the original power, the mathematical constraint to verify is

$$\phi_0 \cdot exp\left\{-\frac{z}{7\times10^{-4}}\right\} = 0.05 \cdot \phi_0 \tag{4.6}$$

which leads to the solution

$$\bar{z} \simeq 2\ mm. \tag{4.7}$$

The other layers (solid water, PMMA and aluminium) form an equivalent water depth of 1.5 cm, which corresponds to d_{max} for a 6 MV photon beam. Similar approach is used in a single diode packaging for entrance dosimetry using metal envelope (brass or tungsten) and plastic to reproduce thickness equivalent to dmax for required MV photon energy [55].

In order to determine the impact of the shielding on the ability to reconstruct the dose, some Monte Carlo simulations have been performed using Geant4 version 10.0p01 [56] as well as some experimental verifications. The simulations were run considering a 30x30x30 cm^3 water block phantom and different field size 6 MV X-ray beams:

1. 1x1 cm^2;
2. 2x2 cm^2;
3. 3x3 cm^2.

In fact, the reference configuration for these simulations is when the entire phantom is water, whereas the simulation of interest includes the replacement of the first 2 mm of water with aluminium, which corresponds to replicate placing 2 mm of aluminium shield on top of PMMA detector enclosure. The source to surface distance (SSD) is 100 cm, and the beams are fired from space files created from an EGSnrc Monte Carlo based system that models a Varian 2100C linac. The model used to represent the linac and the phantom setup, along with the physics of transport, has been already validated by experimental results [57].

Many physics models are used from the standard physics packages: photoelectric effect, Compton scattering and gamma conversion (for photons); ionisation, bremsstrahlung and positron annihilation (for leptons). The particle range cut is set to 0.1 mm as well as the electron/positron maximum step length. Dose is scored inside the phantom at a voxel resolution of 1 mm^3. Each simulation is divided in ten parallel jobs: each has its unique seeds, and the mean dose is reported. At the same time, the standard deviation is taken across 10 simulations to evaluate uncertainties.

Globally, $4x10^{13}$ primary histories are simulated for each field size, where a primary history corresponds to an electron hitting the X-ray target in the linac head. The dose uncertainty is approximately $\pm 1\%$ of the dose at 1.5 cm depth at the beam central axis (CAX) for each field size.

In order to measure the effectiveness of the aluminium shield, the baseline of the detector (the dark signal) is acquired in three different configurations:

1. with Calypso off;
2. with Calypso on and no shield;
3. with Calypso on and the aluminium shielding placed over the phantom as described above.

The acquisition of the base line has been performed for 120 seconds at the sampling rate of 360 Hz: this choice allows to cope with the large number of

samples the simulations require. The statistical analysis of the dark signal consists in the calculation of the average of the baseline and its standard deviation in each channel of MP512 in the three different conditions; the frequency distribution of the standard deviation of the baseline is plot.

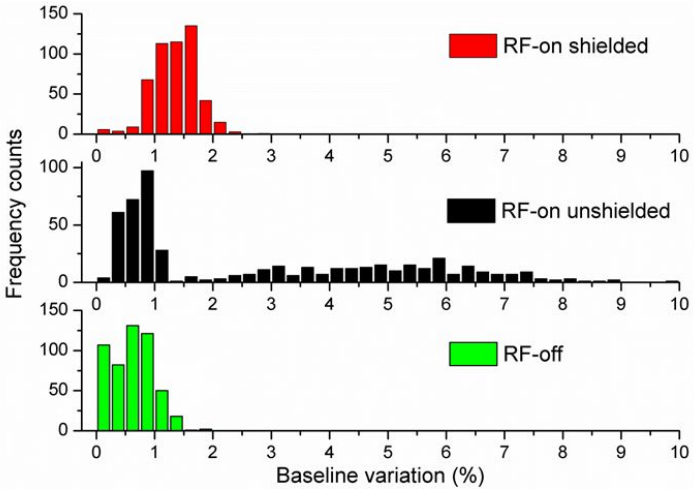

Figure 4.5: Spectrum of the dark noise acquired with Calypso ON, with and without shielding (red and black bars, respectively) compared to baseline fluctuation when Calypso is turned OFF (green bars).

Figure 4.5 shows that without Calypso nor aluminium shielding (case 1, green diagram) the baseline has an average fluctuation of 0.5% of the full signal scale.

On the other hand, with the RF interference generated by the starting of Calypso (case 2, black diagram) the detector suffers a baseline fluctuation up to 6%. Although this large fluctuation has a relative small frequency count (the maximum is 25 occurrences), it degrades the accuracy of the measurement substantially by the generation of a stochastic current signal which can not be distinguished from the signal generated by the beam itself.

Finally, the red diagram shows the effect of the aluminium shielding (case 3): this expedient removes completely the large fluctiation component of the baseline with an increment of the average fluctuation from 0.5% to 1.5%, which is admissible.

Figure 4.6 and Figure 4.7 display the results of the Monte Carlo study. The first picture shows the depth-dose profile for each field size: the dosimetric impact of the aluminium slab is minimal. An unimportant (within 1% of the simulation uncertainty) dose drop is seen along the CAX depth-dose profile beyond around 14 mm depth: in fact, in the first 14 mm depth, there is a clear increase in the energy deposition in water as the aluminium (whose density is about 2.7 g/cm^3) introduces larger secondary electron fluence than the same thickness of water equivalent material. This extra amount of electrons is stopped by around 14 mm depth: at this point, dose is related primarily to the photon fluence, which does not have substantial changes between the two scenarios (2 mm of water or 2 mm of aluminium).

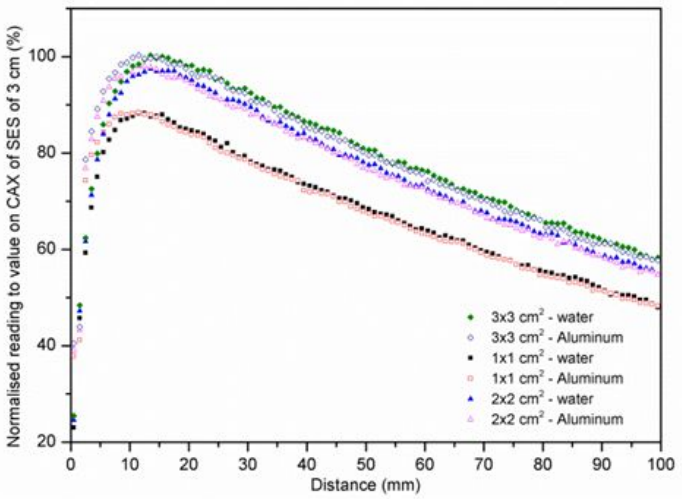

Figure 4.6: Comparison of the Geant4 simulations of Percentage Depth Dose (PDD) with and without the aluminum shield for the RF noise generated.

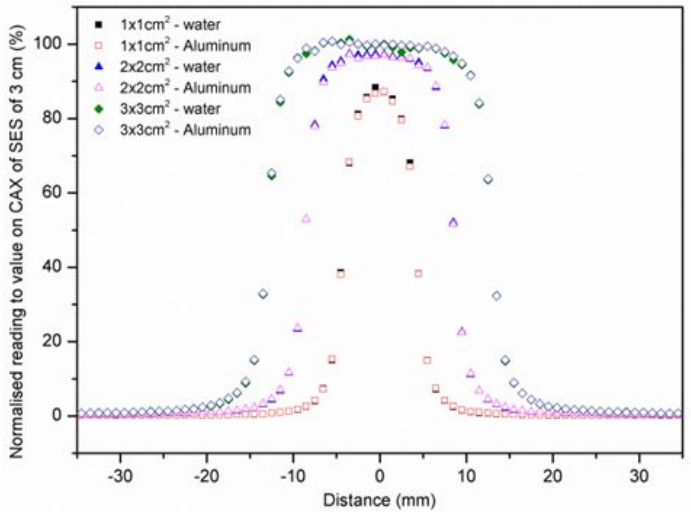

Figure 4.7: Dose profiles for 1x1, 2x2 and 3x3 cm2 field sizes with and without the aluminum shield for the RF noise generated.

In the second picture, cross-profiles at 1.5 cm are presented: in this case, there appears to be no significant changes.

4.2 Beam profile measurement

The first part of the characterisation of the tracking system consists in the measurement of beam profiles of 1x1, 2x2 and 3x3 cm^2 in the three no-motion, motion and tracking modalities:

1. in no-motion mode, the detector is aligned by the laser with the central pixel in correspondence with the isocentre. The detector is then placed on the wooden platform above 6 cm of solid water with the beacons placed onto the aluminium shield and Calypso activated with no tracking motion while HexaMotion is off;

2. in motion mode, the detector is in the same position and alignment as for the previous case. This time, Calypso is still activated with no tracking mode but the HexaMotion platform moves accordingly to the lung temporal pattern shown in Figure 2.17 after being activated manually. However, the difference due to the asynchronicity in the start of the beam and the movement is completely negligible thanks to the length of the exposure;

3. in tracking mode, MP512 is on the platform and moves along thanks to the HexaMotion system. Meanwhile, Calypso tracks the position of the beacons and forwards this information to the tracking system which generates the algorithm that drived the dynamic MLCs. According to Keall [11], the delay introduced by this tracking process is approximately 250 ms.

In order to collimate the beam, the jaws are retracted 1 cm apart and only the MLCs are used. This choice has many reasons:

- minimise the end-of-leaf leakages;
- allow the full range of the movement (which in this work is approximately 8 mm and 2 mm in Y and X directions, respectively - view Figure 2.17);
- verify the tracking technique which relies on the movement of the dynamic MLCs.

Profiles are measured by MP512 by irradiating the detector with 1000 MU at 600 MU/min. In order to benchmark these data, EBT3 films are irradiated in the same experimental session under the same conditions.

The equalisation of MP512, normalisation of the profiles and their alignment with the EBT3 film profiles are exactly the same adopted in the static beam profile measurement described at paragraphs 3.2 and 3.7. After equalisation, a variation of the response across the whole detector of 0.5% is obtained; MP512 profiles are normalised to the response of the central axis

pixel (row 11, column 12) and aligned with the corresponding film profile to the value of 50% of the central axis value; EBT3 profiles are normalised to the average value of a 2x2 mm^2 area surrounding the central axis of the beam profile.

The measurements for both the detectors are calculated as the mean value of 5 repetitions and the error bars of each data point are calculated as two standard deviations.

Quantitative analysis of the agreement between the profiles obtained by the two detectors are performed by the means of MATLAB (Mathworks. Inc) generating a fit by the Curve Fitting Toolbox. The FWHM and right hand side (RHS) penumbra are evaluated by interpolating the data using the interpolation-shape-preserving fit and are reported in Table 4.2.

The choice of the right hand side is not random: in fact, this side is more representative to show the large distortion generated by the organ motion pattern adopted in this thesis.

Figure 4.8 shows measurements of the beam profile along the Y direction. These data confirm the impact of the tracking system resulting in a mitigation of the dose smearing generated by the organ motion. The effectiveness of this technique can be quantitatively evaluated considering the variation of the penumbra: between no-motion and motion, there is a 2.4 average increase; when the tracking system is activated, the variation is reduced down to 0.7 mm, leading to an effective reduction of 70%. MP512 agrees with the film measurements within 3% for FWHM and 0.4 mm for penumbra width.

Profiles measured by MP512 along the X direction are also presented in comparison with EBT3 film at Figure 4.9.

The specific lung motion pattern used in this thesis features a lateral movement along X axis of approximately ± 1 mm. This distance is not long enough to trigger the displacement of a leaf when the tracking system is activated as the minimum leaf width is 2 mm. This limitation leads to the leakage that causes to the bumps in every penumbra and makes the tracking system not effective along the X direction. For this reason, the shapes of the tracking modality for all the three field sizes are more similar to the shapes obtained in the motion case rather than the ones obtained in the no-motion mode. This leads to the fact that the pattern of the beam profiles below 30% of maximum dose is related to radiation leakage between tips of closed leaves and which are absent in the profiles measured in Y direction (Figure 4.8).

4.3 Timing performances of MP512

Among all the possible strategies for lung motion management, *adaptive motion radiation therapy* (ART) features a continuous monitoring feedback of tumor movements in order to modify the beam and adapt it to the movement in real time. Calypso radiofrequency technology is an example of this strategy: the beacons follow the position of the tumor and drive the

Table 4.2: Summary of the comparison of FWHM and right hand side (RHS) penumbra of the Y direction square fields measured by MP512 and EBT3 film.

modality	square field size [cm]	EBT3 film		MP512	
		FWHM [cm]	RHS Penumbra [cm]	FWHM [cm]	RHS Penumbra [cm]
No Motion	1	1.14	0.26	1.17	0.25
	2	2.04	0.27	2.10	0.30
	3	3.06	0.30	3.16	0.29
Motion	1	1.16	0.50	1.21	0.51
	2	2.07	0.54	2.15	0.56
	3	3.10	0.53	3.15	0.57
Tracking	1	1.10	0.35	1.14	0.37
	2	2.10	0.34	2.10	0.38
	3	3.10	0.35	3.12	0.39

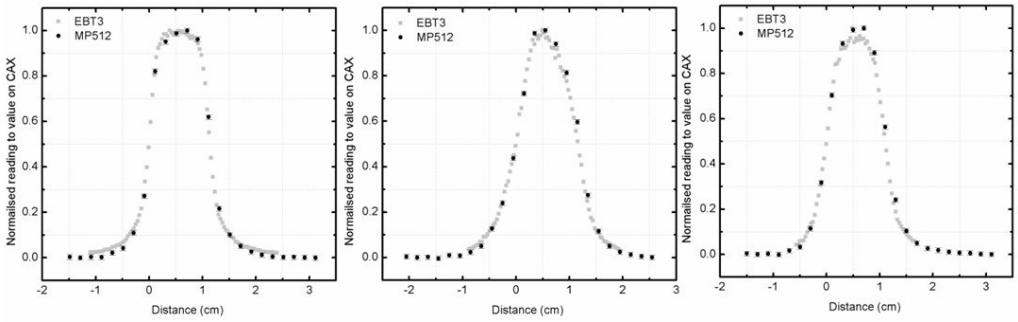

(a) field size 1x1 cm^2 in no motion, motion and tracking mode.

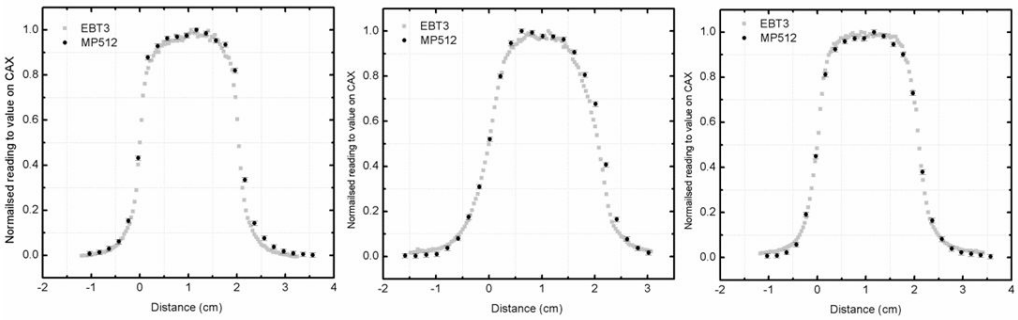

(b) field size 2x2 cm^2 in no motion, motion and tracking mode.

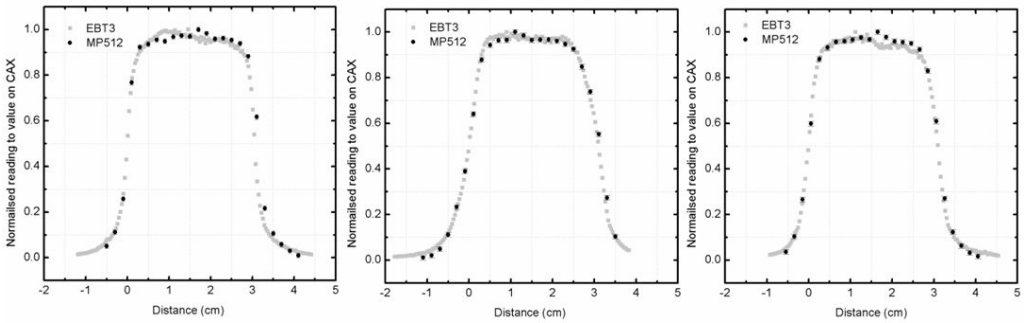

(c) field size 3x3 cm^2 in no motion, motion and tracking mode.

Figure 4.8: Y direction dose profiles measured by EBT3 film and MP512 in no-motion, motion and tracking modes.

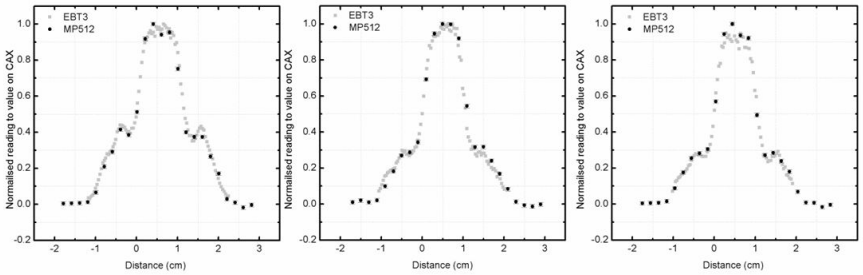

(a) field size 1x1 cm^2 in no motion, motion and tracking mode.

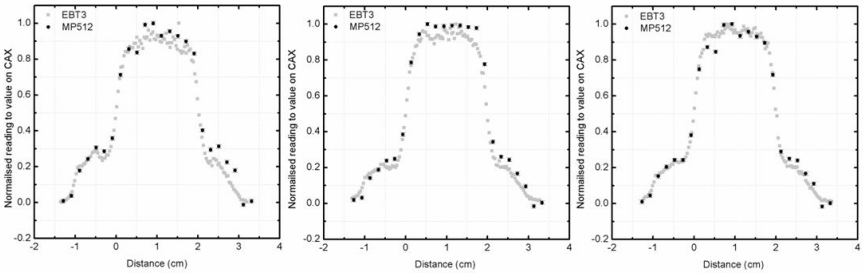

(b) field size 2x2 cm^2 in no motion, motion and tracking mode.

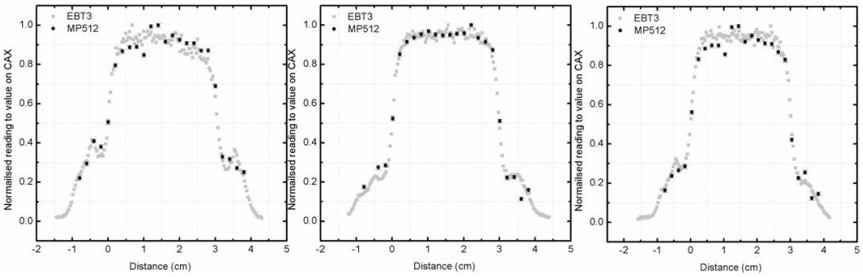

(c) field size 3x3 cm^2 in no motion, motion and tracking mode.

Figure 4.9: X direction dose profiles measured by EBT3 film and MP512 in no-motion, motion and tracking modes.

dynamic MLCs through the definition of a tracking algorithm.

A potential application of MP512 for QA of movable target radiotherapy modalities is the measurement of the dose on a pulse-by-pulse base. The high temporal resolution can be used to test and refine the performance of the tracking feedback algorithm for a specific patient organ motion pattern.

4.3.1 Dynamic wedge measurement

In order to investigate 3D (X,Y and t) dose reconstruction capability of MP512, a dynamic wedge beam combined with the lung motion pattern described at Figure 2.17 is delivered to a solid water phantom placed onto HexaMotion platform using the three modalities described above. MP512 is placed at 1.5 cm depth and the central pixel (row 11, column 12) is aligned with the isocentre.

The dynamic wedge is formed by delivering a total dose of 1000 MU at a dose rate of 600 MU/min and beam energy of 6 MV using the MLCs (leading to a 3x3 cm^2 beam at the end of the wedge) without any rotation of the gantry. The fact that the gantry is fixed vertically above the detector allows to neglect the effects of the angular dependence of the detector (which will be investigated and reported in the future by CMRP research group).

The integral dose deposition measured by MP512 is benchmarked by the response measured by EBT3 films exposed to the same beam and motion conditions in the same experimental session. The instantaneous pulse-by-pulse and integral dose map measured by MP512 has been analysed in real time and retrospectively. The instantaneous dose measured by MP512 is analysed as a function of time in order to evaluate the shape of the signal detected by the central pixel at 50% of maximum dose delivered in no-motion, motion and tracking modalities.

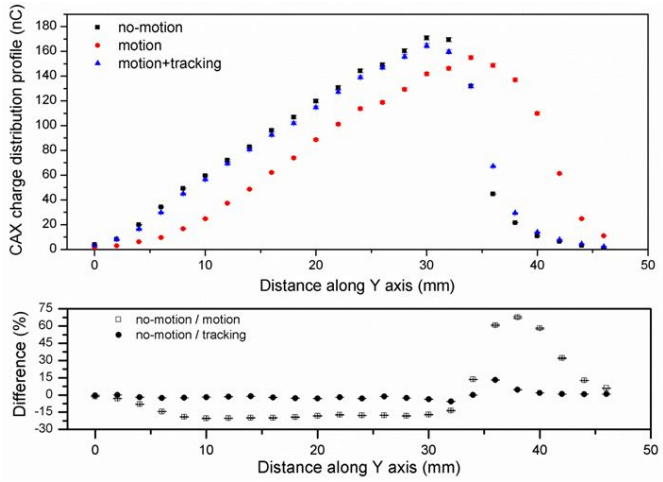

Figure 4.10: Dynamic wedge integral dose profile along the Y axis (column 13) and percent difference. The latter is normalized to the no-motion peak integral dose response.

Figure 4.10 shows the accumulated charge profiles of the no-motion,

motion and tracking of the dynamic wedge as well as the percentual difference between no-motion and motion and between no-motion and tracking along column 13. The difference between no-motion and tracking modalities integral charge can reach a maximum difference of about +15% in the region corresponding to the right hand side penumbra of the wedge, while along the wedge the discrepancy is always within -3%. On the other hand, the comparison between no-motion and motion shows an average difference of -18% along the wedge and a peak of +75% in the penumbra region at a higher distance along Y axis with respect to the maximum difference between no-motion and tracking modes.

In order to verify these data, the same acquisitions are run with several EBT3 in the same experimental conditions used for MP512. In particular, in order to get an overall response of the films, an average over 30 X-columns at the center of the irradiated portion is performed (in the zone that corresponds to column 13 of MP512).

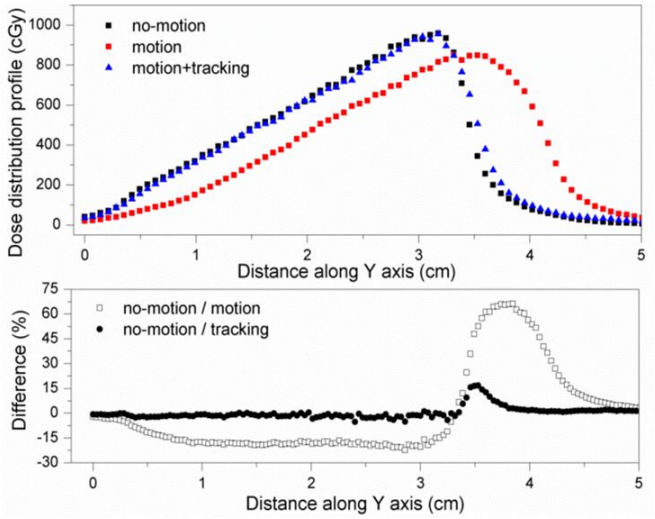

Figure 4.11: Dynamic wedge calibrated integral profiles (cGy) measured by EBT3 film and percentage difference normalised to no-motion peak integral.

The results are plotted in Figure 4.11. The upper panel of the plot shows the value in absolute dose (cGy) after calibration, while the lower panel displays the difference in percentage of the motion and tracking in comparison with the no-motion. The latter plot shows a very good agreement with the results obtained by MP512, with +70% of discrepancy for the penumbra region and -18% for the wedge region in the motion with no tracking modality. The direct comparison of the wedge profiles measured with MP512 and EBT3 films is displayed in Figure 4.12 and confirms the results underlined before.

An important fact to underline is that the normalising all the profiles to the no-motion peak gives a lower response (about 80%) only for the motion profile and not for the tracking one (around 100%).

Globally, all this information underlines the mitigation of the error obtained thanks to the tracking system. Nevertheless, there is still a remark-

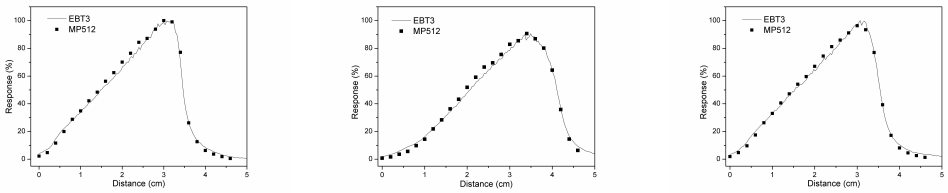

(a) no-motion. **(b)** motion. **(c)** tracking.

Figure 4.12: Comparison of response to the dynamic wedge delivered in three modalities measured by EBT3 film and MP512 and normalised to no-motion peak integral.

able difference, meaning that at some time the tracking system is not able to reconstruct the moving profile. For this reason, a detailed timing analysis of the dynamic wedge has been carried out and is described in the following section.

4.3.2 Timing analysis

This additional study consists in the analysis of the response of a single pixel as a function of time and, thanks to MP512 high temporal resolution, aims to localise the exact time the tracking system fails and is not able to reconstruct accurately the wedge profile. An important concept to point out is that this analysis has no EBT3 film benchmark as they can not allow a pulse-by-pulse analysis as they provide only the integral response.

The attention is then focused on the pixel at 50% of maximum charge distribution in the three modalities. As a result of the superposition of the lung motion pattern and the wedge, this pixel changes from one modality to the other: in particular, for motion and tracking modes, it corresponds to pixel (row 11, column 13) while for motion modality it is pixel (row 8, column 13). This fact is an extra confirmation that the overall effect of the tracking system is effective and that the failure is circumscribed to a small temporal window.

Figure 4.13 illustrates the shape of the transients for the pixels above mentioned:

- the no-motion trace (black curve) is shaped by the transient generated exclusively by the dynamic wedge;
- the motion trace (red curve) features a strong deviation from the original instantaneous response transient. In fact, the response consists in large spikes associated to the maximum displacement of the pixel, and the global trend of the curve does not follow the black one;
- the tracking trace (green curve) mitigates the displacement of the pixel reducing the amount of time it is exposed to a different part of the beam. In fact, the global trend of the curve matches the black

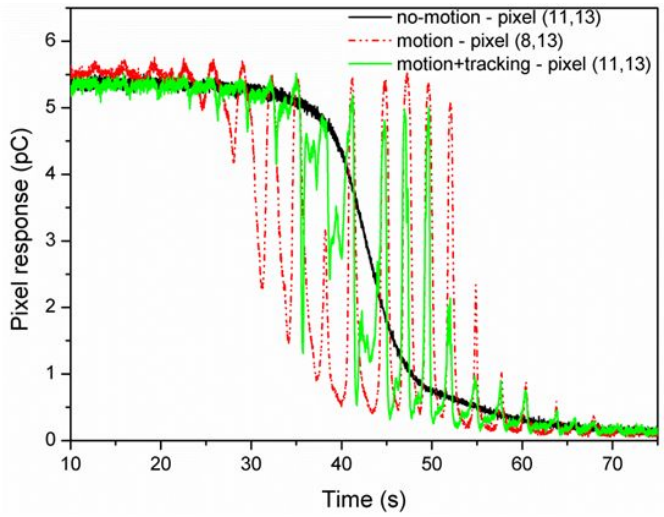

Figure 4.13: Charge deposition transient recorded by one pixel located at 50% of the maximum charge deposited for three motion modalities.

transient. However, the tracking system does not correct for those components of the movement associated with very fast varying displacements.

In fact, these fast components generate the misplacement between the expected position in no-motion and tracking cases, leading to the difference measured in the squared field measurements and the integral dose profiles of the dynamic wedge described in the previous sections.

This effect is generated by the latency associated with the tracking algorithm which is based on a passive feedback with a measurable delay (approximately 250 ms according to [11]) between the acquisition of the beacons position and the movement of the MLC. This is due to the fact that Calypso works as a pure proportional controller (view appendix D): it "simply" calculates the difference between the reference value (the measured position of the beacons) and the controlled variable (the MLCs position) and tries to make them coincide via a fixed proportional term called gain.

On the other hand, a predictive algorithm could be used to improve the performance of the tracking system, as suggested by Srivastava et al. [58]. This would consist in making the tracking system a PD controller (appendix D): the derivative term could predict the next positions of the beacons and make this technique "more adaptive" to every particular lung motion pattern. In particular, this would allow to tune the tracking algorithm in order to follow as much as possible the fast varying displacements and minimise the oscillations generated by the fast transient components of the patient specific motion pattern adopted for the plan.

4.3.3 Fast Fourier transform quantitative analysis

MP512 has sufficient temporal and spatial resolution capabilities to be used to refine the parameters of this predictive algorithm. A preliminary study

of the transients in terms of frequency components is presented hereafter. Its aim is to give a quantitative approach to the problem of minimising the residual inaccuracy of the tracking system.

As for the preceeding timing analysis, this study is focused on the pixel at 50% of maximum charge distribution in the three modalities. Again, because of the lung motion pattern superimposed to the wedge, this pixel changes from one modality to the other: for motion and tracking modes, it is found to be pixel (row 11, column 13) while for motion modality it corresponds to pixel (row 8, column 13). The aim of the choice of 50% of dose is just to show an average behaviour in the context of this preliminary study. For example, in terms of clinical studies, it could be interesting to analyse one or both the edges of the beam penumbra: depending on the specific application of the beam, the oncologists would get complementary information.

In order to carry on a frequency component study, the three transient profiles corresponding to the pixels mentioned just above (Figure 4.13) have undergone a discrete Fourier transform. This procedure has been realised by the means of OriginPro 8.5.0 (OriginLab Corporation, Northampton, MA) and its Fast Fourier transform function. The result of this operation is the decomposition of every transient amplitude profile in its frequency components.

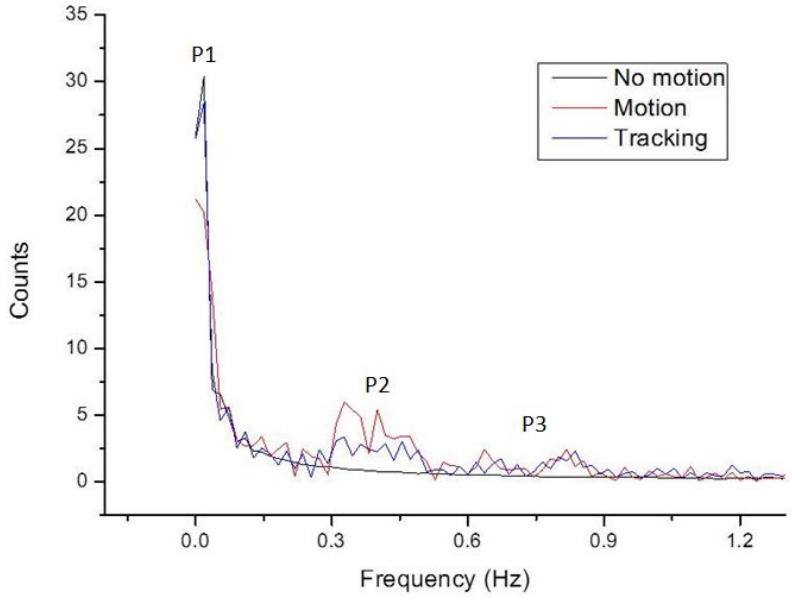

Figure 4.14: Fast Fourier Transform amplitudes of the time transients recorded by one pixel located at 50% of the maximum charge deposited for three motion modalities.

The results of this procedure for the three modalities are plotted in Figure 4.14.

1. the no-motion trace (black curve) shows a peak at very low frequency (approximately 0.02 Hz - P1 peak referring to Figure 4.14) followed

by a smooth falling edge;

2. the motion trace (red curve) features a peak at 0 Hz frequency (P1 peak) plus another peak at an average frequency (approximately 0.4 Hz - P2 peak) and two coupled peaks which can be considered as a single peak at higher frequency (approximately 0.65 and 0.8 Hz - P3 peak);

3. the tracking trace (blue curve) has a peak at very low frequency (approximately 0.02 Hz - P1 peak) followed by the same trend of the motion one (with similar counts values for the three peaks).

In fact, considering all the peaks separately, each one corresponds to a component of the transient profile:

- the left peak represents the very slow descent component;
- the central peak represents the low frequency oscillations (which are not present in the no-motion modality);
- the right peak represents the high frequency oscillations (which are not present in the no-motion modality).

In particular, the tracking plot is almost always between the two other lines: this is once again a confirmation that the Calypso is effective but only to track low and average frequency components.

In fact, in the tracking modality P2 peak is strongly reduced: this represents the fact that the low frequency oscillations can be managed by the Calypso technology. On the other hand, the right peak does not change sensibly between motion and tracking modalities: this is due to the fact that the high frequency oscillations are too fast to be followed properly by the tracking system (they are represented by the red and green coincident spikes at Figure 4.13).

The aim of the ART is to make the tracking profile as close as possible to the no-motion one. In the specific case of Calypso technology, the only way that operators have to adjust the tracking system to the specific pattern is to tune the constant which is relative to the proportional controller.

Therefore, the information about the frequency components of the specific lung motion pattern of every patient obtained by the means of a Fourier transform study can be used as a quantitative criterium: the best proportional coefficient is the one that minimises the area between the black and the blue curves in Figure 4.14.

Chapter 5

Static characterisation of DUO

After having described in detail MP512 performances in terms of static as well as dynamic characterisation, the focus is now set on DUO.

Paragraph 5.1 is an introduction in which it is shown that MP512 (as well as EBT3 films) does not feature a sufficient spatial resolution for very small field dosimetry (less than 1x1 cm^2) basing on Nyquist sampling theory. For this reason, it is possible to define a quantitative criterium in terms of minimum pitch between pixels: DUO has been designed in order to satisfy this condition and overtake MP512 and EBT3 film performances.

At a later stage, a preliminary electric characterisation of DUO is presented: it consists in the current-voltage characterisation (paragraph 5.2).

Finally, it is presented the study of PDD measurements (paragraph 5.4) and OF measurements (paragraph 5.5). Again, the data obtained are benchmarked against conventional radiation detectors such as ionisation chambers and radiochromic films.

All these experiments have been run at the Illawarra Cancer Care Centre (ICCC) at the Wollongong Hospital, using a Varian 2100EX medical linear accelerator. DUO static characterisation follows the one performed for MP512: for this reason the tests and the experimental setups are not described again in this chapter.

5.1 Sampling theory applied to photon beams

Sampling theory (view appendix C) considers physical quantities that can be described as mathematical functions of time. Actually, the principles of this theory are still valid if the quantities of interest depend on other physical quantities: in the case of this thesis, beam profiles depend on space.

In order to determine the minimum pitch between two pixels of a detector that allows to describe the beam without any loss of information, it is possible to apply the Nyquist-Shannon sampling theorem: in fact, the pitch represents the equivalent of the sampling time interval.

In order to obtain a reference "continuous" function, a beam profile from EBT3 films is interpolated using the interpolation-shape-preserving fit tool from MATLAB (Mathworks. Inc). As the scanning has been run at 72 dpi

(3.1), the pitch of the film profile is 353 μm, which might not be sufficient: for this reason, the interpolation is run with a spacing of 1 μm, giving rise to a redundant (in terms of spatial resolution) reference function.

This new profile undergoes a Fast Fourier Transform (FFT) by the means of OriginPro 8.5.0 (OriginLab Corporation): the result is the discrete Fourier transform of the profile, where frequencies are not inverse of time but inverse of space $[\frac{1}{mm}]$. In particular, in order to have a general procedure, not the entire profile undergoes the FFT, but only the left penumbra going from 3% to 97% of the normalised profile. These values have been chosen as they allow to study the whole penumbra while avoiding the plateaux at 0 and 1 (which would give a infinite peak at 0 $\frac{1}{mm}$ frequency).

Theoretically, this spectrum is infinite: this fact would not allow to apply the Nyquist-Shannon theorem. In reality, the high frequency values are due to the noise or response fluctuations featured by the EBT3 film beam profiles: hence, these components can be neglected as they do not exist in a real beam, allowing the application of the theorem.

Therefore, it is possible to identify the frequency corresponding to the peak of the diagram f_{max} and to define the band width frequency f_{bw} as the frequency interval at -3 dB. Thanks to this value, the Nyquist frequency can be computed as $f_N = 2f_{bw}$: its inverse corresponds to the minimum spacing between two different pixels of the detector that guarantees the complete re-construibility of the starting beam profile without any loss of information.

Six different field size profiles (from 0.5x0.5 cm^2 to 10x10^2) have been analysed following this procedure: the results are shown in Figure 5.1 and summarised in Table 5.1.

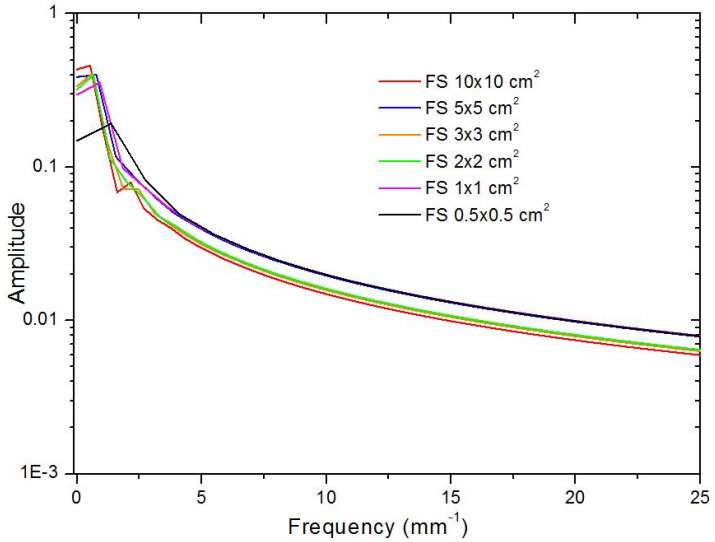

Figure 5.1: Amplitudes as functions of frequency of 6 different field sizes profiles after Fast Fourier Transformation.

This table shows that for beam profiles of 0.5x0.5 cm^2 a pitch of approximately 200 μm is necessary, while a bigger sampling spacing is sufficient

Table 5.1: Nyquist sampling pitch as a function of the field size of the photon beam.

field size (cm^2)	f_{max}	f_{bw}	f_N	Nyquist spacing [mm]
0.5×0.5	1.20	2.41	4.82	0.2075
1×1	0.81	1.62	3.24	0.3086
2×2	0.55	1.10	2.20	0.4545
3×3	0.48	0.97	1.93	0.5176
5×5	0.47	0.94	1.89	0.5297
10×10	0.48	0.98	1.96	0.5102

for bigger field sizes. For this reason, the pitch between DUO channels is of 200 μm, which is enough for field sizes of 0.5x0.5 cm^2.

At the same time, this sampling analysis determines the fact that the MagicPlate512 and EBT3 film (if the scan is run at 72 dpi) spacings are not sufficient for so small beam profiles and lead to a loss of information.

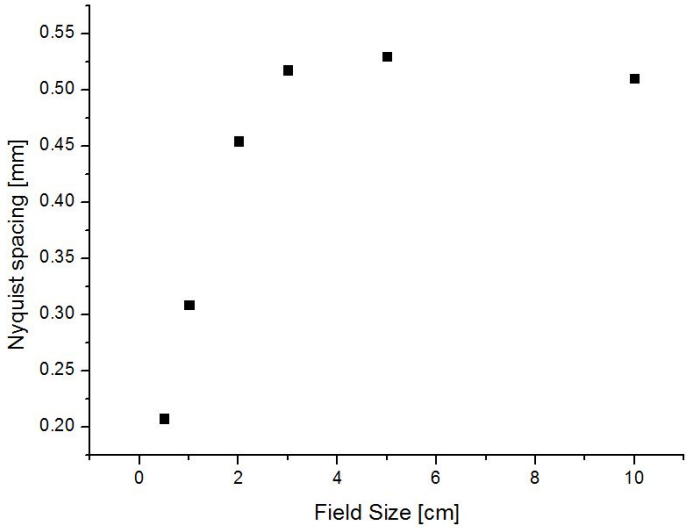

Figure 5.2: Nyquist spacing as a function of the field size.

Figure 5.2 shows extra information which can be determined by this analysis: the minimum required spacing shows an almost constant trend for field sizes bigger than 3x3 cm^2 and a decreasing profile for smaller field sizes. This fact is linked to the fact that, for photons of 6 MV, at isocentre and 10 cm depth, the mean range of secondary electrons is approximately 1.5 cm: in fact, a square of about 3x3 cm^2 (every side is 3 cm which is twice the secondary electrons mean range) guarantees the respectance of the Bragg-Gray cavity theory, while smaller field sizes do not and lead to small field dosimetry issues.

5.2 I-V

In order to have a prior characterisation of uniformity and stability of the device after its irradiation, a current-voltage analysis is performed: its aim is the determination of the baseline leakage current.

To achieve this objective, a negative bias is applied on the bulk p+ substrate across the junction defined by the n+ region. The bias was applied to the detector using a Keithley 230 programmable voltage source, coupled to a Keithley 199 System DMM/scanner and Keithley 614 electrometer to measure the reverse current across the detector.

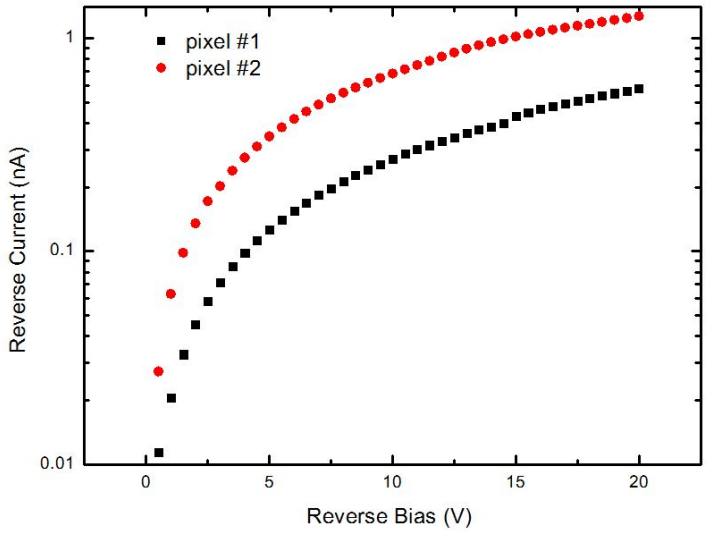

Figure 5.3: Collection of current-voltage experimental characteristics from two samples in logarithmic scale.

Figure 5.3 shows the final results obtained for two pixels of the detector (one per each axis): the trends of the measured leakage current as a function of the reverse bias are regular in both cases.

At the same time, the measured data show a range of slopes of the I-V of the pixels which varies from 270 to 680 nA at 10 V. This variation could be related to the specific position of the sample within the wafer during the manufacturing process or the surface defects induced by the mechanical stress due to the ion implantation doping technique.

5.3 Dose per pulse measurements

This test is run under conditions that are slightly different if compared with the ones for MP512 (paragraph 3.4). The dose range goes from $2.10{\cdot}10^{-5}$ to $2.78{\cdot}10^{-4}$ Gy/pulse and is achieved using a field size of 10x10 cm^2 at 6 MV with a fixed dose rate of 600 MU/min and changing the source to surface distance (SSD) of the detector from 100 cm up to 365 cm as suggested by [47] and [48] and keeping the detector at d_{max}.

The dose per pulse reference measurement is performed using the same set of data used for MP512, obtained thanks to an ionisation chamber CC13 at d_{max}. The response from DUO is normalised to the chamber response ($2.78 \cdot 10^{-4}$ Gy/pulse).

As well as for MP512, also for DUO this kind of characterization of DPP by changing the depth of the detector in a phantom can potentially be affected by the variation of the response of the detector with the spectrum of the radiation: as the sensitive volume of each pixel is much smaller than for MP512, using a 25 cm depth would lead to responses which are too low, especially for high SSDs. For this reason, this experiment has been run at d_{max}, which is approximately 1.5 cm for 6 MV photons.

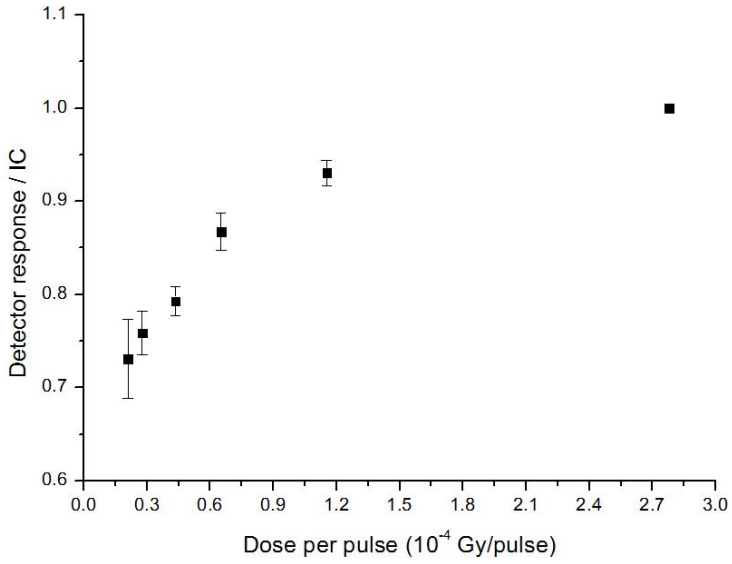

Figure 5.4: Dose per pulse response for DUO normalised to the dose per pulse of 2.78x10-4 Gy/pulse. The X axis represents the dose per pulse in order of $10^{-}4$ Gy/pulse.

Figure 5.4 shows the dose per pulse response of DUO, normalised to $2.78 \cdot 10^{-4}$ Gy/pulse (which represents the response of the ionisation chamber at d_{max} for a 6 MV photon beam, field size of 10x10 cm^2). The error bars representing the uncertainties of the DUO measurements are two standard deviations.

For each dose rate, the response of the DUO is normalised to the dose measured by the ionisation chamber placed at the same SSD of DUO. Again, this is possible because it can be assumed that the ionisation chamber is dose rate independent.

The results obtained show a maximum DPP dependence of 27% in the whole range of dose rate evaluated.

5.4 Percentage depth-dose

The conditions of this experiment are exactly the same as for MP512 (paragraph 3.5): DUO is inserted into a PMMA holder composed of a slab of 5 mm on top and on the bottom of the detector, with a slab of 10 cm as backscattering material and several slabs on top to obtain the depth dose profile from 1.5 cm up to 30 cm depth. For this reason, the minimum depth of measurements was 5 mm water equivalent depth (WED).

The entire setup is irradiated with 100 MU by a field of 10x10 cm^2 at 100 cm SSD by a 6 MV photon beam.

Under the same experimental conditions (in solid water), a Markus ionisation chamber (PTW Freiburg - Germany) is irradiated: its readings are used to benchmark the results obtained with DUO.

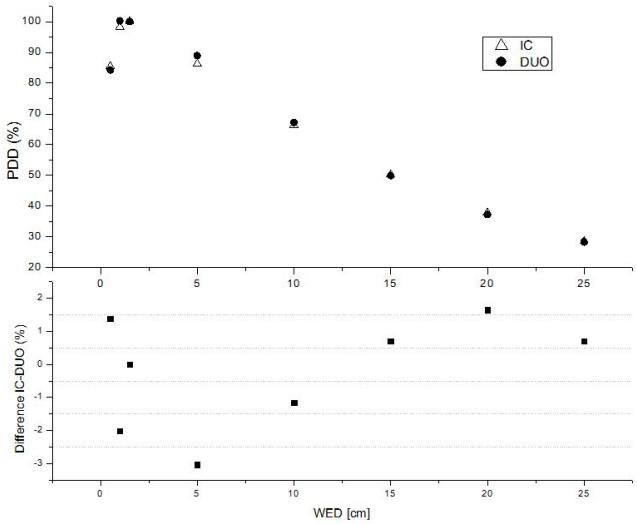

Figure 5.5: PDD measured with DUO of 6 MV photons, 10x10 cm^2 field in comparison with and Markus ion chamber.

This comparison is displayed in Figure 5.5: the observed maximum difference between PDDs is approximately -3%÷+1.5%.

5.5 Output factors

As for MP512 (paragraph 3.6), the reference field size for the output factors is 10x10 cm^2, measured at isocentre (10 cm in depth at SSD of 90 cm) [43]. The output factor is calculated by acquiring the response of the detector in a pixel in the neighbourhood of the crossing of the two microstrips for field size ranging from 0.5x0.5 to 30x30 cm^2.

Again, the output factor measured by DUO is directly compared with MOSkin and EBT3 film. These results are shown at Figure 5.6: it displays the response of the three detectors as a function of the field size.

For every field size, DUO always shows an under-response which goes up to -33.5% for 0.5x0.5 cm^2 when compared with EBT3 film. This is due

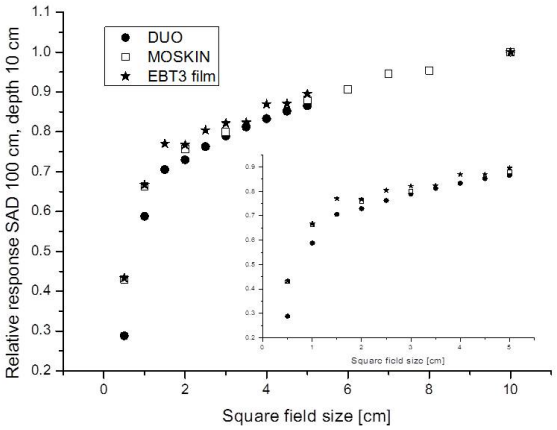

Figure 5.6: Field size dependence response of DUO, MOSkin and EBT3 film normalised to response at 10x10 cm^2 field size. The inset window shows a detail for field sizes smaller than 5x5 cm^2.

to the fact that the sensitive volume of each pixel is really small and the attenuation due to the silicon surrounding the sensitive volume plays an important role.

In order to mitigate this issue, as stated in [51] and [52], a possible solution is the reduction of the air gap above and around the silicon detector. This can be achieved filling the recess in the PMMA phantom with wax: this is a solid material which raises the attenuation of photons and secondary electrons. For this reason, the air gap can not be reduced above a certain threshold. A first try is run reducing the above gap from 2 mm to 1.5 mm and filling the lateral air gap in order to have a square of 6x6 cm^2 to generously fit the detector (as shown in Figure 5.7). On the top side, as the bonding is longer (view Figure 2.4), a special recess has been done in order to avoid any damage to the detector structure: this special feature is indicated in Figure 5.7.

The new results obtained under the same conditions except the changing in the air gap are compared with the old ones (without wax) in Figure 5.9.

The results are interesting as for small field sizes the relative response increases (up to a factor of 7.5% for field size 0.5x0.5 cm^2) while they are substancially unchanged for bigger field sizes.

The data obtained with DUO after wax filling are again compared with MOSkin, Pinpoint ionisation chamber and EBT3 film, and displayed in Figure 5.9

DUO features a behaviour which is an average trend between the ionisation chamber and EBT3 films (and MOSkins) for small field sizes, while for bigger field sizes all the four detectors feature similar values (with difference of approximately 2% between DUO and the EBT3 films). MOSkins and ionisation chambers are adequate detectors for dosimetry, which implies that DUO provides satisfactory properties.

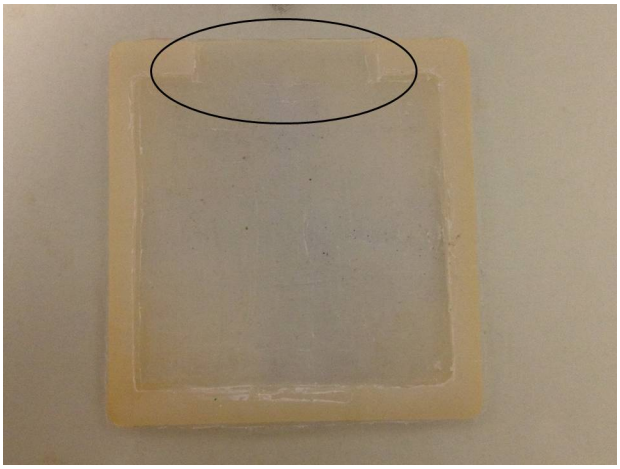

Figure 5.7: Wax filling of the PMMA phantom for DUO. A special recess for top side is detailed.

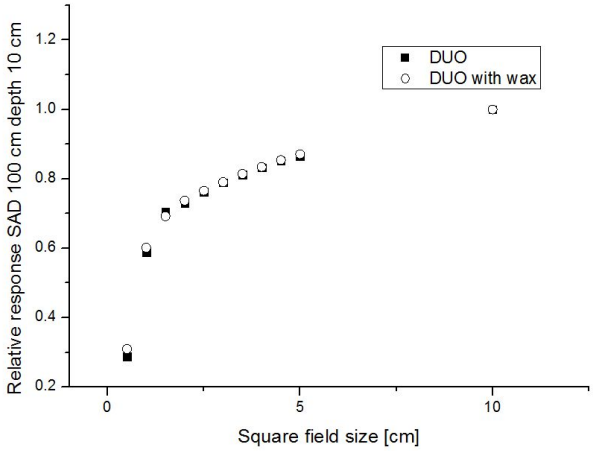

Figure 5.8: Comparison for output factors measured with DUO without and with wax filling in the PMMA phantom.

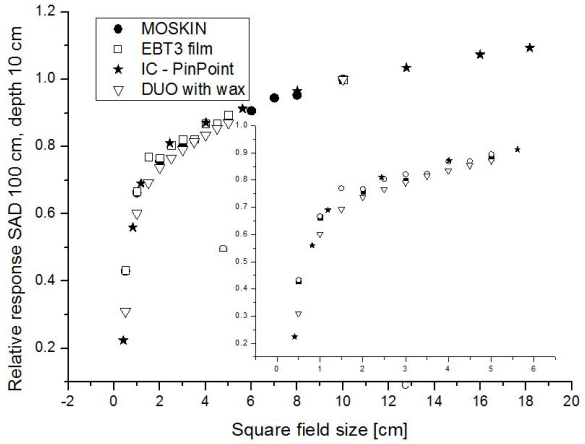

Figure 5.9: Field size dependence response of DUO after wax filling, MOSkin, Pinpoint ion chamber and EBT3 film normalised to response at 10x10 cm^2 field size. The inset window shows a detail for field sizes smaller than 5x5 cm^2.

Chapter 6

Movable Phantom

After having successfully tested MP512 and DUO for small field dosimetry applications as well as MP512 for ART applications, this chapter is centred on the Movable Phantom. This device has been designed to be used for QA of small field treatments on moving organs: in fact, it is conceived to integrate DUO (which has been shown to better fit for small field applications) and to be able to reproduce any lung motion pattern along one axis. For these reasons, the integrated system would fully fulfil all QA requests in order to cope with small fields and movement issues.

This chapter (paragraph 6.1) describes a verification solution of the moving capacity of the phantom. It has been run at CMRP laboratories and relys on an optical system which records the positions of the phantom and analyses the motion using a MATLAB (Mathworks. Inc) script. The aim of this second experiment is to confirm that the phantom motion pattern coincides with the reference lung motion pattern.

In fact, the last section (paragraph 6.2) presents a comparison between the lung pattern and the measured pattern, in order to have a quantitative characterisation of the moving system.

6.1 Phantom movement verification technique

As pointed out at paragraph 2.8, the magnetic sensor does not acquire its distance from the moving part of the phantom. For this reason, it is not possible to use it in order to verify that the movement coincides with the input lung motion pattern.

To verify the pattern, an optical solution has been used. It is based on two round shaped drawings and a chessboard sketch which play the role of position indicators. These figures are printed on two different paper sheets: in particular, the chess and one circle on one sheet which is glued on the fixed part of the phantom and the other circle on another sheet which is glued on the moving part of the phantom, as shown in Figure 6.1.

Once the moving pattern has been chosen, it is filmed using a webcam with a frame rate of 50 Hz and a video is generated. A MATLAB script receives the video as an input and is able to localise the center of the two

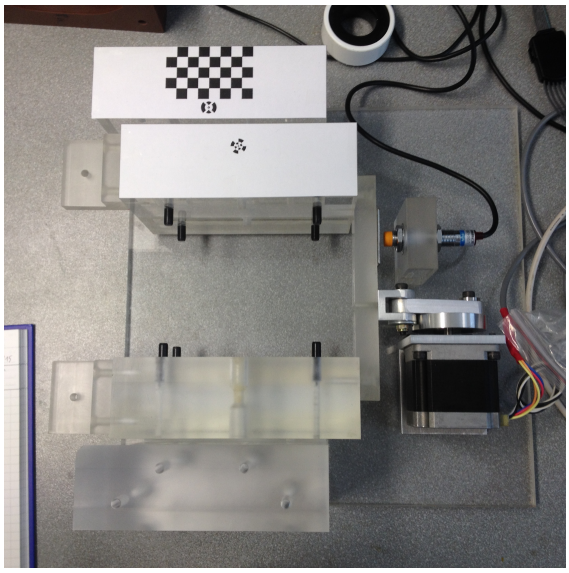

Figure 6.1: Phantom movement verification indicators.

circles and follow their positions as a function of time in terms of pixels. Relying on the fact that every square of the chess drawing measures 7x7 mm^2, it is also able to quantify the distance between the two points along the direction of the movement and generate a proper data array.

6.2 Comparison between theoretical and measured movement profiles

Using the technique just described, it is possible to characterise the performances of the movement system. In order to test it, it is useful to use a profile which includes different features: constant positions, increasing and decreasing wedges, inversion of the motion to verify the effect of the backslash. For this reason, the system has been tested using a "top hat" profile and is shown at Figure 6.2.

This regular profile is then compared with the profile that is obtained by the MATLAB script after the procedure described in the preceeding paragraph. As the two profiles have different spacings, they both have been interpolated using the MATLAB interpolation-shape-preserving fit with a spacing of 0.005 s: the two profiles are plotted at Figure 6.3.

The combined plot shows that the timing management is satisfactory as the two peaks coincide.

On the other hand, the movement along the Y axis respects the global trend of the input profile but the absolute distances are not satisfactory. In fact, if we consider the percentage difference between the measured and the input profiles every 0.005 s and then take the average value over 6 seconds (the whole time needed to run the top hat profile), the measured profile features an error of about 11%.

In particular, the second ramp (going from 5 to 10 cm) has a higher

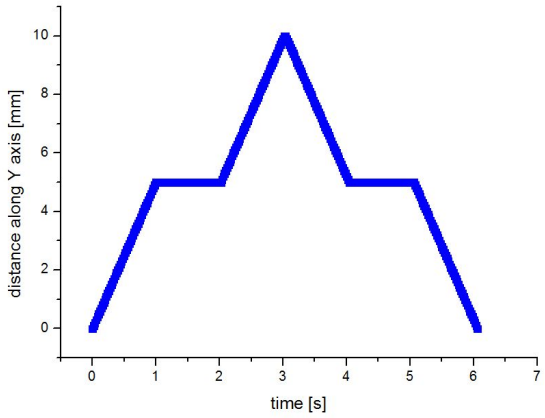

Figure 6.2: Plot of the "top hat" profile used to characterise the moving system performances.

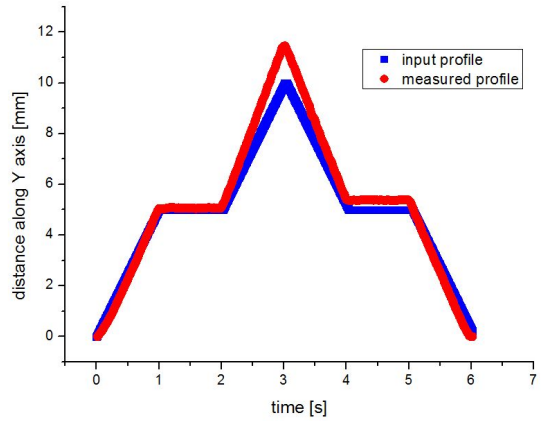

Figure 6.3: Plot of the "top hat" input profile and of the profile acquired via the MATLAB script.

growing rate, and the same happens after the back slash (from 10 to 5). In fact, the peak is at about 11.5 cm and not 10 (which is consistent with the overall 11% error), and the second plateau is not at 5 cm but 5.3: this last difference is equivalent to a 6% error, which is the effect of the backlash. The last decreasing ramp from 5.3 to 0 has a different steepness from the input one, which makes the profile reach a final zero value.

Although the results obtained with the "top hat" profile are not satisfactory, the Y axis lung profile at Figure 2.17 has been run and compared with the measured profile using the same just to have an idea of its behaviour. The results are shown at Figure 6.4: as they featured the same time spacing, no interpolation was needed.

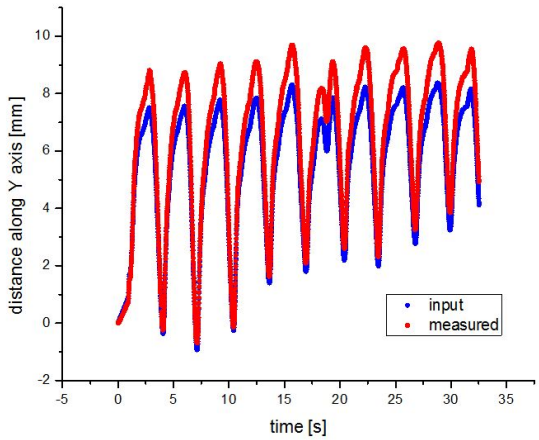

Figure 6.4: Plot of the lung motion input profile and of the profile acquired via the MATLAB script.

Again, the timing management is satisfactory as the peaks and valleys coincide in the two profiles, but the absolute distances are not adequate. In fact, the two profiles are really close to each other in the rises and falls, while the big differences are where the profile is flatter (between every rise and fall), leading to an overall error of about 17% (where 17% of the full dynamic range of the movement is 1.36 mm).

Chapter 7

Discussions and conclusions

In this study, several components of the Movable Phantom were developed, studied and characterised.

The silicon detector MP512 has shown acceptable performances in terms of static characterisation and spatial resolution. In fact, variation of the response between the diodes in a flat field was ± 0.25% after the uniformity correction. Percentage depth dose measurements of the MP512 were compared to those with ion chambers and agreed to within 1.5% for the depth. Dose rate dependence of the MP512 was evaluated by comparison of the response to an ion chamber. MP512 shows a dose per pulse dependence within 1% down to 3.5×10−5 Gy/pulse (approximately one order of magnitude lower than in-field DPP) while it shows approximately 5% at the lowest DPP of 0.9×10−5 Gy/pulse. The normalised beam profile distributions for square field sizes between 0.5 and 4 cm were measured with the MP512 and compared to Gafchromic EBT3 film. The MP512 showed excellent performance in beam profile reconstruction (FWHM discrepancy less than 1.3%) but, in spite of much higher spatial resolution and pixel size of available 2D diode array, MP512 produced a discrepancy in the penumbra of less than 0.4 mm for the smallest fields. This discrepancy still falls within the acceptance criteria of 1 mm generally accepted for small field dosimetry penumbra but represents approximately 20% of the total penumbra as a 0.5x0.5 cm^2.

At the same time, MP512 with designed build up is able to reconstruct the dose profiles in X and Y directions for different square radiation fields in case of no-motion, motion and tracking of the detector with a discrepancy within 0.4 mm and 4% in penumbra width and FWHM, respectively, when compared to EBT3 film. MP512 is also able to record the instantaneous dose deposited pulse-by-pulse allowing for an accurate real time or retrospective analysis of the dose escalation measured by each pixel. Performance of motion adaption algorithm for DMLC in conjunction with Calypso motion tracking system was investigated by MP512 for typical lung motion pattern in case of a 3x3 cm^2 field size dynamic wedge delivered by the MLC. It was demonstrated that DMLC motion tracking in this case is excellent leading to dose discrepancy with stationary MP512 less than -3% along the wedge dose profile and a maximum discrepancy of +15% in penumbral region of

the wedge. In case of absence of motion tracking an average dose difference of -18% along the wedge and a peak of +75% in the penumbra region were measured. Retrospective analysis of temporal response of each pixel during the dynamic wedge delivery in case of motion tracking allowed investigating how DMLC and motion adaptive algorithm manage interplay effect due to MLC and target motion. It was demonstrated that existing algorithm is providing large instantaneous discrepancy in penumbral regions of the field were dose gradient is steep including movable penumbras determined by MLC motion. This effect is due to latency of the tracking algorithm as reported previously. This feature of the MP512 system is particularly useful when a motion predictive algorithm is adopted to drive the DMLC to tune the parameters of the tracking system maximizing its effectiveness. In fact, in this way the MP512 makes the Quality Assurance a practice that can actively improve the performances of treatment techniques on the grounds of quantitative information and not only a passive verification.

Nevertheless, basing on Nyquist sampling theory, it is has been shown that the spacing properties of MP512 are not sufficient when small field sizes are implied in the treatment. In fact, a minimum pitch of about 210 μm is necessary to sample field sizes of 0.5x0.5 mm^2 without any loss of information. For this reason, the silicon detector DUO has been designed: it features a pitch of 200 μm, which is much smaller than MP512 and EBT3 film pitches. This device has undergone a preliminary characterisation in terms of static performances, which revealed DUO properties to be satisfactory.

Finally, the Movable Phantom has been designed using mainly timber and PMMA in order to mimic the lung and thorax structure and movement. It consists in a moving device which is able to reproduce along one direction the typical lung motion pattern thanks to a motion management system based on a stepping motor, an FPGA and a digital step driver. A primary and home-made technique has been conceived in order to verify its motion management: it is based on a system of optical references which are filmed by a webcam and analysed using MATLAB features. This study has shown that the general operation of the device is acceptable in terms of timing, but the absolute spatial movement needs to be tuned as it shows an under-response of approximately 11%. This same verification technique has been used for a specific lung motion pattern, leading to a global error of about 17%.

7.1 Limitations

A fundamental point is constituted by the fact that MP512 has not been completely characterised. In fact, before it can be used as a QA device, it needs to undertake some extra studies: the fundamental missing point is its angular dependence. It could be useful to run these missing tests using a static phantom in combination with small field size beams, as it would have a more clinical significance. Strategies to compensate the angular response

of a monolithic silicon detector are well known and include applying either angular correction factors or placement of MP512 in a rotatable cylindrical phantom that rotates synchronically with the gantry providing the beam incidence normally to the detector [59], [60]. Despite the more challenging design necessary for the phantom, this approach is feasible considering that HexaMotion is originally designed for Delta4 and is able to manage the weight associated with the cylindrical drum of the rotatable phantom.

In particular, concerning the dynamic study, an issue which implies the lack of angular dependence characterisation is the use of the gantry in a fixed (vertical) position, with no rotation around the phantom as it would happen in real SRS and SBRT treatments.

Another strong limitation of this work is that only one motion pattern was used. All the results and conclusions taken by this study rely on the specific pattern that has been used: it has been chosen for his regular shape, but it might not be a representative sample. What is more, it just features a movement on the XY plane, without any variation of the detector distance from the head of the linac. A change in SSD would contribute to a variation of the dose rate measured by the detector: assuming that the tumor is not deformable, the effect of this component would lead to uncertainties in the estimation of the performance of MP512 in determining the mitigation of the dose variation in X and Y directions by DMLC tracking system.

Theoretically, DUO should overtake all MP512 limitations. In reality, the sensitive volume is so small that other problems raise, such as a strong under-response when very small fields are considered(as shown in paragraph 5.4) which requires a reduction of the air gap between the detector and the PMMA phantom. As this aim can be reached using some wax above and around the detector, a proper study needs to be done in order to characterise the effect of the lateral and the superior air gap.

Finally, as it is the first prototype that has been designed, the Movable Phantom features some issues in the reproduction of the lung motion pattern. This could be due to the motion management system itself or even in the motion verification. For this reason, an improvement in the components of the motion management system (particularly in the digital step driver) as well as a different solution for the measurement of the distance run by the phantom (a laser yardstick for example) must be taken into account.

7.2 Future work

DUO represents a further improvement of MP512 as it features a 2D spatial capability but a pitch sensibily smaller. At the same time, DUO has a cross pixels disposition which does not allow a complete 2D mapping of the beam. For this reason, MP512 is still a valuable device which might need some specific improvements. For example, introducing a small air gap above the detector would mitigate the dose enhancement produced by the silicon chip die.

As stated before, a clinical characterisation (angular and energy de-

pendence) would be useful from the treatment point of view. Strategies to compensate the angular response of a monolithic silicon detector are well known and include applying either angular correction factors or placement of MP512 in a rotatable cylindrical phantom that rotates synchronically with the gantry providing the beam incidence normally to the detector [59] [60]. Despite the more challenging design necessary for the phantom, this approach is feasible considering that HexaMotion is originally designed for Delta4 and is able to manage the weight associated with the cylindrical drum of the rotatable phantom.

Monte Carlo simulation of the MP512 will be also carried out for full optimisation of its design for small field QA dosimetry applications. A comprehensive Monte Carlo model of the MP512 detector and the linac head (space file for generation of the accurate spectrum of the source) is currently being developed. The MP512 combined with the use of the rotatable phantom is a powerful tool, with real-time, accurate 2D, and potentially 3D, dose reconstruction capabilities for pre-treatment QA for SBRT and SRS verification.

In order to obtain a total movement characterisation, a further study will include a movement along the Z axis and investigate the effect of depth variation on the detector response in a full 4D motion patterns from different organs and compare the results to film dosimeters.

All these improvements will then be applied to several lung motion patterns, in order to verify if the results obtained in this first study are general or depend drastically on the single motion profile. In this way, it would also be possible to define properly the criteria that could be used to tune the proportional and derivative coefficients of the tracking system to make them match to the single lung motion pattern.

Concerning DUO, up to now it has just undergone a basic characterisation. For this reason, all the studies done and foreseen for MP512 should be reproduced with DUO: thanks to its specific pitch properties, it would become the new golden standard in terms of spatial resolution and real time reading as well as, thanks to the fast DAQ, be able to perform the timing analysis described for MP512. In this way, it would provide better results than EBT3 films in spatial terms and feature pulse-per-pulse dose analysis, overtaking films and allowing to avoid the long and boring post-processing.

About the Movable Phantom, it has been shown that it needs refinement in order to raise its performances up to the level of MP512 and DUO. As the errors are small in terms of absolute values (less than 1.5 mm), a possible solution could just be the use of kapton tape around some moving components in order to reduce the sliding during the movement and mitigate the global inaccuracy.

What is more, another couple of timber pieces (Figure 7.1) has been conceived and realised: it has the same characteristics, except the fact that it features two hemispheric recesses (one per each piece) in correspondence of the center of the detector. This modification has a clinical aim: in fact, these holes are filled with solid water and represent the tumor. In this specific case, the detector would be in the middle of the tumor and allow

to study the effects of the presence of the non-homogeneity. In order to characterise this new configuration of the phantom, it is worth considering a 4D-CT of the phantom: it would allow to determine the relative scattering properties of every different piece of the phantom.

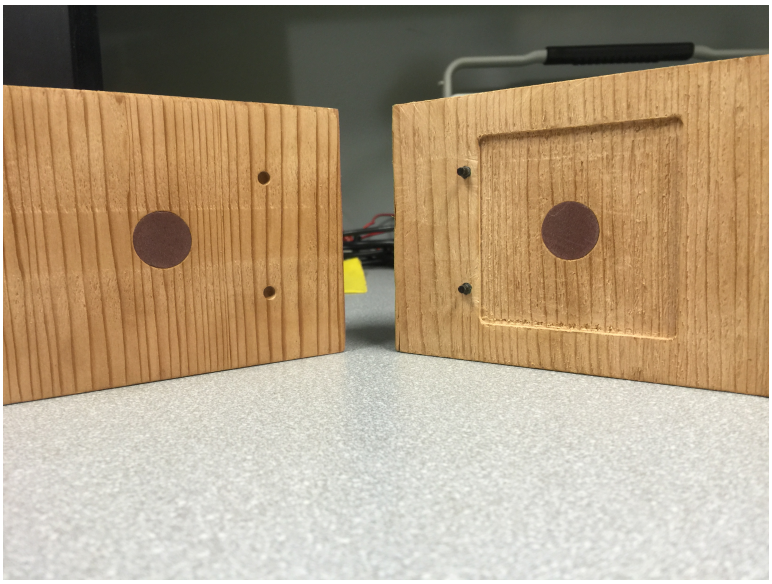

Figure 7.1: New timber pieces: they feature two solid water hemispheres representing the tumour.

Once this aim is reached, the physical integration of DUO in the Movable Phantom and of the data acquisition chain with the motion management system is possible. This last step would allow to avoid the HexaMotion platform for QA purposes: as the costs of the two technologies are described by two different order of magnitudes, this will lead to substantial cost cuts with improved performances.

Appendix A

Electromagnetic radiation interactions

In this appendix we focus on the most important gamma radiation-matter interactions. When considering interactions of medical linear accelerator emitted photons and biological tissues, only three interactions have a real significance:

1. photoelectric effect,
2. Compton effect,
3. pair production.

General references can be found in [2] and [61].

A.1 Photoelectric effect

This kind of interaction (Figure A.1) consists in a complete absorption of an incident photon by an atom and the subsequent emission of one of its electrons , called in this precise case photoelectron. This event would not be possible with a free electron because it would be impossible to satisfy the conservation of linear momentum (the photon should travel with a speed equal to 2c). For incident photons of sufficient energy, the photoelectron is usually emitted from the most tightly bound shell (also called K shell) of the atom.

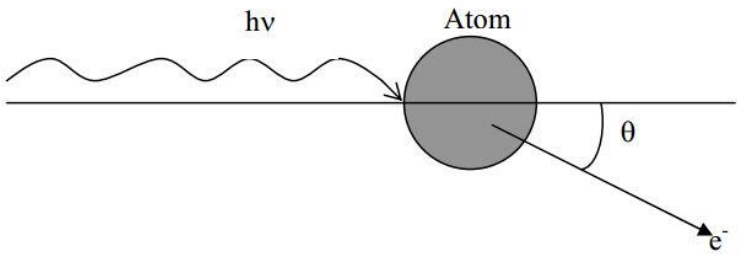

Figure A.1: Schematic representation of a photoelectric interaction. [2]

The law of conservation of energy leads to the following formula, which states energy contributions in this interaction:

$$E_e = h\nu + E_b \tag{A.1}$$

where E_e is the energy of the photoelectron, $h\nu$ is the energy of the incident photon and E_b is the binding energy of the electron in its original shell in the atom. Since during this interaction the incident photon disappears, the photoelectric effect is also known as *photoelectric absorption*.

If we wanted to relate the cross section of this particular interaction to the energy of the photon $E_\gamma = h\nu$ and the nature of the absorber material (its atomic number Z), a good approximation would be

$$\sigma_{pe} \sim \frac{Z^n}{E_\gamma^{3.5}} \tag{A.2}$$

where n varies from 4 to 5 depending on E_γ.

A.2 Compton effect

This process takes place between an incident photon and an electron (treated as a nearly free electron) in the absorbing material: it consists in the deviation of the photon through an angle θ with respect to its original direction (Figure A.2). In order to satisfy conservation laws, the photon transfers a portion E_e of its energy to the electron (assumed to be initially at rest), which is then called recoil electron.

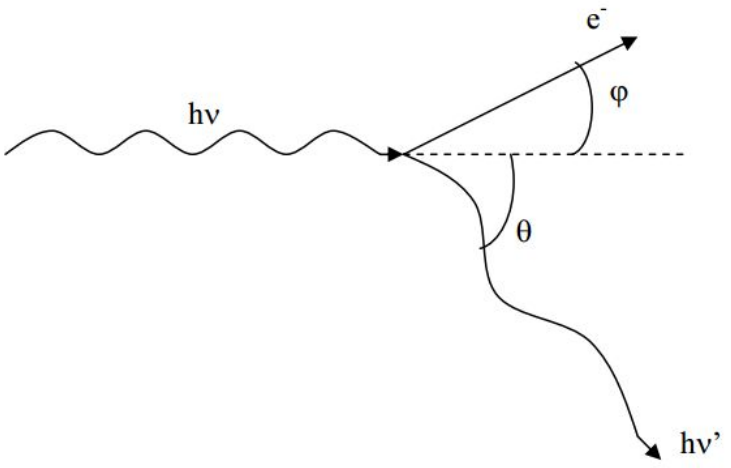

Figure A.2: Schematic representation of a Compton scattering. [2]

According to energy conservation law, the re-emitted photon has an energy

$$h\nu' = h\nu - E_e = \frac{h\nu}{1 + \frac{h\nu}{m_e c^2}(1 - \cos\theta)} \tag{A.3}$$

smaller that the energy of the incident photon $h\nu$ as θ can assume values from 0 to 180°.

As no particle is absorbed or created, this interaction is also known as *Compton scattering*.

A good approximation to relate the cross section of this particular interaction to the energy of the photon $E_\gamma = h\nu$ and the nature of the absorber material (its atomic number Z) would be

$$\sigma_C \sim Z \tag{A.4}$$

due to the fact that all atomic electrons are implied in the process.

Considering that biological tissues is mostly composed with low-Z elements (hydrogen, nitrogen, carbon, oxygen), the Compton effect is the most likely interaction.

A.3 Pair production

With photons of energy bigger than the threshold $2{m_e}^2$=1.022 MeV, another interaction, called pair production, becomes possible. As a result of the interaction between this high energy-photon and the Coulomb field generated by the nucleus of an atom, the photon is completely absorbed and an electron-positron pair is produced (Figure A.3). According to the energy and momentum conservation laws, this would not be possible in vacuum.

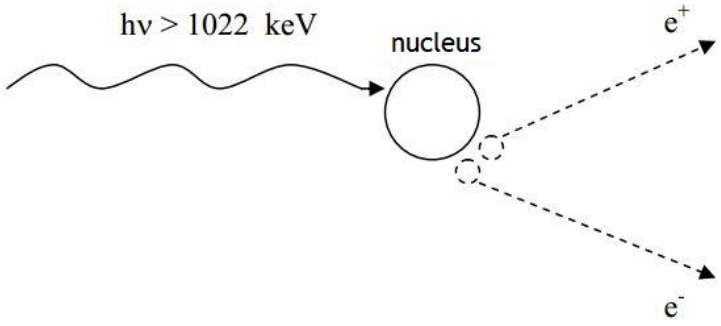

Figure A.3: Schematic representation of a pair production interaction. [2]

The existence of antiparticles is justified by quantistic theory, according to which $E^2 = (mc^2)^2 + (pc)^2$, where negative energy levels are also accepted. Negative and positive energy levels for each kind of particle are separated by an energy gap equal to the double of the particle's rest energy. If we consider electrons, whose invariant mass is equal to 0,511MeV, it results evident why it is necessary at least a 1,022MeV photon to create a positron-electron pair. If the photon has an energy larger than 1,022MeV, the exceeding energy is shared equally between the two resultant particles (as their masses are equivalent), giving rise to the following energy conservation equation:

$$h\nu = E_e + E_p + 2m_o c^2 \tag{A.5}$$

where E_e is the electron energy, E_p is the positron energy and m_o is the electron and positron rest mass. The cross section for pair production can be approximated as

$$\sigma_{pp} \sim Z^2 \tag{A.6}$$

and grows with incident photon energy.

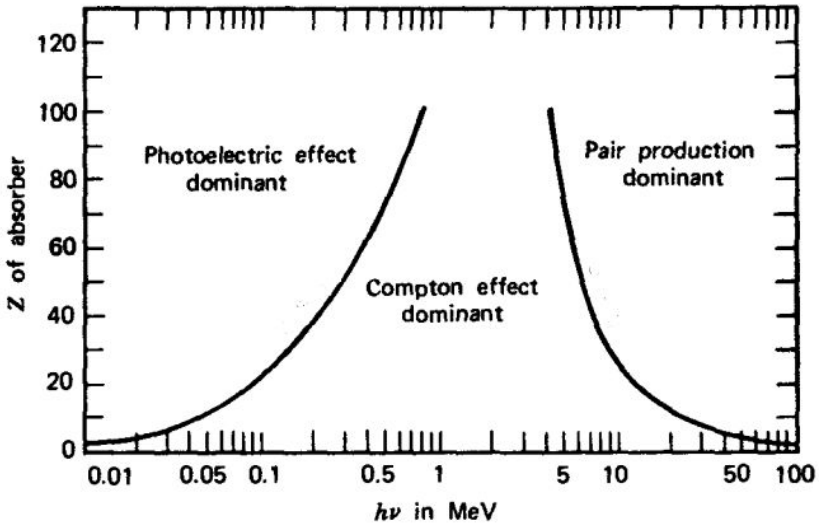

Figure A.4: Relative importance of the three photon-matter interactions. The two lines shows the values of Z and hν for which the two neighbouring effects are equal [61].

Appendix B

Charged particle equilibrium

The object of this appendix is the description of the charged particle equilibrium.

B.1 General considerations

Any radiation detector can be schematized as an active volume enclosed in a wall surrounded by the remaining environment as represented in Figure A.3.

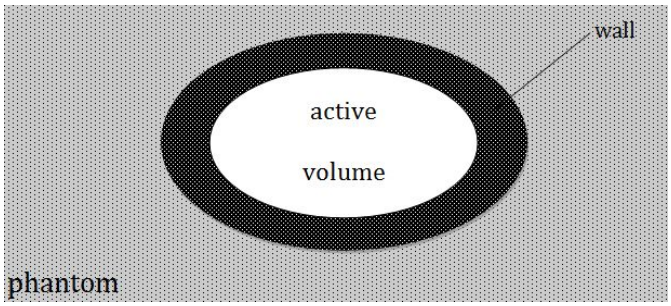

Figure B.1: Schematic representation of a radiation detector.

For this reason, the dose can be calculated thanks to an energy balance involving radiant energies:

$$D = \frac{1}{m} \times (E^{\gamma}_{in} - E^{\gamma}_{out} - E^{\gamma,e}_{out} + E^{e}_{in} - E^{e}_{out} - E^{e,\delta}_{out} + E^{\delta}_{in} - E^{\delta}_{out}) \quad \text{(B.1)}$$

where m is the mass of the active volume, the index *in* represents radiant energies penetrating it and *out* radiant energies escaping it, γ refers to photons, e to secondary electrons (electrons generated as ionization products) and δ to delta electrons (secondary electrons with enough energy to escape a significant distance away from the primary radiation beam and produce further ionization). The mixed high indices refer to interactions within the active volume: γ, e describes the electrons generated by a photon in m, and e, δ delta electrons generated by electrons in m.

B.2 Secondary electron equilibrium

The condition of *electron equilibrium* is been proven when incoming and outcoming energies transported by electrons are balanced: this means that the last six terms in equation B.1 cancel each other. This implies that the dose in the detector is only dependent on the energy transported into and out by photons. A less restrictive case is represented by the allowance of delta particle disequilibrium: in this case

$$- E_{out}^{\gamma,e} + E_{in}^{e} - E_{out}^{e} = 0 \tag{B.2}$$

which means that the deposited energy read by the detector is only due to photons and delta particles.

B.3 Bragg-Gray cavity theory

Under *Bragg-Gray* conditions, incoming and outcoming energies transported by photons and delta electrons are balanced: this represents the opposite extreme compared with secondary electron equilibrium. In fact, the energy balance equation

$$E_{in}^{\gamma} - E_{out}^{\gamma} - E_{out}^{\gamma,e} - E_{out}^{e,\delta} + E_{in}^{\delta} - E_{out}^{\delta} = 0 \tag{B.3}$$

states that in this case only secondary electrons are measured.

In megavoltage radiation, however, delta electrons have such a large energy that equation B.3 can not be satisfied. This new configuration is called *Spencer-Attix extension of Bragg-Gray cavity theory.*

Appendix C

Sampling theory and Nyquist-Shannon theorem

In this appendix, we shortly approach the signal processing and the sampling theory. The basic idea of these fields is that signals are seen as mathematical functions of time: in fact, variations in time of a particular physical quantity represent the signal itself. Signal theory aim is then the description of these signals in order to work with them mathematically. The first (and most important) classification of signals is based on their continuousness:

1. discrete-time signal: the signal is a sequence of points, where the distance in time between two values can be constant or variable. The corresponding signal is called *digital signal*;

2. continuous-time signal: the mathematical function is continuous (it assumes a value for every value of time). In juxtaposition with the analog signal, this signal takes the name of *analog signal*.

Nowadays, a fundamental point of signal processing is the conversion from analog to digital signal: in fact, it represents the basis for the "digital revolution".

C.1 The sampling theorem

The fundamental step in the conversion from analog to digital is the sampling of the signal: it consists in taking samples from a continuous-time signal every Δt seconds (this is called *sampling interval* and its inverse $f_s = \frac{1}{\Delta t}$ is called *sampling frequency*). This operation should give a discrete signal that carries the exact information of the analog one: in fact, the old analog signal should be completely reconstructable.

Intuitively, one can expect that the fidelity of the interpolation from the digital to the analog signal depends on the density of the original samples: in fact, it exists a minimum frequency that guarantees that no information is lost in the whole process.

The exact criterion is formally stated by the *Nyquist-Shannon theorem*. If we consider a signal as a mathematical function $s(t)$ of time, this has to

verify a fundamental condition for the theorem to be applied: its Fourier transform is zero outside of a finite region, and the frequency corresponding to the maximum is f_{max}.

Depending on the field of application of the beam, different band widths can be defined. Usually, the filter is stated at the frequency corresponding to -3dB with respect to the peak (which means half of the peak value): in fact, this corresponds to consider half of the power of the signal. This new frequency is called f_{bw}.

The minimum sampling frequency must then satisfy the following condition:

$$f_s \geq 2f_{bw} \tag{C.1}$$

where

$$f_N = 2f_{bw} \tag{C.2}$$

is known as *Nyquist frequency* and guarantees a loseless sampling.

Appendix D

Control theory and feedback loops

The aim of this appendix is to give a brief overview of basic automatic control principles. A general reference can be found here [62].

D.1 Control problems

Control problems consist in the imposition of a particular behaviour to a particular process of a dynamic system: in physical terms, we act on some input quantities (known as *control variables*) in order that output quantities (also called *controlled variables*) can reach a desired value (called *reference*), which can be fixed or changing. Usually, controlled variables do not only depend on control variables, but also on other quantities which we can not act on: these quantities are called *disturbances*. Sometimes, even if they can not be changed, they can be measured, procuring some extra information that can help in understanding the evolution of the system. Anyway, the fundamental point of control theory is that every quantity depends on time. In order to act on control variables and reach the reference values, a device called *controller* is introduced: the combination of process and controller takes the name of *plant*. As for the majority of practical plants the perfect identity between controlled variables and references is not reachable, it is useful to define an error which is the difference between the reference and the controlled variable:

$$\epsilon = reference - controlled\ variable \tag{D.1}$$

where ϵ represents the numerical value of the error. Hence, the aim of the controller is to make this error reasonably small, where reasonably has a mathematical meaning that has to be specified depending on the specific system. This new formulation corresponds to a simpler mathematical description, as the aim of control theory can just be described as make ϵ tend to zero:

$$\epsilon \longrightarrow 0 \tag{D.2}$$

when control variables tend to the values we want them to reach.

D.2 Control loops

The logic of control systems is that the controller acts on control variables: their changes have some effects on the system. Then, some of the quantities that describe it (or even all of them): among these, if everything works properly, the controlled variables tend to the reference values as much as possible. Therefore, it is necessary for the controller to have some input information: reference quantities and, if possible, the disturbances. In this case, we talk about *open-loop* (or *non-feedback* or *feedforward*) controllers (Figure D.1).

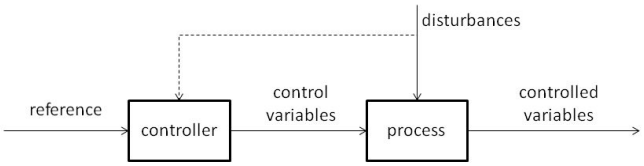

Figure D.1: Open-loop control system.

Sometimes, controlled variables can be measured and made available to the controller: the latter can then act on control variables knowing the value of the error ϵ. These devices are called *closed-loop* or *feedback* controllers Figure D.2. This second class of controllers is obviously more powerful: the bigger is the availability of information, the more effective is the action that controllers can make on the system.

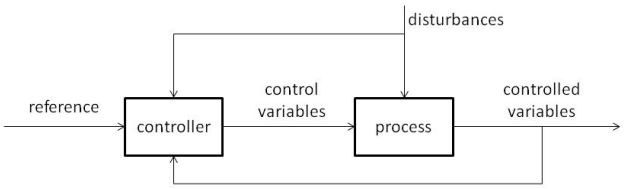

Figure D.2: Closed-loop control system

An important statement is that all the boxes and arrows in Figure D.1 and D.2 have a correspondent mathematical meaning: in fact, a complete mathematical reformulation of the system and all its components is necessary to formalize control theory. At the same time, this process of abstraction from the physical world makes control theory relevant for several and diverse applications. In order to have easy (or at least not too complex) mathematical problems, it is useful to describe systems using systems of dynamic linear equations. When this is not possible, a linearization in the neighbourhood of the equilibrium point turns out to be a successful strategy in most cases.

D.3 PID controllers

The most general kind of linear controllers is called *PID* as it is formed by 3 different terms: differential, integral and proportional, denoted respectively with *P*, *I* and *D*. Each of these contributions depends on the error ϵ in a different way, but the result is that the control variable can be expressed as

$$u(t) = u_P(t) + u_I(t) + u_D(t) \tag{D.3}$$

where each term corresponds to a different action of the controller on the error.

D.3.1 Proportional term

This action is proportional to the value of the error itself: in fact, the error is multiplied by a suitable constant k_P so that

$$u_P(t) = k_P \times \epsilon(t) \tag{D.4}$$

is the partial contribution to the new control variable and depends only on the present value of ϵ. For the latter point, this controlled is referred as "present". A proportional controller can regulate many processes and provide stability against small disturbances, but it can not deal with steady disturbances. For this reason, the integral term was introduced.

D.3.2 Integral term

The integral term is proportional to the integral of error in time, multiplied by a another suitable constant k_I:

$$u_I(t) = k_I \times \int_0^t \epsilon(\tau) d\tau \tag{D.5}$$

where the upper bound t coincides with the time at which the controller is operating. This definition makes the action of the integral controller "remember" the past behaviour of the error: for this reason, its contribution is not necessarily null even if the error is. The fact that the integral controller depends on the past values of ϵ makes this term referred as the "past" controller.

D.3.3 Derivative term

The last term is proportional to the derivative of the error through the constant k_D:

$$u_D = k_D \times \frac{d\epsilon}{d\tau}(t) \tag{D.6}$$

and has been added in order to improve the performances of the controller. In fact, its contribution leads to a quick compensation of variations of disturbances: as far as ϵ grows, the controller tries to compensate this change depending on the speed of the change, without caring about its absolute value (proportional action) or waiting for a certain time (integral action). As its action tries to predict the system behaviour and act consequently, it is also called "future" controller. At the same time, if the error shows a step function-like behaviour, this term would tend to infinity, making the whole controller too sensitive.

D.3.4 Global control law

Finally, the control law that links the control variable and the error has the shape

$$u(t) = u_P(t) + u_I(t) + u_D(t) = k_P \times \epsilon(t) + k_I \times \int_0^t \epsilon(\tau) d\tau + k_D \times \frac{d\epsilon}{d\tau}(t) \quad \text{(D.7)}$$

which shows the linear nature of the PID controller.

Acronyms

ADC
Analogue-to-Digital Converter

ART
Adaptive motion Radiation Therapy

CAX
Central Axis

CI
Conformity Index

CMRP
Centre for Medical Radiation Physics

CPE
Charged Particle Equilibrium

CT
Computed Tomography

DAQ
Data Acquisition System

DMLC
Dynamic Multi-Leaf Collimator

DPP
Dose Per Pulse

DTA
Distance To Agreement

EBRT
External Beam Radiation Therapy

EPID
Electronic Portal Imaging Device

FFT
Fast Fourier Transform

FPGA
Field Programmable Gate Array

FS
Field Size

FWHM
Full Width at Half Maximum

GUI
Graphical User Interface

ICCC
Illawarra Cancer Care Centre

IMAT
Intensity Modulated Arc Radiotherapy

IMRT
Intensity Modulated Radiation Therapy

IR
Infra Red

MLC
Multi-Leaf Collimator

MOSFET
Metal Oxide Semiconductor Field-Effect Transistor

MP512
Magic Plate 512

MR
Magnetic Resonance

MU
Monitor Unit

OAR
Organ(s) At Risk

OD
Optical Density

OF
Output Factors

OSLD
Optically Stimulated Luminescence Dosimeter

PCB
Printed Circuit Board

PDD
Percentage Depth Dose

PET
Positron Emission Tomography

PMMA
Poly(methyl methacrylate)

PSD
Plastic Scintillating Detector

PTV
Planning Target Volume

QA
Quality Assurance

RF
Radiofrequency

RGB
Red Green Blue

RHS
Right Hand Side

RNSH
Royal North Shore Hospital

RPM
Real time positioning

SBRT
Stereotactic Body Radiation Therapy

SPI
Serial Protocol Interface

SRS
Stereotactic RadioSurgery

SSD
Source to Surface Distance

TLD
Thermoluminescent Detector

TP
Treatment Planning

TPR
Tissue Phantom Ratio

TPS
Treatment Planning System

VMAT
Volumetric-Modulated Arc Therapy

WED
Water Equivalent Depth

Bibliography

[1] Johnny E Morales, Scott B Crowe, Robin Hill, Nigel Freeman, and JV Trapp. Dosimetry of cone-defined stereotactic radiosurgery fields with a commercial synthetic diamond detector. *Medical physics*, 41(11):111702, 2014.

[2] Stefano Agosteo. *Dispense del corso di "Applicazioni medicali delle radiazioni"*, 2013.

[3] Lung cancer fact sheet. `http://www.lung.org/lung-disease/lung-cancer/resources/facts-figures/lung-cancer-fact-sheet.html`. Accessed: 2014-11-20.

[4] International Agency for Research on Cancer et al. World cancer report 2014. *Geneva: WHO*, 2014.

[5] Indra J Das, George X Ding, and Anders Ahnesjö. Small fields: Nonequilibrium radiation dosimetry. *Medical physics*, 35(1):206–215, 2008.

[6] Stephanie Lang, Jörg Zeimetz, Gregor Ochsner, Marianne Schmid Daners, Oliver Riesterer, and Stephan Klöck. Development and evaluation of a prototype tracking system using the treatment couch. *Medical physics*, 41(2):021720, 2014.

[7] Marianne Falk, Per Munck af Rosenschöld, Paul Keall, Herbert Cattell, Byung Chul Cho, Per Poulsen, Sergey Povzner, Amit Sawant, Jens Zimmerman, and Stine Korreman. Real-time dynamic mlc tracking for inversely optimized arc radiotherapy. *Radiotherapy and Oncology*, 94(2):218–223, 2010.

[8] Paul J Keall, Amit Sawant, Byungchul Cho, Dan Ruan, Junqing Wu, Per Poulsen, Jay Petersen, Laurence J Newell, Herbert Cattell, and Stine Korreman. Electromagnetic-guided dynamic multileaf collimator tracking enables motion management for intensity-modulated arc therapy. *International Journal of Radiation Oncology* Biology* Physics*, 79(1):312–320, 2011.

[9] Calypso localisation system. `https://www.varian.com/`. Accessed: 2014-11-20.

[10] Patient positioning and setup - beacon. http://radonc.ucsf.edu/research_group/jpouliot/tutorial/hu/Lesson20.html. Accessed: 2015-06-01.

[11] Paul J Keall, Emma Colvill, Ricky O'Brien, Jin Aun Ng, Per Rugaard Poulsen, Thomas Eade, Andrew Kneebone, and Jeremy T Booth. The first clinical implementation of electromagnetic transponder-guided mlc tracking. *Medical physics*, 41(2):020702, 2014.

[12] Amish Shah, Patrick Kupelian, Twyla Willoughby, and Sanford Meeks. Expanding the use of real-time electromagnetic tracking in radiation oncology. *Journal of Applied Clinical Medical Physics*, 12(4), 2011.

[13] Ryan L Smith, Amit Sawant, Lakshmi Santanam, Raghu B Venkat, Laurence J Newell, Byung-chul Cho, Per Poulsen, Herbert Catell, Paul J Keall, and Parag J Parikh. Integration of real-time internal electromagnetic position monitoring coupled with dynamic multileaf collimator tracking: An intensity-modulated radiation therapy feasibility study. *International Journal of Radiation Oncology* Biology* Physics*, 74(3):868–875, 2009.

[14] Amit Sawant, Ryan L Smith, Raghu B Venkat, Lakshmi Santanam, Byungchul Cho, Per Poulsen, Herbert Cattell, Laurence J Newell, Parag Parikh, and Paul J Keall. Toward submillimeter accuracy in the management of intrafraction motion: the integration of real-time internal position monitoring and multileaf collimator target tracking. *International Journal of Radiation Oncology* Biology* Physics*, 74(2):575–582, 2009.

[15] Martin J Menten, Matthias Guckenberger, Christian Herrmann, Andreas Krauß, Simeon Nill, Uwe Oelfke, and Jürgen Wilbert. Comparison of a multileaf collimator tracking system and a robotic treatment couch tracking system for organ motion compensation during radiotherapy. *Medical physics*, 39(11):7032–7041, 2012.

[16] Igrt: introducing the next generation. http://medicalphysicsweb.org/cws/article/research/43771, note = Accessed: 2014-11-20.

[17] Vero imaging and treatment integrated system. http://www.epsilonelektronik.com/Tr/?Page=2&CatID=19&SubCatID=45, note = Accessed: 2014-11-20.

[18] Manuela Burghelea, Dirk Verellen, Thierry Gevaert, Tom Depuydt, Kenneth Poels, Viorica Simon, and Mark De Ridder. Feasibility of using the vero sbrt system for intracranial srs. *Journal of Applied Clinical Medical Physics*, 15(1), 2014.

[19] H. Palmans K. Rosser M.M. Aspradakis, J.P. Byrne. *IPEM Report Number 103: Small Field MV Photon Dosimetry.* Institute of Physics and Engineering in Medicine, York, 2010.

[20] S.H. Benedict, D.J. Schlesinger, S.J. Goetsch, and B.D. Kavanagh. *Stereotactic Radiosurgery and Stereotactic Body Radiation Therapy*. CRC Press, 2015.

[21] Peter Metcalfe, Thomas Kron, and Peter Hoban. *The physics of radiotherapy x-rays and electrons*. Medical Physics Publ., 2012.

[22] Treatment machines for external beam radiotherapy. `http://www.irsn.fr/fr/professionnels_sante/documentation/documents/syllabus_chapitre_5.pdf`, note = Accessed: 2014-12-10.

[23] A Wagner, F Crop, T Lacornerie, F Vandevelde, and N Reynaert. Use of a liquid ionization chamber for stereotactic radiotherapy dosimetry. *Physics in medicine and biology*, 58(8):2445, 2013.

[24] Octavius detector 729 xdr. `http://www.ptw.de/octavius_729_xdr.html`, note = Accessed: 2014-12-10.

[25] Mapcheck 2. `http://www.imagingequipment.co.uk/product/705-198/MapCHECK-2`, note = Accessed: 2014-12-10.

[26] e-lectron newsletter. `http://www.radpro.eu/news/newsletter31/April09_Electron.html`, note = Accessed: 2014-12-10.

[27] Delta4 imrt pretreatment qa system. `http://medicalphysicsweb.org/cws/product/P000007563`, note = Accessed: 2014-12-10.

[28] Bijan Arjomandy, Ramesh Tailor, Aman Anand, Narayan Sahoo, Michael Gillin, Karl Prado, and Milos Vicic. Energy dependence and dose response of gafchromic ebt2 film over a wide range of photon, electron, and proton beam energies. *Medical physics*, 37(5):1942–1947, 2010.

[29] Quasar verification phantom. `http://medicalphysicsweb.org/cws/product/P000017589`, note = Accessed: 2014-12-10.

[30] JM Fontbonne, G Iltis, G Ban, A Battala, JC Vernhes, J Tillier, N Bellaize, C Le Brun, B Tamain, K Mercier, et al. Scintillating fiber dosimeter for radiation therapy accelerator. In *Nuclear Science Symposium Conference Record, 2001 IEEE*, volume 3, pages 1707–1711. IEEE, 2001.

[31] Frederic Lacroix, Louis Archambault, Luc Gingras, Mathieu Guillot, A Sam Beddar, and Luc Beaulieu. Clinical prototype of a plastic water-equivalent scintillating fiber dosimeter array for qa applicationsa). *Medical physics*, 35(8):3682–3690, 2008.

[32] AS Beddar, KJ Kinsella, A Ikhlef, and CH Sibata. A miniature "scintillator-fiberoptic-pmt" detector system for the dosimetry of small fields in stereotactic radiosurgery. *Nuclear Science, IEEE Transactions on*, 48(3):924–928, 2001.

[33] Scintillating fibers. http://www.crystals.saint-gobain.com/Scintillating_Fiber.aspx, note = Accessed: 2014-12-10.

[34] JHD Wong, M Carolan, MLF Lerch, Marco Petasecca, Sutinder Khanna, VL Perevertaylo, P Metcalfe, and Anatoly B Rosenfeld. A silicon strip detector dose magnifying glass for imrt dosimetry. *Medical physics*, 37(2):427–439, 2010.

[35] AH Aldosari, Marco Petasecca, A Espinoza, Matthew Newall, I Fuduli, C Porumb, Sami Alshaikh, ZA Alrowaili, Michael Weaver, P Metcalfe, et al. A two dimensional silicon detectors array for quality assurance in stereotactic radiotherapy: Magicplate-512. *Medical physics*, 41(9):091707, 2014.

[36] 64 channel analog front end for digital x-ray detector; datasheet available from: http://www.ti.com/lit/ds/slas672/slas672.pdf. Technical report, Texas Instruments, September 2009.

[37] I Fuduli, MK Newall, AA Espinoza, CS Porumb, M Carolan, MLF Lerch, P Metcalfe, AB Rosenfeld, and M Petasecca. Multichannel data acquisition system comparison for quality assurance in external beam radiation therapy. *Radiation Measurements*, 71:338–341, 2014.

[38] Iolanda Fuduli, Claudiu Porumb, AA Espinoza, AH Aldosari, Martin Carolan, Michael LF Lerch, P Metcalfe, AB Rosenfeld, and Marco Petasecca. A comparative analysis of multichannel data acquisition systems for quality assurance in external beam radiation therapy. *Journal of Instrumentation*, 9(06):T06003, 2014.

[39] Elaine Nicpon Marieb and Katja Hoehn. *Human anatomy & physiology*. Pearson Education, 2007.

[40] Anatomical planes and spatial relationships in the human body. http://www.interactive-biology.com/tag/mid-sagittal-plane/, note = Accessed: 2014-12-10.

[41] RO Kornelsen and MEJ Young. Changes in the dose-profile of a 10 mv x-ray beam within and beyond low density material. *Medical physics*, 9(1):114–116, 1982.

[42] Azam Niroomand-Rad, Charles Robert Blackwell, Bert M Coursey, Kenneth P Gall, James M Galvin, William L McLaughlin, Ali S Meigooni, Ravinder Nath, James E Rodgers, Christopher G Soares, et al. Radiochromic film dosimetry: recommendations of aapm radiation therapy committee task group 55. *Medical physics*, 25(11):2093–2115, 1998.

[43] M Westermark, J Arndt, B Nilsson, and A Brahme. Comparative dosimetry in narrow high-energy photon beams. *Physics in medicine and biology*, 45(3):685, 2000.

[44] MJ Butson, T Cheung, and PKN Yu. Scanning orientation effects on gafchromic ebt film dosimetry. *Australasian Physics & Engineering Sciences in Medicine*, 29(3):281–284, 2006.

[45] C Andres, A Del Castillo, R Tortosa, D Alonso, and R Barquero. A comprehensive study of the gafchromic ebt2 radiochromic film. a comparison with ebt. *Medical physics*, 37(12):6271–6278, 2010.

[46] JHD Wong, I Fuduli, M Carolan, Marco Petasecca, MLF Lerch, VL Perevertaylo, P Metcalfe, and Anatoly B Rosenfeld. Characterization of a novel two dimensional diode array the "magic plate" as a radiation detector for radiation therapy treatment. *Medical physics*, 39(5):2544–2558, 2012.

[47] David Wilkins, X Allen Li, Joanna Cygler, and Lee Gerig. The effect of dose rate dependence of p-type silicon detectors on linac relative dosimetry. *Medical physics*, 24(6):879–881, 1997.

[48] Amarjit S Saini and Timothy C Zhu. Dose rate and sdd dependence of commercially available diode detectors. *Medical physics*, 31(4):914–924, 2004.

[49] AB Rosenfeld. Mosfet dosimetry on modern radiation oncology modalities. *Radiation protection dosimetry*, 101(1-4):393–398, 2002.

[50] Zhen-Yu Qi, Xiao-Wu Deng, Shao-Min Huang, Li Zhang, Zhi-Chun He, X Allen Li, Ian Kwan, Michael Lerch, Dean Cutajar, Peter Metcalfe, et al. In vivo verification of superficial dose for head and neck treatments using intensity-modulated techniques. *Medical physics*, 36(1):59–70, 2009.

[51] PH Charles, SB Crowe, T Kairn, J Kenny, J Lehmann, J Lye, L Dunn, B Hill, RT Knight, CM Langton, et al. The effect of very small air gaps on small field dosimetry. *Physics in medicine and biology*, 57(21):6947, 2012.

[52] PH Charles, SB Crowe, T Kairn, RT Knight, B Hill, J Kenny, CM Langton, and JV Trapp. Monte carlo-based diode design for correction-less small field dosimetry. *Physics in medicine and biology*, 58(13):4501, 2013.

[53] Otto A Sauer and Jürgen Wilbert. Measurement of output factors for small photon beams. *Medical physics*, 34(6):1983–1988, 2007.

[54] Sadao Yamazaki, Hiroshi Nakane, and Akio Tanaka. Basic analysis of a metal detector. *Instrumentation and Measurement, IEEE Transactions on*, 51(4):810–814, 2002.

[55] Kai Huang. *Characterization of an in vivo diode dosimetry system for clinical use*. PhD thesis, University of Miami, 2002.

[56] Sea Agostinelli, John Allison, K al Amako, J Apostolakis, H Araujo, P Arce, M Asai, D Axen, S Banerjee, G Barrand, et al. Geant4—a simulation toolkit. *Nuclear instruments and methods in physics research section A: Accelerators, Spectrometers, Detectors and Associated Equipment*, 506(3):250–303, 2003.

[57] BM Oborn, M Williams, M Bailey, and MG Carolan. Imrt treatment monitor unit verification using absolute calibrated beamnrc and geant4 monte carlo simulations. In *Journal of Physics: Conference Series*, volume 489, page 012020. IOP Publishing, 2014.

[58] V Srivastava, P Keall, A Sawant, and Y Suh. Tu-c-m100j-06: Accurate prediction of intra-fraction motion using a modified linear adaptive filter. *Medical Physics*, 34(6):2546–2546, 2007.

[59] Paul A Jursinic, Renu Sharma, and Jim Reuter. Mapcheck used for rotational imrt measurements: step-and-shoot, tomotherapy, rapidarc. *Medical physics*, 37(6):2837–2846, 2010.

[60] Ann Van Esch, Christian Clermont, Magali Devillers, Mauro Iori, and Dominique P Huyskens. On-line quality assurance of rotational radiotherapy treatment delivery by means of a 2d ion chamber array and the octavius phantom. *Medical physics*, 34(10):3825–3837, 2007.

[61] Glenn F Knoll. *Radiation detection and measurement*. John Wiley & Sons, 2010.

[62] Paolo Bolzern, Riccardo Scattolini, and Nicola Schiavoni. *Fondamenti di controlli automatici*. McGraw-Hill Libri Italia, 1998.